4-4-2019 10:00 AM

Texture Analysis and Machine Learning to Predict Pulmonary Ventilation from Thoracic Computed Tomography

Andrew Westcott, *The University of Western Ontario*

Supervisor: Parraga, Grace, *The University of Western Ontario*

A thesis submitted in partial fulfillment of the requirements for the Master of Science degree in Medical Biophysics

Recommended Citation

Westcott, Andrew, "Texture Analysis and Machine Learning to Predict Pulmonary Ventilation from Thoracic Computed Tomography" (2019). *Electronic Thesis and Dissertation Repository*. 6080.
https://ir.lib.uwo.ca/etd/6080

Abstract

Chronic obstructive pulmonary disease (COPD) leads to persistent airflow limitation, causing a large burden to patients and the health care system. Thoracic CT provides an opportunity to observe the structural pathophysiology of COPD, whereas hyperpolarized gas MRI provides images of the consequential ventilation heterogeneity. However, hyperpolarized gas MRI is currently limited to research centres, due to the high cost of gas and polarization equipment. Therefore, I developed a pipeline using texture analysis and machine learning methods to create predicted ventilation maps based on non-contrast enhanced, single-volume thoracic CT. In a COPD cohort, predicted ventilation maps were qualitatively and quantitatively related to ground-truth MRI ventilation, and both maps were related to important patient lung function and quality-of-life measures. This study is the first to demonstrate the feasibility of predicting hyperpolarized MRI-based ventilation from single-volume, breath-hold thoracic CT, which has potential to translate pulmonary ventilation information to widely available thoracic CT imaging.

Keywords

Chronic Obstructive Pulmonary Disease, Magnetic Resonance Imaging, Hyperpolarized Gas MRI, Computed Tomography, Texture Analysis, Machine Learning, Pulmonary Imaging

Co-Authorship Statement

The following thesis contains one scientific conference proceeding and one manuscript that has been submitted for publication. As the first author of these works, I was a significant contributor to all aspects of the studies as well as manuscript preparation and submission. I was responsible for data acquisition, pipeline and software development, conception of the study, experimental design, image processing, statistical analyses and interpretation, as well as manuscript preparation and submission. Grace Parraga, as the Principal Investigator and thesis Supervisor, provided continued guidance and was responsible for the conception of the study, experimental design, data interpretation and drafting and approval of manuscripts. She was also the guarantor of the data integrity and responsible for Good Clinical Practice. Patient study visits and acquisition of pulmonary function data were performed under the supervision of Lyndsey Reid-Jones, Rachel Eddy and Danielle Knipping. Polarization of hyperpolarized gas was performed by Andrew Wheatley, Dante PI Capaldi, Heather Young and myself. MRI acquisition was performed by Trevor Szekeres and David Reese. Below outlines the specific contributions for all co-authors for Chapter 2 and Chapter 3.

Chapter 2 is a peer-reviewed conference proceeding entitled "Texture Analysis of Thoracic CT to Predict Hyperpolarized Gas MRI Lung Function" and it was accepted for *SPIE Medical Imaging* conference proceedings. The proceeding was co-authored by Andrew Westcott, Dante PI Capaldi, David G McCormack, Aaron Fenster and Grace Parraga. I was responsible for data acquisition, pipeline and software development, concept development, experimental design, image processing, statistical analyses and interpretation, as well as manuscript preparation and submission. Dante PI Capaldi assisted in data collection and concept development, David McCormack assisted in data interpretation, and Aaron Fenster assisted in method development and data interpretation.

Chapter 3 is an original research article entitled "Chronic Obstructive Pulmonary Disease: Thoracic CT Texture Analysis and Machine Learning to Predict Pulmonary Ventilation" and it was submitted to the journal *Radiology* on February 26, 2019. The manuscript was co-authored by Andrew Westcott, Dante PI Capaldi, David McCormack, Aaron Ward, Aaron Fenster and Grace Parraga. I was responsible for data acquisition, pipeline and software development, concept development, experimental design, image processing, statistical analyses and interpretation, as well as manuscript preparation and submission. Dante PI Capaldi assisted in data collection, concept development and manuscript revisions, David McCormack assisted in data interpretation and manuscript revisions, Aaron Ward assisted in data interpretation and manuscript revisions, and Aaron Fenster assisted in method development, data interpretation and manuscript revisions.

The appendix contains three published manuscripts completed within my MSc that I was first author for, which are complementary, yet not directly related to the objective and hypothesis of this thesis. As first author I was responsible for data acquisition, statistical analysis, experimental design, manuscript preparation and literature review. Appendix A is a peer-reviewed original research article entitled "Hyperpolarized ^{3}He MRI ventilatory Apparent Diffusion Coefficient of alpha-1 antitrypsin deficiency", and was published as an extended letter to the editor August 13, 2018. The manuscript was co-authored by Andrew Westcott, Dante PI Capaldi, Alexei Ouriadov, David G McCormack and Grace Parraga. Appendix B is a peer-reviewed original research article entitled "Rapid single-breath hyperpolarized noble gas MRI-based biomarkers of airspace enlargement", and was published December 21, 2018. The manuscript was co-authored by Andrew Westcott, Fumin Guo, Grace Parraga and Alexei Ouriadov, where I was co-first author with Fumin Guo. Appendix C is a peer-reviewed review article entitled "Advanced pulmonary MRI to quantify alveolar and acinar duct abnormalities: Current status and future clinical applications", and was published January 13, 2019. The manuscript was co-authored by Andrew Westcott, David G McCormack, Grace Parraga and Alexei Ouriadov.

Acknowledgments

I would first like to thank my supervisor, Grace Parraga. The opportunities you have provided me are incredibly unique; from working on publications, review articles and abstracts, to the opportunity to continually collaborate with colleagues. These experiences have led to personal and professional growth in a short period of time that I could not have imagined before this experience. I greatly appreciate knowing you were always vehemently in my corner to support my work and goals.

I would also like to thank the members of my advisory committee: Aaron Fenster, Aaron Ward and Eranga Ukwatta for your support and guidance. The committee meetings were thought provoking and immensely helpful – but more importantly, I knew I could reach out for any advice to leverage your individual expertise. Further thanks goes to the amazing support of the Medical Biophysics department, including: Kathleen Petts, Umera Ali, Wendy Hough, Jeff Frisbee and Jennifer Devlin. The opportunities provided and excellent communication make me confident I was lucky enough to be a part of one of the best departments there is.

A special thank you goes to everyone within the Parraga lab – past and present – I feel fortunate to get to call each of you my colleague and friend. Each and every one of you have made Robarts and our lab an incredibly special place to work. To Lyndsey Reid-Jones, thank you for being kind, caring and fun – however I was feeling, my mood would improve with a visit to your office. To Tamas Lindenmaier, thank you for putting me out of my job, allowing me to finish my thesis. To Danielle Knipping, thank you for always being kind, calm and helpful. You both made a morning coffee, lunch or discussion on business within the lab incredibly enjoyable. To Alexei Ouriadov, thank you for the opportunity to work with you on multiple interesting projects and for teaching me about diffusion imaging. To Sarah Svenningsen and Miranda Kirby, thank you for the opportunity to work with you on exciting projects, and.

To Rachel Eddy thank you for being my go-to person when I need to talk out an idea or can’t remember something, and for being the true senior student we could rely on this last year. The help, support and encouragement you have provided goes well beyond an extra set of eyes on my work. To Dante Capaldi, thank you for your great sense of humor and genuine interest in all aspects of science – this makes any conversation with you a perfect balance of intellect and humor. To Heather Young, thank you for being an incredible support through my transition to graduate school, and for patiently teaching me the fundamentals of the lab. To Andrea Barker, thank you for stepping up the social game in the lab, a chat with you about life outside work or on human physiology is always an awesome way to spend some time. To Cathy Ong Ly, thank you for always lightening the mood and being positive, as well as our interesting conversations about machine learning topics. To Jonathan MacNeil, thank you for reaching for even more puns than me, and discussing novel COPD imaging phenotypes. To Alexander Matheson, thank you for being a coding partner, and for discussing interesting physics concepts, as well as any other topic you happen to know a lot about. The hard work, perseverance and positive attitudes each of you display is inspiring.

A huge thank you to all of the students and personnel around Robarts and beyond who have made graduate school immensely fun, creating a work-life balance that allowed me to focus on working hard when needed. Thank you to first year communications, and everyone involved, for introducing me to so many great people who would go on to be great friends.

Finally, my deepest gratitude goes towards Sarah, my family and my friends outside of Western. You have provided continuing, unwavering support in anything I do, and were always able to provide an outside perspective if I ever needed advice. Despite being too busy at times to communicate and visit as much as I wanted, I could count on you understanding and providing love and friendship whenever we reconnect. I’m incredibly lucky to have such great relationships!

Table of Contents

List of Tables

List of Figures

List of Appendices

List of Abbreviations

^{129}Xe	Xenon-129
^{1}H	Proton
^{3}He	Helium-3
AATD	Alpha-1 Antitrypsin Deficiency
ADC	Apparent Diffusion Coefficient
AUC	Area Under the receiver-operator characteristic Curve
COPD	Chronic Obstructive Pulmonary Disease
CT	Computed Tomography
DL_{CO}	Diffusing Capacity of the lung for Carbon Monoxide
FEV_1	Forced Expiratory Volume in 1 Second
FRC	Functional Residual Capacity
HU	Hounsfield Unit
HU_{15}	15th percentile of CT density histogram
MRI	Magnetic Resonance Imaging
mSv	Millisievert
PFT	Pulmonary Function Test
RA_{950}	Relative Area Under -950 HU
Rb	Rubidium
ROC	Receiver-Operator Characteristic
ROI	Region of Interest
RV	Residual Volume
SGRQ	St. George's Respiratory Questionnaire
SVM	Support Vector Machine
VOI	Volume of Interest

CHAPTER 1

1 INTRODUCTION

Chronic obstructive pulmonary disease (COPD) is a disease characterized as non-reversible airflow limitation, which causes the lung to be heterogeneously ventilated. Hyperpolarized gas magnetic resonance imaging (MRI) provides the ability to image the ventilation within the lung, however is limited to research centres, whereas thoracic computed tomography (CT) is widely available. In this thesis, the underlying hidden and visible structural information within CT images was quantified with texture analysis and machine learning to predict pulmonary ventilation heterogeneity.

1.1 Motivation and Rationale

Chronic obstructive pulmonary disease (COPD) is defined by irreversible airflow obstruction, and presents a serious burden to the health care system and to patients' quality of life. COPD was projected to become the third leading cause of by 2030,[1] however has surpassed the projections and was recently reported to already be the third leading cause of death worldwide.[2] As of now there is no cure for COPD,[3] instead the current management goal is to improve health status, prevent exacerbations and prevent related complications and mortality.[3] Figure 1-1 displays the burden of hospitalizations from patients with COPD in Canada. Importantly, a large portion of patients are admitted for multiple hospital visits compared to other diseases responsible for large numbers of hospitalizations.[4] Related to these hospitalization statistics, there is a mean annual COPD-related healthcare cost per patient of over $3000.[5]

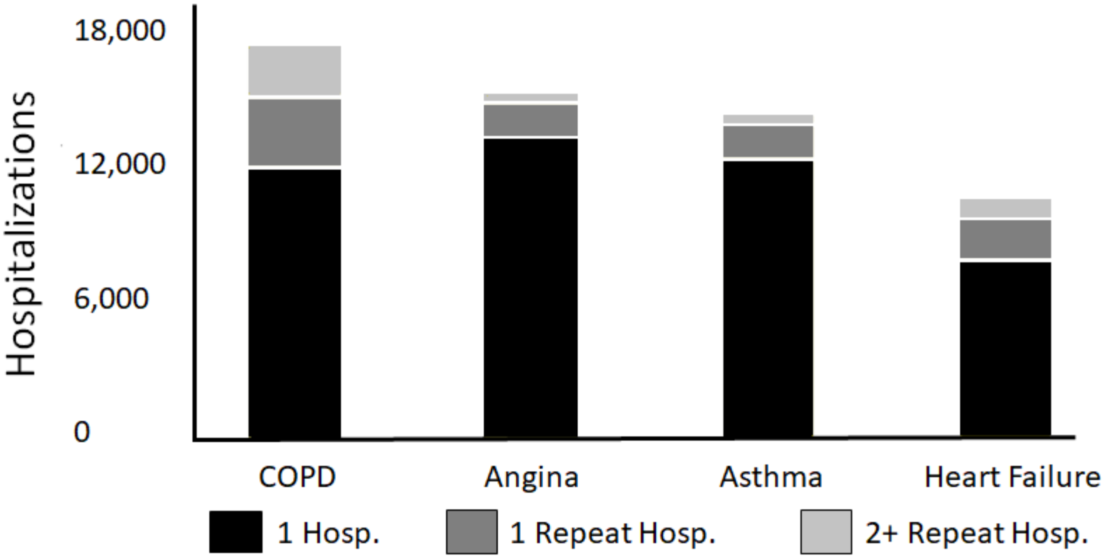

Figure 1-1: Leading causes of hospitalizations in Canada.
Figure adapted from Canadian Institute of Health Information, Health Indicators 2008 report.[4]

The large, and growing, burden illustrates the sub-optimal management and treatment of COPD. Current measures of lung function include relatively simple and inexpensive pulmonary function tests. Despite their wide use, these tests provide only a global measure to encapsulate the complex heterogeneity of the disease, which manifests itself in many ways including airway obstruction, parenchymal destruction and related pathophysiology such as vascular abnormalities. Further, COPD is a heterogeneous disease, and does not affect the entire lung uniformly. A more precise and sensitive method for characterizing and monitoring underlying structural abnormalities, and resulting functional consequences, in COPD is needed. This has motivated the use of pulmonary imaging to enable a regional understanding of underlying structural abnormalities in patient populations, as well as on an individual level.

Since the late 1970s, x-ray computed tomography (CT) has been used for pulmonary exams in COPD, specifically for detecting parenchymal destruction, or emphysema.[6-10] CT has further been used to visualize the airways and vasculature within the lung. Alternatively, emerging imaging technologies such as hyperpolarized gas magnetic resonance imaging (MRI) have been developed that allow visualization of ventilation heterogeneity within the lung that is a result of underlying structural abnormalities. Hyperpolarized gas MRI provides unique information on lung function and patient outcomes, however this functional information is currently limited to a number of research centres of excellence. To translate this unique information, this thesis focuses on predicting regional ventilation heterogeneity based on structural patterns and determinants as quantified within widely available thoracic CT.

In this chapter, background relevant to the understanding and motivation of the original research work presented in Chapters 2 and 3, is provided. In (1.2), an overview of the relationship between structure and function of the lung is presented. Section (1.3) presents the pathophysiology of COPD, followed by the clinical measures (1.4) and current imaging techniques (1.5) used to monitor COPD. Texture analysis of medical images and the current role it plays in lung imaging will be introduced in (1.6). Finally, the hypothesis and objectives of the thesis will be introduced and stated in (1.7).

1.2 Structure and Function of the Lung

The lung is a complex organ that allows for efficient distribution and exchange of oxygen into the bloodstream. The structure of the lungs consists of the airways, parenchyma and vasculature, while the function is how these components exist together to distribute oxygen throughout the lung and deliver it into the bloodstream.

1.2.1 Airways

The airways are the highway for delivery of oxygen, and range widely in size and structure. A diagram of the entire airway tree is shown in Figure 1-2. The beginning airway generations, including the trachea and the main bronchi, have a large diameter and are supported by cartilage. As the airway generation increases, the number of airways grows exponentially due to branching, while the airway diameter decreases. At the terminal bronchioles, the airways are no longer supported by a cartilage and are simply supported by the airway wall and smooth muscle, as well as the matrix composed of alveoli.

As shown in Figure 1-2, the airway tree can be split into the conducting zone and the respiratory zone. The conducting zone is comprised of the airways which do not participate in gas exchange, whereas the respiratory zone is comprised of airways which are lined with alveoli. Conducting zone airways hold approximately 150 millilitres of air, and are often referred to as dead space as they do not participate in gas exchange. This is converse to the respiratory and transition zone airways, which participate in gas exchange and can hold approximately 2.5-3 litres at rest, depending on the size of the individual's lungs.[11]

Within the conducting zone the airflow is driven by bulk flow and the inertia of the air. Once through the conducting zone, the total cross-sectional area of the airways increases, slowing the velocity of airflow. From this point onward, the air movement is largely due to diffusion of the gas.

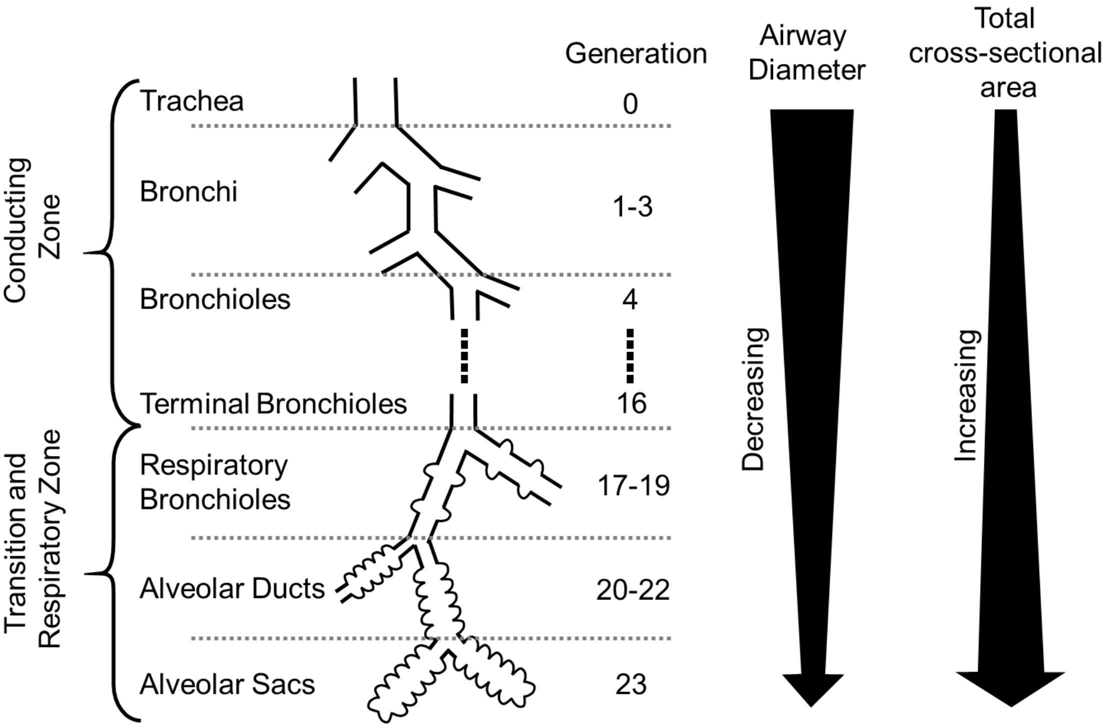

Figure 1-2: Idealized human airway generation diagram.
Adapted from Respiratory Physiology: The Essentials 10th edition.[11]

1.2.2 Parenchyma

The lung and airway system is designed to maximize the surface area available for gas to diffuse into the blood. Small alveolar sacs comprise the terminal point of the airways, where the wall is thin enough to allow oxygen to diffuse into the bloodstream. These well-formed, small alveolar sacs provide the lung with 50-100 m^2 of surface area for gas exchange. Figure 1-3 displays a diagram of the alveoli and bloodstream interaction, where it can be seen that the alveoli takes a spherical shape to maximize the surface area. There are approximately 500 million alveoli within the lung,[12] with a dense capillary network around the alveoli. The capillaries which participate in gas exchange are not much larger than a single blood cell, and the alveolar-capillary membrane is extremely thin, approximately 0.2-0.3 µm, allowing for fast diffusion of gases across the membrane.

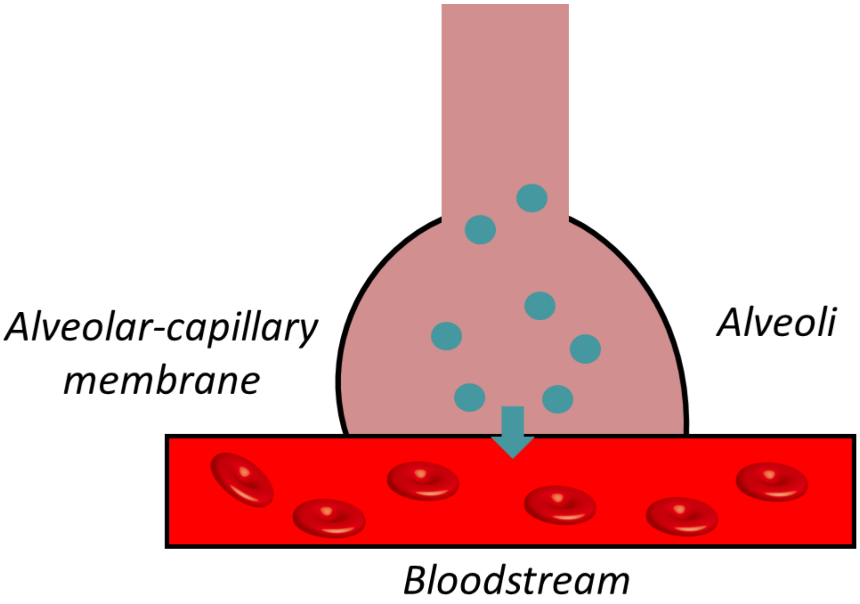

Figure 1-3: Diagram of oxygen exchange into the bloodstream.
Diagram showing gas (blue circles) exchange into the bloodstream from the alveoli.

1.3 Pathophysiology of Chronic Obstructive Pulmonary Disease

Lung disease can occur from an abnormality or dysfunction in any of the components above, preventing optimal delivery of oxygen to the bloodstream. COPD is characterized by persistent airflow limitation caused by a combination of parenchymal destruction (emphysema) and airways disease (chronic bronchitis).[3] COPD is progressive over time, and is a result of exposure to exogenous irritants such as cigarette smoke, environmental/occupational irritants or genetic conditions such as alpha-1 antitrypsin deficiency.[3]

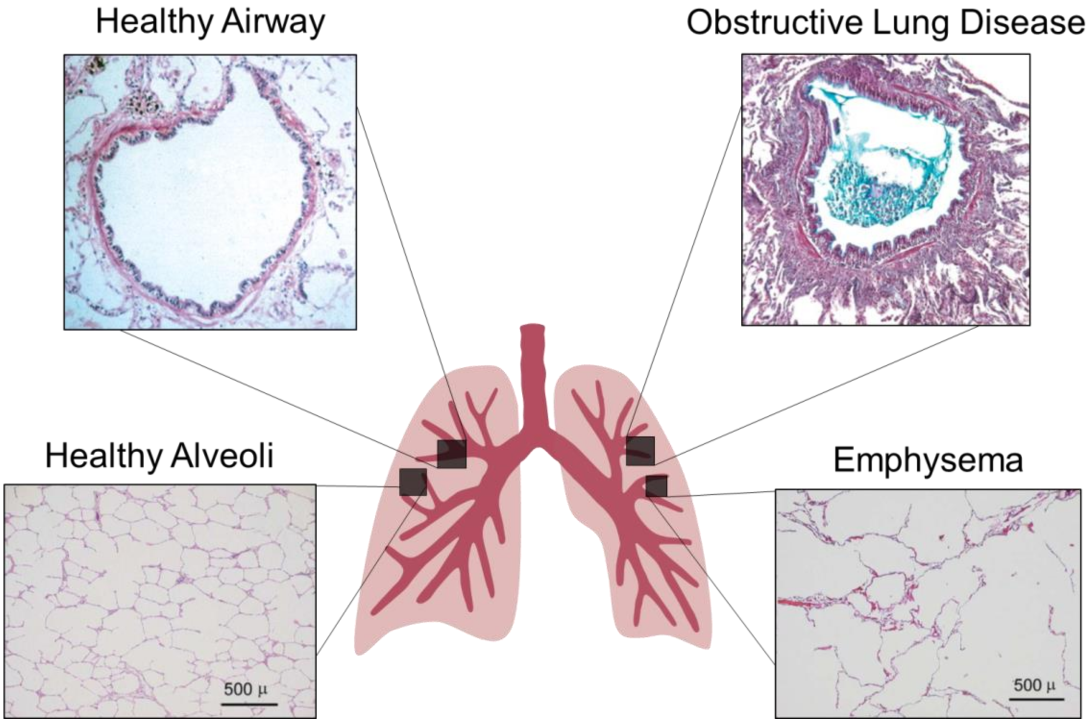

Figure 1-4: Diagram of pathophysiology of chronic obstructive pulmonary disease. Healthy airway and obstructive lung disease panels are adapted from Hogg (2004),[13] permission to reproduce provided in Appendix E. Healthy Alveoli and Emphysema are adapted from Woods et al. (2006),[14] permission to reproduce provided in Appendix E.

1.3.1 Emphysema

Emphysema is characterized by enlargement of the airspaces distal to the terminal bronchioles, where gas exchange occurs. This enlargement is due to the destruction of parenchymal tissue, where the effects can be observed in the lower right quadrant of Figure 1-4, compared to healthy alveoli in the lower left quadrant. The destruction of parenchyma may be heterogeneous and to varying severities in different regions within the lung, which give sub-classifications of emphysema including: centrilobular, panlobular and bullous emphysema. Many patients have a combination of these sub-classifications, and in severe emphysema it may be difficult to distinguish them.

Some of the earliest observations of emphysema stem from work in the 1950s from Leopold and Gough. Their seminal work included observations on the inflammation, calibre of bronchi and weakness within emphysematous spaces.[15] Since then, there have been extensive studies, moving from two-dimensional *ex vivo* measurements of emphysema, to three-dimensional *ex vivo* measurements of emphysema,[16-18] and eventually *in vivo* monitoring of emphysema using imaging as described in Section 1.5.

The understanding of COPD changed in the 1960s, when Dr. James Hogg et al. published "The site and nature of airway obstruction in chronic obstructive lung disease", demonstrating the importance of the small airways.[19] They observed that in a healthy individual, the small airways contributes a small amount of the total airways resistance. However, in patients with COPD it was observed this relationship was inverted and small airways resistance was significantly increased. This increased resistance was present in regions with and without emphysema, indicating small airway abnormalities may predate the development of emphysema.

1.3.2 Chronic Bronchitis

Chronic bronchitis is characterized by sputum production and airflow obstruction for greater than three months during two consecutive years.[3] The causes of cough and airflow obstruction are believed to be inflammation, mucus and damage to airways. Early investigations of chronic bronchitis observed a relationship between mucous hypersecretion and thickening of the bronchial mucus glands,[20-23] as well as between mucous hypersecretion and accelerated lung function decline.[24] An example of airway inflammation and mucus presence is shown in the upper right quadrant of Figure 1-4, where mucus is observed in the airway lumen leading to a decreased cross-section for airflow.

1.4 Clinical Measures of Global Lung Function

"Pulmonary function tests provide objective, quantifiable measures of lung function. They are used to evaluate and monitor diseases that affect heart and lung function" Crapo 1994.[25]

To diagnose and monitor COPD, clinicians primarily rely on pulmonary function tests (PFT). These are simple breathing maneuvers that monitor flow rate, lung volumes and gas exchange at the mouth to provide information about the function of the lungs. These tests include spirometry, plethysmography and the diffusing capacity of the lung for carbon monoxide (DL_{CO}). Measurement values can be expressed as percent of the predicted value, which is a function of the patient's age, sex, height and ethnicity.[26] The impact of obstructive lung disease on patients can also be measured using quality-of-life questionnaires and exercise capacity tests.

Of the breathing tests available, spirometry is currently the simplest and most widely used. Spirometry can be performed using a handheld device, such as that shown in Figure 1-5A.[27] The patient performs multiple tidal breaths, then is instructed to inhale fully, followed by a forceful exhalation until they cannot exhale further. A representative lung volume curve measured by the spirometer is displayed in Figure 1-5A. From this maneuver, the forced expiratory volume in one second (FEV_1) and the forced vital capacity (FVC) are measured.

The clinical diagnosis of COPD is based on the lung volumes measured with spirometry, as shown in Table 1-1. A ratio of FEV_1 to FVC less than 70 percent is the diagnostic cut-off for COPD according to the Global Initiative for Chronic Lung Disease (GOLD) criteria.[3] The severity of COPD is then graded based on FEV_1, where a lower percent of predicted is indicative of increased obstruction.

Table 1-1: Diagnostic cut-offs from the Global Initiative for Chronic Lung Disease (GOLD).

The pulmonary function test cut-off for diagnosis of COPD is for $FEV_1/FVC<70\%$, the severity grading is based on FEV_1 percent predicted.

	Pulmonary Function Test If $FEV_1/FVC < 70\%$
GOLD Grade 1	$FEV_1 \geq 80\%_{pred}$
GOLD Grade 2	$50\%_{pred} \leq FEV_1 < 80\%_{pred}$
GOLD Grade 3	$30\%_{pred} \leq FEV_1 < 50\%_{pred}$
GOLD Grade 4	$FEV_1 < 30\%_{pred}$

Plethysmography can be used to measure additional lung volumes, based on Boyle's law.[28] The patient is seated in a sealed chamber, as shown in Figure 1-5B, and performs a series of breathing maneuvers, including tidal breathing, full inspiration and full expiration. An exemplar lung volume curve is also displayed in Figure 1-5B. In the context of COPD, the residual volume and functional residual capacity will often be increased due to gas trapping from the collapse of airways.

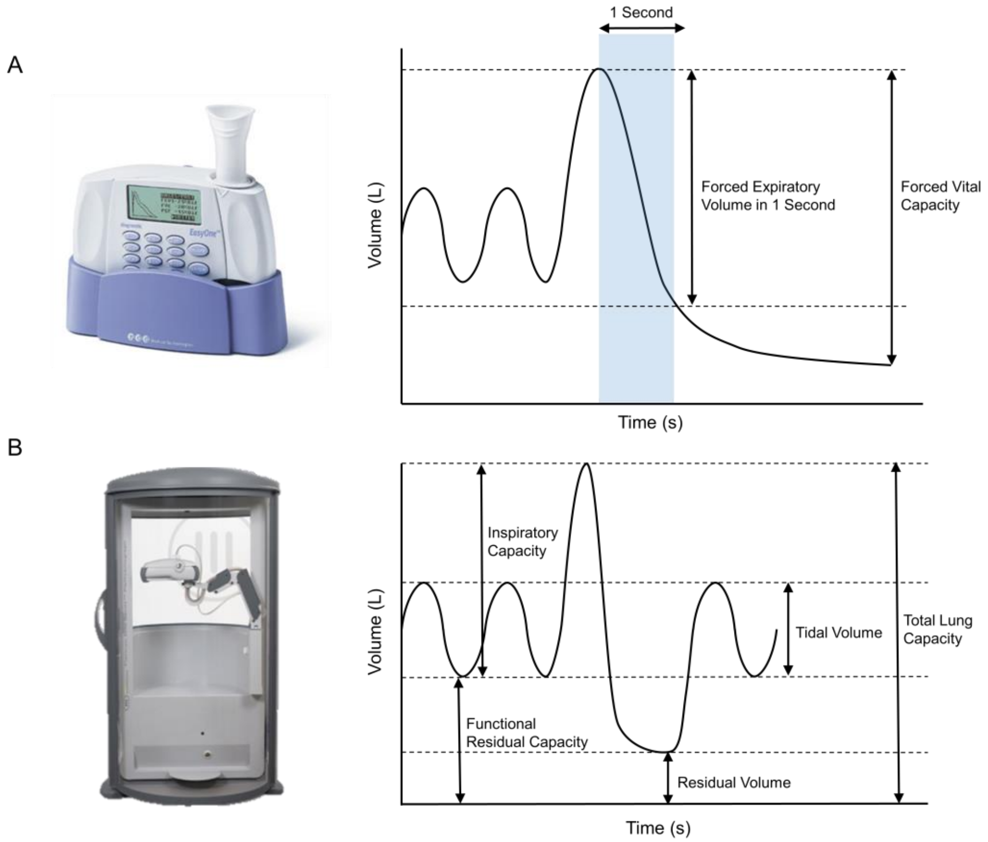

Figure 1-5: Spirometry and plethysmography devices and measurements.
A) Handheld spirometer and measurements of the forced expiratory volume in one second and the forced vital capacity. B) Plethysmography box for lung volume measurements.

Further, the morphology of the alveoli can be probed using the DL_{CO}.[29] This test is performed by inhaling a specific mixture of gas, containing a low concentration of carbon monoxide (CO) (0.3%). The patient then holds their breath at total lung capacity for eight seconds, during which the CO diffuses across the alveolar-capillary membrane and into the blood. When the patient breaths out, the concentration of CO is measured and compared to the initial concentration, from which the amount of CO that has diffused into the blood is inferred. Patients with emphysema will have a decreased DL_{CO} due to a reduction of alveolar surface area for gas exchange, however a decreased DL_{CO} may also be indicative of a thickening of the alveolar-capillary membrane, among other abnormalities.

The impact that COPD has on the life of a patient is also an important measure. To quantify this, patient quality of life is measured using the St. George’s Respiratory Questionnaire (SGRQ).[30] The SGRQ includes information from different aspects of disease effects, including symptoms, activity and impacts on daily life. The scores from each component of the questionnaire are then averaged to give a single SGRQ value. Further, exercise capacity can be quantified using tests such as the six minute walk test.[31, 32] The six-minute walk test, as well as other exercise capacity measurements, have been shown to be clinically important measures.[33-35]

Despite the ability to simply and cost-effectively monitor lung disease, the tests described above do not provide sensitive quantitative or regional measurements of lung disease. In healthy individuals, the small airways contribute only a small portion of the total lung resistance, however, in COPD these small airways may be where the disease begins,[19] and therefore may not be detected by measuring lung volumes and capacities.

1.5 Imaging Pulmonary Structure and Function

"There may be considerable obstruction in the peripheral airways that would affect ventilation distribution and gas exchange but would have little effect on function tests designed to reveal obstruction. When total airway resistance is elevated to a clinically detectable level by disease in the small airways, obstruction is much more severe than is generally recognized." Hogg et al. *1968.*[19]

Contrary to clinical measures of lung function, pulmonary imaging provides the opportunity to view regional abnormalities within the lung. As discussed in Section 1.2, the structure and function of the lung are innately connected. Anatomical imaging modalities provide the opportunity to visualize the structural abnormalities which in turn may be consequential in determining the functional abnormalities, which can be measured using functional imaging techniques.

1.5.1 Structural and Anatomical Imaging

First introduced in the late 1970s, x-ray computed tomography (CT) allows for visualization of the structure within the lung, as shown within Figure 1-6. Thoracic CT can be acquired under breath hold conditions, where a patient is instructed to inhale fully, or by inhaling a set volume of gas from functional residual capacity. CT then provides an attenuation map of the lung, where a density of -1000 Hounsfield units (HU) indicates the presence of air, and as such, voxels with a density near -1000 HU indicate regions of tissue destruction. Two methods are commonly used to quantify the severity of emphysema in a patient, either a threshold method or percentile method. The threshold method quantifies the percentage of the lung that has a density of less than the threshold. Commonly used thresholds include -910 HU,[36] -950 HU[37] and -960 HU.[38] The percentile method reports the value of the percentile density from a histogram, often used values include the 5th percentile and 15th percentile. The ability to visualize emphysema *in vivo* has allowed for sensitive monitoring of disease progression, and has been shown to reduce the statistical power needed to perform clinical trials of treatment in alpha-1 antitrypsin deficiency compared to spirometry.[39]

More complex CT analyses have also been employed, including metrics which examine the statistical properties of low attenuating (< -960 HU) clusters in CT images.[40] The cumulative size distribution of low attenuating clusters were shown to follow a power-law relationship, and the power-law exponent was shown to be reduced in relation to a decrease in DL_{CO}.[40]

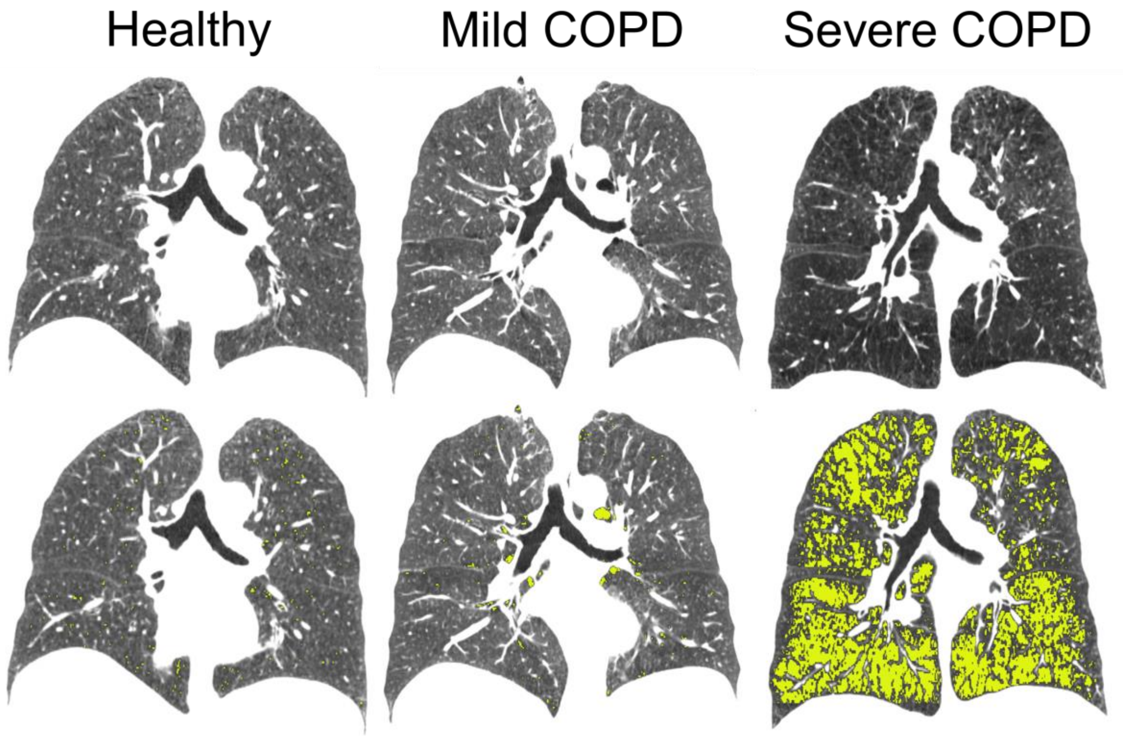

Figure 1-6: CT Imaging of healthy, mild COPD and severe COPD individuals.

Healthy DL_{CO}= 106%$_{pred}$, FEV_1/FVC= 72%, FEV_1 = 80%$_{pred}$; Mild COPD DL_{CO}=87%$_{pred}$, FEV_1/FVC=60%, FEV_1=94%$_{pred}$; Severe COPD DL_{CO}=17%$_{pred}$, FEV_1/FVC=29%, FEV_1=28%$_{pred}$. Yellow areas show regions of density less than -950 HU.

CT can also be used to visualize the airways and vasculature within the lung. Spatial resolution in low-dose CT typically limits the segmentation of airways to ~7th generation airways (~2 mm diameter). Despite these limitations, from airway segmentations, important measurements can be made such as airway wall thickness, wall area and lumen area. Airway measurements have led to observations including recent work showing apparent loss of airways in severe emphysema,[41] and the extent of this loss measured using CT is an independent predictor of patient quality of life.[42] CT measures have also been shown to be risk factors for exacerbations, including the percentage of emphysema or airway wall thickening which were both associated with COPD exacerbation frequency.[43]

Further, changes in pulmonary vasculature have been observed using CT perfusion imaging, indicating there may be vasculature changes at early stages of COPD development.[44] Non-contrast enhanced CT has also been used to observe distal pruning of small vessels in COPD, where a decreased ratio of small vessel blood volume to total blood volume was shown.[45, 46]

More recently, high resolution structural images of the lung have been achieved using magnetic resonance imaging (MRI). MRI of the lung presents a unique challenge because there is a low density of tissue and many tissue/air interfaces. This means there is a small magnitude of signal and a high amount of paramagnetic oxygen, which creates local field inhomogeneities and increases the relaxation rate. To account for the increased relaxation rate of the tissue within the lung, ultra-short echo time sequences have been developed.[47-50] These, and newer techniques such as zero echo time sequences, are advances towards MR images achieving similar structural information as present within CT, with no radiation dose to the patient.[51]

1.5.2 Functional Imaging

While structural information may indirectly inform upon the efficiency of the lung, with *in vivo* imaging there is opportunity to image function within the lung.

X-ray Computed Tomography

Contrast-enhanced CT utilizes inhaled xenon and dual energy techniques to image where in the lung the xenon gas reaches to visualize ventilation. To accomplish this, dual-source CT scanners are used for near-simultaneous acquisition of two separate energy spectra. The separation between high and low energy spectra allows for differentiation between the inhaled contrast gas, and the native materials to the lung, to generate gas distribution images. Dual-energy CT has previously been applied to observe ventilation patterns in patients with COPD.[52, 53]

In addition to dual-energy CT, it is possible to use air as a contrast agent by acquiring images at multiple lung volumes, where you can attribute the change in density within an anatomical location to the flux of air. Both four-dimensional CT (4D-CT) and multi-volume CT have been used to create surrogate measures of ventilation by registering multiple lung volumes acquired and quantifying the density change as air enters the lung.[54-59]

Despite success of CT for functional imaging, the clinical adoption is limited due to the increased radiation dose required for multiple, or extended length, scans. Additionally, the necessity of additional scans or an exogenous contrast agent with specialized hardware make these scans costly.

Hyperpolarized Gas Magnetic Resonance Imaging

Hyperpolarized gas MRI uses an exogenous gas, which is polarized to have an atomic spin. When inhaled, the spatial distribution of the gas within the lungs can be imaged using specialized receive coils within a magnetic resonance scanner. Due to the low spin density available in the gas state, hyperpolarization is performed. This is done through optical pumping, where angular momentum is given to an alkali metal (typically Rubidium) through a circularly polarized laser at the resonance frequency of the metal (~794.6 nm for Rubidium). The angular momentum is then transferred from the metal to the nuclei being polarized (^{3}He or ^{129}Xe) through collisions. The optical pumping technique can increase the polarization of the gas up to five orders of magnitude greater than through a thermal process.

The field began in the 1990s, when inhaled ^{129}Xe was first imaged within a mouse model.[60] Since then, the use of hyperpolarized gas MRI has greatly expanded, and has seen the adoption of hyperpolarized ^{3}He, however, is currently undergoing a transition back to ^{129}Xe due to the increasing cost of ^{3}He. Figure 1-7 displays the ventilation patterns measured using hyperpolarized ^{3}He across COPD disease severity. Cyan indicates the volumes ventilated within a breath-hold, whereas dark regions are not ventilated. To quantify the extent of ventilation abnormalities, the ventilation defect percent (VDP) is calculated as the total volume of ventilation defects normalized to the thoracic cavity volume.[61] The Brownian motion of hyperpolarized gas under diffusion gradients has also been used to probe microstructure of the lung using the apparent diffusion coefficient or morphometry.[14, 62-64] Work related to these measures is complimentary to the objective and hypothesis of this thesis, and are presented in Appendix A-C.

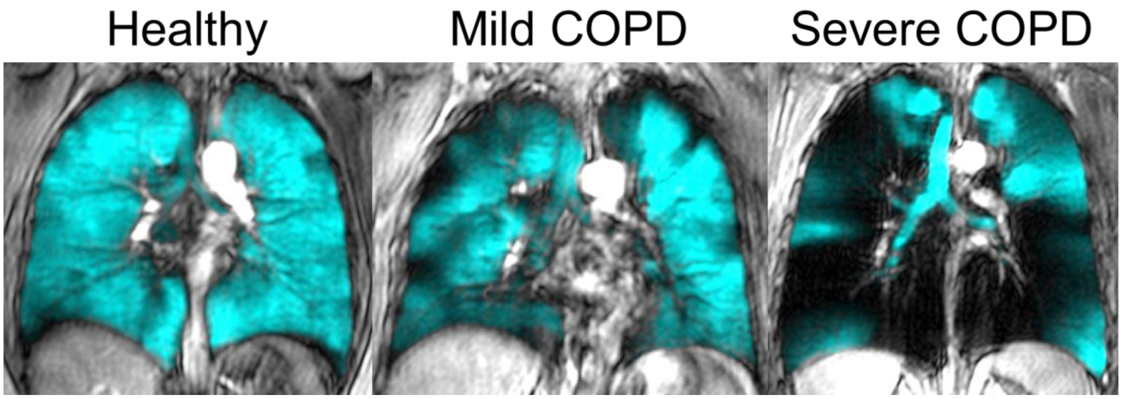

Figure 1-7: ^{3}He hyperpolarized gas MRI for healthy, mild COPD and severe COPD individuals.
Examples of hyperpolarized ^{3}He (cyan) overlaid on anatomical ^{1}H (gray) MRI. The dark regions within the lung are regions which are not filled within a breath hold, and are termed ventilation defects. An increase in severity in COPD is related to an increase in ventilation defects.

Both ^{3}He and ^{129}Xe hyperpolarized gas MRI have been shown to be safe and reproducible measures.[65-67] In COPD patients, ^{3}He VDP is related to spirometry,[68] symptoms and exercise capacity,[69] CT based measurements of emphysema and patient exacerbations.[70, 71] Ventilation defects have also been shown to be spatially related to structural observations of gas trapping and emphysema as measured using CT parametric response maps.[72] Using ^{129}Xe has yielded similar observations, with many of the ^{3}He studies being paired with

^{129}Xe, as well as independent studies where the VDP was again shown to be related to spirometry.[73]

It is important to note that despite each ventilation imaging technique relating to patient measures, they all vary slightly on the physiology they are probing. There are known differences between ^{3}He and ^{129}Xe,[68, 74, 75] likely due to the density and viscosity of each gas allowing for different flow dynamics (based on Reynolds Numbers) in different calibre airways. Differences between CT-derived ventilation and hyperpolarized gas imaging have recently been reported,[76] where a portion of the difference is likely a difference due to different breathing maneuvers. The majority of hyperpolarized gas imaging is based on static breath-holds, whereas CT is based on volumes throughout the breathing cycle.

1.6 Texture Analysis in Medical Imaging

"Texture is an innate property of virtually all surfaces ... It contains important information about the structural arrangement of surfaces and their relationship to the surrounding environment." Haralick 1973.[77]

In medical imaging, texture analysis provides a quantitative method for describing patterns within an image, which may relate to different underlying pathophysiological determinants. Texture analysis has played a large role in the field of computer-aided diagnosis, where biomedical images are mined for information reflecting underlying pathophysiology which can then be used for the detection and diagnosis of disease.[78] The rapid growth of the application of texture analysis and machine learning in medicine is evident in Figure 1-8, where an exponential increase in PubMed search results are observed, compared to a near linear increase in CT and MRI.

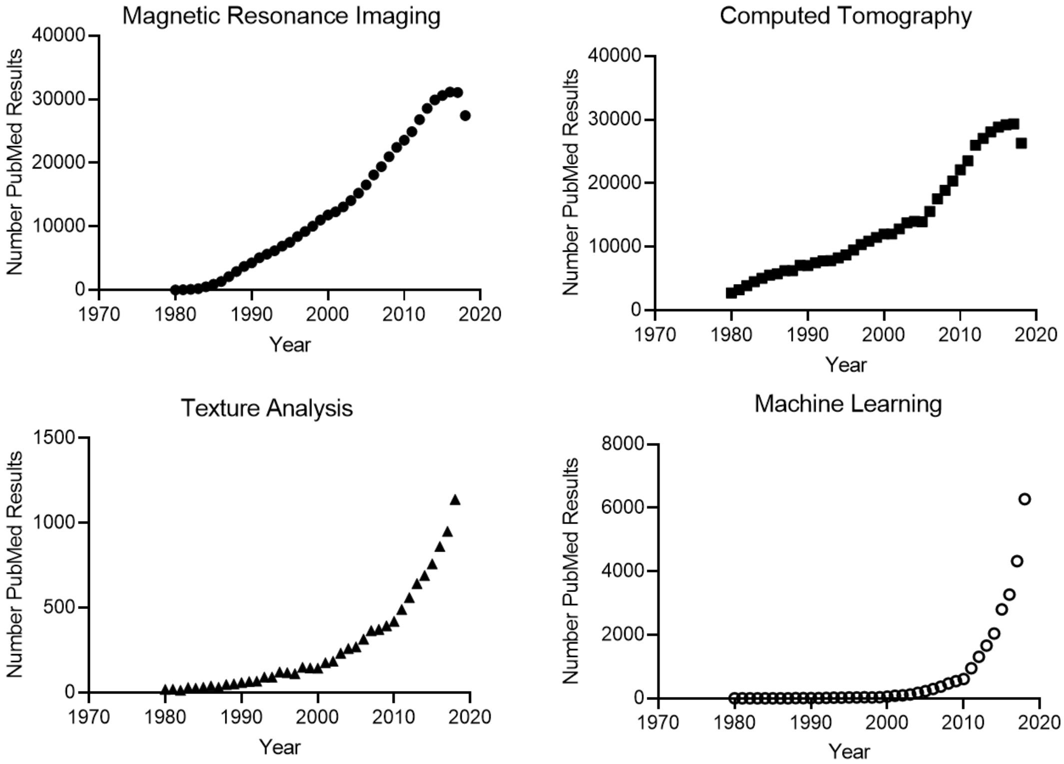

Figure 1-8: PubMed results for thesis keywords.
Displaying the number of results sorted by year, displaying an indirect observation of the popularity of these methods.

1.6.1 Typical Work Flow

A typical workflow for texture analysis is outlined in Figure 1-9, where it includes image acquisition, region of interest definition, feature extraction from the region of interest, and feature analysis. The feature analysis can involve calculating which features are unique to certain regions, or including features within a machine learning algorithm. Below, the methods used for each of these steps are described, where segmentation and registration can be used to define a region of interest, and feature selection and machine learning are methods to analyze the extracted features.

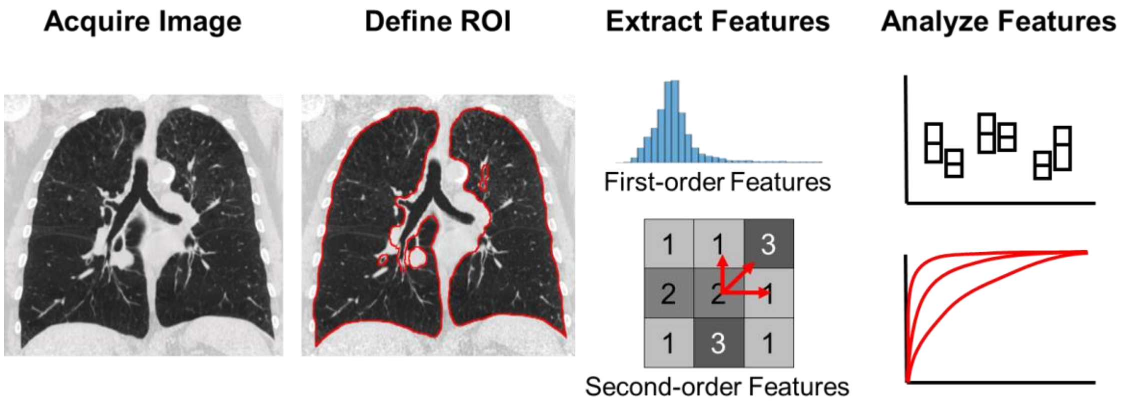

Figure 1-9: Typical workflow for texture analysis.
The typical workflow for texture analysis include image acquisition, region of interest definition, feature extraction then feature analysis. ROI=region of interest.

Segmentation

Medical image segmentation is the task of partitioning an image into multiple regions, based on a specified similarity characteristic. The simplest segmentation is done manually, where an observer outlines the structure desired. However, this method can be quite time intensive, and leads to high variability depending on the observer. Due to this, medical imaging has moved to semi-automated or automated segmentations. Segmentation of the lung cavity is a relatively easy task because there is a distinct density difference between lung tissue and other tissue. However, it is complicated by the presence of vasculature, diseased tissue and differentiating the trachea from lung tissue.

The simplest computer aided segmentation approach is based on thresholding the image. Thresholding partitions the image into different regions based on a set, or algorithmically determined, signal intensity.[79, 80] Another approach to segmentation is region growing techniques, which segments regions connected by intensity similarities. This can be performed by manually, or automatically selecting a seed location, and growing the region by iteratively adding neighboring pixels within a certain similarity criteria.[81, 82] These methods have been employed to segment proton MRI thoracic cavity images previously.[61] More advanced methods including watershed,[83] clustering,[84, 85] and model based techniques[86] have also been employed. Many of these methods have been utilized to create automated lung segmentation algorithms as an integral step in computer-aided diagnosis pipelines.[87-89]

More recently, deep learning has been applied to medical image segmentation, with the wide adoption of convolutional neural network architectures such as U-Net.[90] U-Net is a neural network architecture which gained popularity after outperforming other segmentation tasks in multiple Grand Challenges. The U-Net architecture has also been extended to be compatible with volumetric segmentation, versus 2-dimensional segmentation, in a network referred to as V-Net.[91] Converse to the previously described segmentation techniques, deep learning does not follow rule based segmentation, and instead learns to identify features relevant to the specific segmentation task trained on through backpropagation. One common limitation with deep learning for segmentation is the necessity for large labeled datasets, which can be time consuming to curate or difficult to attain. However, there are open source trained segmentation networks available on repositories such as GitHub or NiftyNet[92] which can be more simply applied to a specific segmentation task without needing to train an entire network.

Registration

Registration is often required to determine the ground truth for texture analysis, whether that be registering MRI to histology, conventional to contrast-enhanced images, or structural to functional images. There are different registration techniques including rigid, affine and deformable. These techniques enforce limits on how the images can be moved or warped to match the other image. Rigid registration allows only translations and rotations of the moving image, and affine registrations maps parallel lines across the images being registered. Deformable registration cannot be represented using a transformation matrix, and instead creates local vector displacement fields to map the images to the same space. The technique you choose will depend on the registration task, where a rigid or affine registration is often sufficient if the images being registered are of the same anatomical space. However, for registration of inherently different images, deformable registrations may be more successful.

A simple registration technique is landmark based registration, where a user places landmarks at the same anatomical location on the two images to be registered, and a deformation is calculated and applied to minimize the difference in the locations. This method has previously been developed for affine registration of hyperpolarized gas MRI to anatomical proton MRI.[61] More complex registration methods work to minimize a cost function based on the similarity of the images being registered, or by matching segmented surfaces. State-of-the-art registration algorithms used in medical imaging include the demons registration[93] and the modality independent neighbourhood descriptor (MIND) registration.[94]

Feature Extraction

To describe the underlying patterns within the image, feature extraction is performed. The simplest features can be extracted from the histogram of values within the region of interest. These first-order features include the mean, median, mode, standard deviation, skewness and more. In CT imaging, these relate to the density, and include quantitative CT measures discussed in Section 1.5.1 including the relative area less than a threshold value, or the histogram percentile.

Despite containing information on the voxel values within a region of interest, first-order features do not contain any information regarding the spatial distribution of voxels. To overcome this, frequently used approaches are based on second-order statistics which quantifies the relationship between voxels. Two of the most commonly used second-order statistic features include gray level co-occurrence matrix (GLCM)[77] and run length matrix (RLM)[95] derived features.[96] The GLCM is populated by recording the number of times gray-level values appear within proximity to each other, where the column and row indices represent the pixel value, and the value within each element is the number of times the pixel values appear next to each other. Therefore, a GLCM with large values close to the diagonal represents an image that does not have many sharp edges. The RLM is populated by recording the number of runs within an image, where the row indices are the pixel value and the column indices are the length of a run, and the element value is the number of runs. Therefore, a RLM with most values in the first columns indicates an image which is very heterogeneous in appearance.

Many further texture features may be calculated, including filter based methods, local binary patterns, spherical harmonics, Markov models and wavelets. A comparison of the use cases and properties of each of these features are presented in a review of three-dimensional texture features in medical imaging.[96]

To account for noise, and reduce the size of the matrices, values must be binned to create both RLM and GLCM. If this is not performed, there would be virtually zero runs within the RLM, as there would be a very small chance of the exact same value appearing. A similar problem would be observed within the GLCM. The width of the bin will be a determinant of how well the features describe the region of interest; if the bin width is too small, the features will be noisy, whereas if it is too large you will not be sensitive to differences which may be physiologically relevant. The bin width is therefore a parameter that should be carefully chosen and is often experimentally determined to address what is best for the specific task. To address these problems, filtering and smoothing of the image may also be performed.

More recently, with the advances made possible from improvements in hardware and software, deep neural networks have been widely adopted in medical image analysis. The most popular method for deep learning, a subtype of machine learning, is using convolutional neural networks (CNN). Conceptually, CNN are iteratively trained to learn abstractions of images from low level (such as edges and corners), to high level (such as shapes and concepts) features. These abstractions are learned and stored in filter banks, which are specially tuned to the type of image the CNN was trained on. As discussed, texture analysis aims to describe underlying patterns in an image, and in the same way, filter banks from a CNN quantify patterns observed. The largest difference between the methods is that texture analysis relies on hand crafted features, whereas deep learning automatically learns features which are relevant to a task, and typically has much greater capacity for abstraction. Further, the filter banks and features generated from a CNN do not require the next two steps (feature selection and machine learning for classification), as the last layer of a CNN generates class labels. However, a limitation to deep learning is the requirement of a large amount of training data, and the computational complexity of handling a large amount of data.

Feature Selection

Feature selection aims to minimize the subset of features used from the original set of extracted features, such that the generalizability of the model is maximized. There are many factors that must be considered when choosing which features to use, including the size of the dataset you have. It has been observed the error of a classifier decreases and then increased as the number of features included increase.[97] There have been different studies into the optimal number of features to include, however the consensus is the number varies largely depending on the task.[98]

Methods to perform feature selection include forward selection and backward selection. In forward selection, features are iteratively added to the model based on the feature which increases the performance metric the most, whereas backward selection starts with the entire set of features and iteratively removes features which leaves the highest performing model. Further methods include dimension reduction by using tools such as principle component analysis or independent component analysis which aim to explain variance within the data, however, the interpretability of the features can be complicated while using these approaches. It is also important to select features which will be steady in different circumstances; for example, it is undesirable to include features that are highly dependent on user input, such as a segmentation. As such, a step can be included to select only features which are steady through different observer segmentations. To do this, a metric such as the intraclass correlation coefficient (ICC) may be used to compare the ranking of features across different segmentations.

Machine Learning

Once features are chosen to represent an image, or region in an image, machine learning can be used to determine how to combine the information from different features to minimize a cost function. The simplest example of this is a linear regression, where you want to minimize the sum of the squares of the distance from the line of best fit to each data point. When you have more than one feature, this task becomes more complicated.

Machine learning approaches can generally be classified as supervised, or unsupervised learning. Unsupervised approaches look for patterns within a feature set, creating clusters of features, without knowing an associated label for each cluster. Supervised approaches look to separate the feature space based on a label associated with each data point. Popular supervised machine learning algorithms used in medical imaging include logistic regression, linear discriminants, support vector machines, decision trees and neural networks.[99]

A logistic regression is used for classification problems by estimating the probabilities for each class using a logistic function, also known as a sigmoid function, as the activation function which maps your algorithm value to a probability between [0, 1]. To train a logistic regression, the cross-entropy cost function is typically used. Similarly, a support vector machine aims to find the hyperplane which separates two classes, while maximizing the distance from the plane to each of the closest points, or support vectors. In cases which the data are not linearly separable, a non-linear kernel can be used to map the data to a linear space, as well as an application of a soft-margin. To train a support vector machine, the cost function rewards being at least one unit away from zero in the cost space, which aims to minimize the data points which lay within a margin to the separating hyperplane. Due to the inclusion of distance to points in space in the cost function, standardization or normalization of the features is an important pre-processing step. Standardization is performed by subtracting the feature mean and dividing by the standard deviation, while normalization is performed to rescale all data to the range of [0, 1]. Other classifiers include decision trees which learn decision rules for each feature to classify based on features, nearest neighbor, which classifies based on how similar a data point is to previously observed data, and a neural networks train to learn the combination of features and weights to predict the class. Each of these have different underlying algorithms, but all aim to minimize a cost function, such that when presented with a new data point they can predict the associated label as accurately as possible.

1.6.2 Challenges and Limitations

One of the largest challenges in texture analysis for medical imaging is deciding which of the methods discussed in Section 1.6.1 to implement. As is evident, there are a high number of combinations and permutations of texture features, feature selection and machine learning methods. There is no standard combination that is the “best” to employ due to the fact that each medical image analysis problem is unique. Therefore, one of the most important parts of any texture analysis or machine learning project is managing the dataset to be able to validate and eventually test your specific method. If done correctly, a training, validation and testing split allows for confidence in the performance of the model created. For example, many machine learning methods may be used to generate a model from the training set, then be applied to the validation set. The highest performing model as determined on the validation set, can then be applied to the testing set to report the overall performance of the model generated. This ensures a decision on the best machine learning algorithm was determined experimentally, greatly reducing the likelihood the final model has been over fit to the data.

Another important challenge is the generalizability of the models created using texture analysis. To obtain the best results, homogenous collection of the data is desired, where the same imaging protocol is employed across all subjects. However, to translate the model, differences across sites must be understood and considered. It is known the protocol parameters (slice thickness, voxel spacing), reconstruction kernel, and scanner vendor all effect texture features.[100-102] The robustness of features across different scanners can be studied, including measuring feature robustness as a metric within feature selection. There is also recent work being done to standardize features across scanners.[103]

1.6.3 Applications in Lung Imaging

Computer-aided diagnosis has been around since before the digitization of medical images, where a pattern recognition approach was introduced to preprocess images, extract features and perform classification.[104] Within lung imaging, a large number of studies applied feature analysis to chest x-ray images in a series of studies on “Image feature analysis and computer-aided diagnosis in digital radiography” from Dr. MacMahon and colleagues.[105-112]

More recently, texture analysis has been applied to CT images for the detection and classification of pulmonary nodules,[113-116] which is also referred to as radiomics. Here, it has been observed that in addition to analyzing the tumour volume, it is beneficial to analyze the parenchymal tissue.[117, 118] Texture analysis has also been applied to create automated lung disease classification, including fibrosis,[119] pneumonia[120] and obstructive lung disease such as emphysema.[121-125] All of these studies employed slightly different approaches to texture analysis, with different ground truths, however demonstrate the ability of texture analysis to capture important information within thoracic CT images.

1.7 Thesis Hypotheses and Objectives

Hyperpolarized gas MRI has been used to provide unique functional information in patients with COPD, and has been shown to relate to important patient outcomes and have the potential to guide treatment. Unfortunately, this specialized information is currently limited to a small number of research centres due to the high cost of hyperpolarization equipment and gas. This is converse to widely available thoracic CT, which provides high-resolution anatomical images. The overarching objective of this thesis is to use texture analysis and machine learning to generate the functional information contained within hyperpolarized gas MRI, from a single-volume, non-contrast enhanced thoracic CT. To do this, hyperpolarized gas MRI were registered to thoracic CT to provide the ground truth training label. First and second order features were then extracted from each volume of interest, which were used to create a machine learning model. We hypothesized that the structural information contained within a single-volume breath hold CT can inform on regional lung function. This hypothesis has a basis in previous observations using thoracic CT, such as the airway and vasculature changes associated with COPD, and the previously reported spatial overlap between CT emphysema measures and ventilation defects. The objective of Chapter 2 was to development a texture analysis pipeline, and apply the pipeline is a small cohort as proof-of-concept.

The objectives in Chapter 3, were to apply improve upon the methods developed in Chapter 2, and apply this pipeline in a larger set of patients. To do this texture features, the volume of interest size, and the sampling method were optimized within the training set of this cohort. The optimal performing model was then applied in the testing set of 27 participants. We hypothesized that the model predicted ventilation maps would qualitatively and quantitatively relate to ground truth MRI ventilation maps, as well as important clinical measures.

In Chapter 4, I provide a summary of the impact and conclusions from Chapter 2 and 3, as well as discuss limitations and future steps to build upon the research presented in this thesis.

1.8 References

1. Mathers CD, Loncar D. Projections of global mortality and burden of disease from 2002 to 2030. PLoS Med. 2006;3(11):e442.

2. Lozano R, Naghavi M, Foreman K, et al. Global and regional mortality from 235 causes of death for 20 age groups in 1990 and 2010: a systematic analysis for the Global Burden of Disease Study 2010. Lancet. 2012;380(9859):2095-128.

3. Vogelmeier CF, Criner GJ, Martinez FJ, et al. Global Strategy for the Diagnosis, Management, and Prevention of Chronic Obstructive Lung Disease 2017 Report. GOLD Executive Summary. Am J Respir Crit Care Med. 2017;195(5):557-82.

4. Health Indicators 2008. Ottawa: Canadian Institute for Health Information, 2008. Report No.

5. Chapman KR, Bourbeau J, Rance L. The burden of COPD in Canada: results from the Confronting COPD survey. Respir Med. 2003;97 Suppl C:S23-31.

6. Jost RG, Sagel SS, Stanley RJ, Levitt RG. Computed tomography of the thorax. Radiology. 1978;126(1):125-36.

7. Rosenblum LJ, Mauceri RA, Wellenstein DE, Bassano DA, Cohen WN, Heitzman ER. Computed tomography of the lung. Radiology. 1978;129(2):521-4.

8. Goddard PR, Nicholson EM, Laszlo G, Watt I. Computed tomography in pulmonary emphysema. Clin Radiol. 1982;33(4):379-87.

9. Bergin C, Muller N, Nichols DM, et al. The diagnosis of emphysema. A computed tomographic-pathologic correlation. Am Rev Respir Dis. 1986;133(4):541-6.

10. Foster WL, Jr., Pratt PC, Roggli VL, Godwin JD, Halvorsen RA, Jr., Putman CE. Centrilobular emphysema: CT-pathologic correlation. Radiology. 1986;159(1):27-32.

11. West J, Luks A. Respiratory Physiology: The Essentials Wolters Kluwer; 2016.

12. Ochs M, Nyengaard JR, Jung A, et al. The number of alveoli in the human lung. Am J Respir Crit Care Med. 2004;169(1):120-4.

13. Hogg JC. Pathophysiology of airflow limitation in chronic obstructive pulmonary disease. Lancet. 2004;364(9435):709-21.

14. Woods JC, Choong CK, Yablonskiy DA, et al. Hyperpolarized 3He diffusion MRI and histology in pulmonary emphysema. Magn Reson Med. 2006;56(6):1293-300.

15. Leopold JG, Gough J. The centrilobular form of hypertrophic emphysema and its relation to chronic bronchitis. Thorax. 1957;12(3):219-35.

16. Weibel ER. Principles and methods for the morphometric study of the lung and other organs. Lab Invest. 1963;12:131-55.

17. Heemskerk-Gerritsen BA, Dijkman JH, Ten Have-Opbroek AA. Stereological methods: a new approach in the assessment of pulmonary emphysema. Microsc Res Tech. 1996;34(6):556-62.

18. Wiebe BM, Laursen H. Lung morphometry by unbiased methods in emphysema: bronchial and blood vessel volume, alveolar surface area and capillary length. APMIS. 1998;106(6):651-6.

19. Hogg JC, Macklem PT, Thurlbeck WM. Site and nature of airway obstruction in chronic obstructive lung disease. N Engl J Med. 1968;278(25):1355-60.

20. Reid L. Measurement of the bronchial mucous gland layer: a diagnostic yardstick in chronic bronchitis. Thorax. 1960;15:132-41.

21. Thurlbeck WM, Angus GE. A Distribution Curve for Chronic Bronchitis. Thorax. 1964;19:436-42.

22. Dunnill MS, Massarella GR, Anderson JA. A comparison of the quantitative anatomy of the bronchi in normal subjects, in status asthmaticus, in chronic bronchitis, and in emphysema. Thorax. 1969;24(2):176-9.

23. Mitchell RS, Stanford RE, Johnson JM, Silvers GW, Dart G, George MS. The morphologic features of the bronchi, bronchioles, and alveoli in chronic airway obstruction: a clinicopathologic study. Am Rev Respir Dis. 1976;114(1):137-45.

24. Vestbo J, Prescott E, Lange P. Association of chronic mucus hypersecretion with FEV1 decline and chronic obstructive pulmonary disease morbidity. Copenhagen City Heart Study Group. Am J Respir Crit Care Med. 1996;153(5):1530-5.

25. Crapo RO. Pulmonary-function testing. N Engl J Med. 1994;331(1):25-30.

26. Quanjer PH, Stanojevic S, Cole TJ, et al. Multi-ethnic reference values for spirometry for the 3-95-yr age range: the global lung function 2012 equations. Eur Respir J. 2012;40(6):1324-43.

27. Miller MR, Hankinson J, Brusasco V, et al. Standardisation of spirometry. Eur Respir J. 2005;26(2):319-38.

28. Wanger J, Clausen JL, Coates A, et al. Standardisation of the measurement of lung volumes. Eur Respir J. 2005;26(3):511-22.

29. Macintyre N, Crapo RO, Viegi G, et al. Standardisation of the single-breath determination of carbon monoxide uptake in the lung. Eur Respir J. 2005;26(4):720-35.

30. Jones PW, Quirk FH, Baveystock CM, Littlejohns P. A self-complete measure of health status for chronic airflow limitation. The St. George's Respiratory Questionnaire. Am Rev Respir Dis. 1992;145(6):1321-7.

31. Enright PL, Sherrill DL. Reference equations for the six-minute walk in healthy adults. Am J Respir Crit Care Med. 1998;158(5 Pt 1):1384-7.

32. Laboratories ACoPSfCPF. ATS statement: guidelines for the six-minute walk test. Am J Respir Crit Care Med2002. p. 111-7.

33. Carter R, Holiday DB, Nwasuruba C, Stocks J, Grothues C, Tiep B. 6-minute walk work for assessment of functional capacity in patients with COPD. Chest. 2003;123(5):1408-15.

34. Wise RA, Brown CD. Minimal clinically important differences in the six-minute walk test and the incremental shuttle walking test. COPD. 2005;2(1):125-9.

35. Redelmeier DA, Bayoumi AM, Goldstein RS, Guyatt GH. Interpreting small differences in functional status: the Six Minute Walk test in chronic lung disease patients. Am J Respir Crit Care Med. 1997;155(4):1278-82.

36. Muller NL, Staples CA, Miller RR, Abboud RT. "Density mask". An objective method to quantitate emphysema using computed tomography. Chest. 1988;94(4):782-7.

37. Gevenois PA, De Vuyst P, de Maertelaer V, et al. Comparison of computed density and microscopic morphometry in pulmonary emphysema. Am J Respir Crit Care Med. 1996;154(1):187-92.

38. Madani A, De Maertelaer V, Zanen J, Gevenois PA. Pulmonary emphysema: radiation dose and section thickness at multidetector CT quantification--comparison with macroscopic and microscopic morphometry. Radiology. 2007;243(1):250-7.

39. Dirksen A, Piitulainen E, Parr DG, et al. Exploring the role of CT densitometry: a randomised study of augmentation therapy in alpha1-antitrypsin deficiency. Eur Respir J. 2009;33(6):1345-53.

40. Mishima M, Hirai T, Itoh H, et al. Complexity of terminal airspace geometry assessed by lung computed tomography in normal subjects and patients with chronic obstructive pulmonary disease. Proc Natl Acad Sci U S A. 1999;96(16):8829-34.

41. McDonough JE, Yuan R, Suzuki M, et al. Small-airway obstruction and emphysema in chronic obstructive pulmonary disease. N Engl J Med. 2011;365(17):1567-75.

42. Diaz AA, Valim C, Yamashiro T, et al. Airway count and emphysema assessed by chest CT imaging predicts clinical outcome in smokers. Chest. 2010;138(4):880-7.

43. Han MK, Kazerooni EA, Lynch DA, et al. Chronic obstructive pulmonary disease exacerbations in the COPDGene study: associated radiologic phenotypes. Radiology. 2011;261(1):274-82.

44. Alford SK, van Beek EJ, McLennan G, Hoffman EA. Heterogeneity of pulmonary perfusion as a mechanistic image-based phenotype in emphysema susceptible smokers. Proc Natl Acad Sci U S A. 2010;107(16):7485-90.

45. Estepar RS, Kinney GL, Black-Shinn JL, et al. Computed tomographic measures of pulmonary vascular morphology in smokers and their clinical implications. Am J Respir Crit Care Med. 2013;188(2):231-9.

46. Diaz AA, Maselli DJ, Rahaghi F, et al. Pulmonary vascular pruning in smokers with bronchiectasis. ERJ Open Res. 2018;4(4).

47. Bergin CJ, Glover GM, Pauly J. Magnetic resonance imaging of lung parenchyma. J Thorac Imaging. 1993;8(1):12-7.

48. Ma W, Sheikh K, Svenningsen S, et al. Ultra-short echo-time pulmonary MRI: evaluation and reproducibility in COPD subjects with and without bronchiectasis. J Magn Reson Imaging. 2015;41(5):1465-74.

49. Bergin CJ, Noll DC, Pauly JM, Glover GH, Macovski A. MR imaging of lung parenchyma: a solution to susceptibility. Radiology. 1992;183(3):673-6.

50. Ohno Y, Koyama H, Yoshikawa T, et al. T2* measurements of 3-T MRI with ultrashort TEs: capabilities of pulmonary function assessment and clinical stage classification in smokers. AJR Am J Roentgenol. 2011;197(2):W279-85.

51. Ohno Y, Koyama H, Yoshikawa T, et al. Pulmonary high-resolution ultrashort TE MR imaging: Comparison with thin-section standard- and low-dose computed tomography for the assessment of pulmonary parenchyma diseases. J Magn Reson Imaging. 2016;43(2):512-32.

52. Park EA, Goo JM, Park SJ, et al. Chronic obstructive pulmonary disease: quantitative and visual ventilation pattern analysis at xenon ventilation CT performed by using a dual-energy technique. Radiology. 2010;256(3):985-97.

53. Thieme SF, Hoegl S, Nikolaou K, et al. Pulmonary ventilation and perfusion imaging with dual-energy CT. Eur Radiol. 2010;20(12):2882-9.

54. Guerrero T, Sanders K, Castillo E, et al. Dynamic ventilation imaging from four-dimensional computed tomography. Phys Med Biol. 2006;51(4):777-91.

55. Pan T, Lee TY, Rietzel E, Chen GT. 4D-CT imaging of a volume influenced by respiratory motion on multi-slice CT. Med Phys. 2004;31(2):333-40.

56. Reinhardt JM, Ding K, Cao K, Christensen GE, Hoffman EA, Bodas SV. Registration-based estimates of local lung tissue expansion compared to xenon CT measures of specific ventilation. Med Image Anal. 2008;12(6):752-63.

57. Bodduluri S, Newell JD, Jr., Hoffman EA, Reinhardt JM. Registration-based lung mechanical analysis of chronic obstructive pulmonary disease (COPD) using a supervised machine learning framework. Acad Radiol. 2013;20(5):527-36.

58. Yamamoto T, Kabus S, Klinder T, et al. Investigation of four-dimensional computed tomography-based pulmonary ventilation imaging in patients with emphysematous lung regions. Phys Med Biol. 2011;56(7):2279-98.

59. Yamamoto T, Kabus S, Lorenz C, et al. 4D CT lung ventilation images are affected by the 4D CT sorting method. Med Phys. 2013;40(10):101907.

60. Albert MS, Cates GD, Driehuys B, et al. Biological magnetic resonance imaging using laser-polarized 129Xe. Nature. 1994;370(6486):199-201.

61. Kirby M, Heydarian M, Svenningsen S, et al. Hyperpolarized 3He magnetic resonance functional imaging semiautomated segmentation. Acad Radiol. 2012;19(2):141-52.

62. Salerno M, de Lange EE, Altes TA, Truwit JD, Brookeman JR, Mugler JP, 3rd. Emphysema: hyperpolarized helium 3 diffusion MR imaging of the lungs compared with spirometric indexes--initial experience. Radiology. 2002;222(1):252-60.

63. Ley S, Zaporozhan J, Morbach A, et al. Functional evaluation of emphysema using diffusion-weighted 3Helium-magnetic resonance imaging, high-resolution computed tomography, and lung function tests. Invest Radiol. 2004;39(7):427-34.

64. Parraga G, Ouriadov A, Evans A, et al. Hyperpolarized 3He ventilation defects and apparent diffusion coefficients in chronic obstructive pulmonary disease: preliminary results at 3.0 Tesla. Invest Radiol. 2007;42(6):384-91.

65. Shukla Y, Wheatley A, Kirby M, et al. Hyperpolarized 129Xe magnetic resonance imaging: tolerability in healthy volunteers and subjects with pulmonary disease. Acad Radiol. 2012;19(8):941-51.

66. Mathew L, Evans A, Ouriadov A, et al. Hyperpolarized 3He magnetic resonance imaging of chronic obstructive pulmonary disease: reproducibility at 3.0 tesla. Acad Radiol. 2008;15(10):1298-311.

67. Driehuys B, Martinez-Jimenez S, Cleveland ZI, et al. Chronic obstructive pulmonary disease: safety and tolerability of hyperpolarized 129Xe MR imaging in healthy volunteers and patients. Radiology. 2012;262(1):279-89.

68. Kirby M, Svenningsen S, Owrangi A, et al. Hyperpolarized 3He and 129Xe MR imaging in healthy volunteers and patients with chronic obstructive pulmonary disease. Radiology. 2012;265(2):600-10.

69. Kirby M, Owrangi A, Svenningsen S, et al. On the role of abnormal DL(CO) in ex-smokers without airflow limitation: symptoms, exercise capacity and hyperpolarised helium-3 MRI. Thorax. 2013;68(8):752-9.

70. Kirby M, Pike D, Coxson HO, McCormack DG, Parraga G. Hyperpolarized (3)He ventilation defects used to predict pulmonary exacerbations in mild to moderate chronic obstructive pulmonary disease. Radiology. 2014;273(3):887-96.

71. Kirby M, Kanhere N, Etemad-Rezai R, McCormack DG, Parraga G. Hyperpolarized helium-3 magnetic resonance imaging of chronic obstructive pulmonary disease exacerbation. J Magn Reson Imaging. 2013;37(5):1223-7.

72. Capaldi DP, Zha N, Guo F, et al. Pulmonary Imaging Biomarkers of Gas Trapping and Emphysema in COPD: (3)He MR Imaging and CT Parametric Response Maps. Radiology. 2016;279(2):597-608.

73. Virgincar RS, Cleveland ZI, Kaushik SS, et al. Quantitative analysis of hyperpolarized 129Xe ventilation imaging in healthy volunteers and subjects with chronic obstructive pulmonary disease. NMR Biomed. 2013;26(4):424-35.

74. Kirby M, Ouriadov A, Svenningsen S, et al. Hyperpolarized 3He and 129Xe magnetic resonance imaging apparent diffusion coefficients: physiological relevance in older never- and ex-smokers. Physiol Rep. 2014;2(7).

75. Stewart NJ, Chan HF, Hughes PJC, et al. Comparison of (3) He and (129) Xe MRI for evaluation of lung microstructure and ventilation at 1.5T. J Magn Reson Imaging. 2018.

76. Tahir BA, Hughes PJC, Robinson SD, et al. Spatial Comparison of CT-Based Surrogates of Lung Ventilation With Hyperpolarized Helium-3 and Xenon-129 Gas MRI in Patients Undergoing Radiation Therapy. Int J Radiat Oncol Biol Phys. 2018;102(4):1276-86.

77. Haralick RM, Shanmugam K, Dinstein Ih. Textural Features for Image Classification. IEEE Transactions on Systems, Man and Cybernetics. 1973;SMC-3(6):610-21.

78. Doi K. Computer-aided diagnosis in medical imaging: historical review, current status and future potential. Comput Med Imaging Graph. 2007;31(4-5):198-211.

79. Kittler J, Illingworth J, Foglein J. Threshold Selection Based on a Simple Image Statistic. Computer Vision Graphics and Image Processing. 1985;30(2):125-47.

80. Sahoo PK, Soltani S, Wong AKC, Chen YC. A Survey of Thresholding Techniques. Computer Vision Graphics and Image Processing. 1988;41(2):233-60.

81. Pavlidis T, Liow YT. Integrating Region Growing and Edge-Detection. Ieee Transactions on Pattern Analysis and Machine Intelligence. 1990;12(3):225-33.

82. Haralick RM, Shapiro LG. Image Segmentation Techniques. Computer Vision Graphics and Image Processing. 1985;29(1):100-32.

83. Beucher S, Lantuejoul C. Use of Watersheds in Contour Detection. Internaitonal workshop on image processing, real-time edge and motion detection; France1979.

84. Coleman GB, Andrews HC. Image Segmentation by Clustering. Proceedings of the Ieee. 1979;67(5):773-85.

85. Bezdek JC, Ehrlich R, Full W. Fcm - the Fuzzy C-Means Clustering-Algorithm. Computers & Geosciences. 1984;10(2-3):191-203.

86. McInerney T, Terzopoulos D. Deformable models in medical image analysis. Proceedings of the Ieee Workshop on Mathematical Methods in Biomedical Image Analysis. 1996:171-80.

87. Sluimer I, Prokop M, van Ginneken B. Toward automated segmentation of the pathological lung in CT. IEEE Trans Med Imaging. 2005;24(8):1025-38.

88. Armato SG, 3rd, Sensakovic WF. Automated lung segmentation for thoracic CT impact on computer-aided diagnosis. Acad Radiol. 2004;11(9):1011-21.

89. Sun S, Bauer C, Beichel R. Automated 3-D segmentation of lungs with lung cancer in CT data using a novel robust active shape model approach. IEEE Trans Med Imaging. 2012;31(2):449-60.

90. Ronneberger O, Fischer P, Brox T. U-Net: Convolutional Networks for Biomedical Image Segmentation. Medical Image Computing and Computer-Assisted Intervention, Pt Iii. 2015;9351:234-41.

91. Milletari F, Navab N, Ahmadi SA. V-Net: Fully Convolutional Neural Networks for Volumetric Medical Image Segmentation. Proceedings of 2016 Fourth International Conference on 3d Vision (3dv). 2016:565-71.

92. Gibson E, Li WQ, Sudre C, et al. NiftyNet: a deep-learning platform for medical imaging. Computer Methods and Programs in Biomedicine. 2018;158:113-22.

93. Vercauteren T, Pennec X, Perchant A, Ayache N. Diffeomorphic demons: efficient non-parametric image registration. Neuroimage. 2009;45(1 Suppl):S61-72.

94. Heinrich MP, Jenkinson M, Bhushan M, et al. MIND: modality independent neighbourhood descriptor for multi-modal deformable registration. Med Image Anal. 2012;16(7):1423-35.

95. Tang X. Texture information in run-length matrices. IEEE Trans Image Process. 1998;7(11):1602-9.

96. Depeursinge A, Foncubierta-Rodriguez A, Van De Ville D, Muller H. Three-dimensional solid texture analysis in biomedical imaging: review and opportunities. Med Image Anal. 2014;18(1):176-96.

97. Hughes G. On the mean accuracy of statistical pattern recognizers. IEEE Trans Info Theory. 1968;14(1):55-63.

98. Hua JP, Xiong ZX, Lowey J, Suh E, Dougherty ER. Optimal number of features as a function of sample size for various classification rules. Bioinformatics. 2005;21(8):1509-15.

99. Erickson BJ, Korfiatis P, Akkus Z, Kline TL. Machine Learning for Medical Imaging. Radiographics. 2017;37(2):505-15.

100. Yasaka K, Akai H, Mackin D, et al. Precision of quantitative computed tomography texture analysis using image filtering: A phantom study for scanner variability. Medicine (Baltimore). 2017;96(21):e6993.

101. Shafiq-Ul-Hassan M, Zhang GG, Latifi K, et al. Intrinsic dependencies of CT radiomic features on voxel size and number of gray levels. Med Phys. 2017;44(3):1050-62.

102. Mackin D, Fave X, Zhang L, et al. Measuring Computed Tomography Scanner Variability of Radiomics Features. Invest Radiol. 2015;50(11):757-65.

103. Andrearczyk V, Depeursinge A, Muller H, editors. Learning Cross-Protocol Radiomics and Deep Feature Standardization from CT Images of Texture Phantoms. SPIE Medical Imaging; 2019; San Diego.

104. Sutton RN, Hall EL. Texture Measures for Automatic Classification of Pulmonary-Disease. Ieee Transactions on Computers. 1972;C 21(7):667-+.

105. Chan HP, Doi K, Galhotra S, Vyborny CJ, MacMahon H, Jokich PM. Image feature analysis and computer-aided diagnosis in digital radiography. I. Automated detection of microcalcifications in mammography. Med Phys. 1987;14(4):538-48.

106. Katsuragawa S, Doi K, MacMahon H. Image feature analysis and computer-aided diagnosis in digital radiography: detection and characterization of interstitial lung disease in digital chest radiographs. Med Phys. 1988;15(3):311-9.

107. Giger ML, Doi K, MacMahon H. Image feature analysis and computer-aided diagnosis in digital radiography. 3. Automated detection of nodules in peripheral lung fields. Med Phys. 1988;15(2):158-66.

108. Katsuragawa S, Doi K, MacMahon H. Image feature analysis and computer-aided diagnosis in digital radiography: classification of normal and abnormal lungs with interstitial disease in chest images. Med Phys. 1989;16(1):38-44.

109. Nakamori N, Doi K, Sabeti V, MacMahon H. Image feature analysis and computer-aided diagnosis in digital radiography: automated analysis of sizes of heart and lung in chest images. Med Phys. 1990;17(3):342-50.

110. Katsuragawa S, Doi K, Nakamori N, MacMahon H. Image feature analysis and computer-aided diagnosis in digital radiography: effect of digital parameters on the accuracy of computerized analysis of interstitial disease in digital chest radiographs. Med Phys. 1990;17(1):72-8.

111. Sanada S, Doi K, MacMahon H. Image feature analysis and computer-aided diagnosis in digital radiography: automated delineation of posterior ribs in chest images. Med Phys. 1991;18(5):964-71.

112. Sanada S, Doi K, MacMahon H. Image feature analysis and computer-aided diagnosis in digital radiography: automated detection of pneumothorax in chest images. Med Phys. 1992;19(5):1153-60.

113. Armato SG, 3rd, Altman MB, Wilkie J, et al. Automated lung nodule classification following automated nodule detection on CT: a serial approach. Med Phys. 2003;30(6):1188-97.

114. McNitt-Gray MF, Hart EM, Wyckoff N, Sayre JW, Goldin JG, Aberle DR. A pattern classification approach to characterizing solitary pulmonary nodules imaged on high resolution CT: preliminary results. Med Phys. 1999;26(6):880-8.

115. Han F, Wang H, Zhang G, et al. Texture feature analysis for computer-aided diagnosis on pulmonary nodules. J Digit Imaging. 2015;28(1):99-115.

116. Dhara AK, Mukhopadhyay S, Dutta A, Garg M, Khandelwal N. A Combination of Shape and Texture Features for Classification of Pulmonary Nodules in Lung CT Images. J Digit Imaging. 2016;29(4):466-75.

117. Dilger SK, Uthoff J, Judisch A, et al. Improved pulmonary nodule classification utilizing quantitative lung parenchyma features. J Med Imaging (Bellingham). 2015;2(4):041004.

118. Beig N, Khorrami M, Alilou M, et al. Perinodular and Intranodular Radiomic Features on Lung CT Images Distinguish Adenocarcinomas from Granulomas. Radiology. 2019;290(3):783-92.

119. Sluimer IC, Prokop M, Hartmann I, van Ginneken B. Automated classification of hyperlucency, fibrosis, ground glass, solid, and focal lesions in high-resolution CT of the lung. Med Phys. 2006;33(7):2610-20.

120. Korfiatis P, Kalogeropoulou C, Karahaliou A, Kazantzi A, Skiadopoulos S, Costaridou L. Texture classification-based segmentation of lung affected by interstitial pneumonia in high-resolution CT. Med Phys. 2008;35(12):5290-302.

121. Park YS, Seo JB, Kim N, et al. Texture-based quantification of pulmonary emphysema on high-resolution computed tomography: comparison with density-based quantification and correlation with pulmonary function test. Invest Radiol. 2008;43(6):395-402.

122. Xu Y, Sonka M, McLennan G, Guo J, Hoffman EA. MDCT-based 3-D texture classification of emphysema and early smoking related lung pathologies. IEEE Trans Med Imaging. 2006;25(4):464-75.

123. Ginsburg SB, Lynch DA, Bowler RP, Schroeder JD. Automated texture-based quantification of centrilobular nodularity and centrilobular emphysema in chest CT images. Acad Radiol. 2012;19(10):1241-51.

124. Yang J, Angelini ED, Balte PP, et al. Unsupervised Discovery of Spatially-Informed Lung Texture Patterns for Pulmonary Emphysema: The MESA COPD Study. Med Image Comput Comput Assist Interv. 2017;10433:116-24.

125. Chabat F, Yang GZ, Hansell DM. Obstructive lung diseases: texture classification for differentiation at CT. Radiology. 2003;228(3):871-7.

CHAPTER 2

2 TEXTURE ANALYSIS OF THORACIC CT TO PREDICT HYPERPOLARIZED GAS MRI LUNG FUNCTION

To develop a pipeline for predicting hyperpolarized gas MRI ventilation based on texture analysis of thoracic CT, a small cohort of COPD patients were evaluated. Predicted ventilation maps were compared to ground truth hyperpolarized gas MRI ventilation.

The contents of this chapter were accepted as conference proceedings in SPIE Medical Imaging and permission to reproduce the article was granted by SPIE: A Westcott, D.P.I Capaldi, D.G McCormack, A Fenster and G Parraga. SPIE Medical Imaging 2019.

2.1 Introduction

Pulmonary imaging provides a unique opportunity to guide treatment and monitor disease progression in patients with chronic obstructive pulmonary disease (COPD). Currently, such regional information can be gleaned using contrast-enhanced X-ray computed tomography (CT), typically by using inhaled xenon gas with dual energy CT, at two different inspiration volumes, or free breathing volumetric CT image acquisition (4DCT) that employ advanced registration and analysis techniques.[1]

Recently, hyperpolarized gas MRI has been developed and exploited in COPD patients because it does not employ ionizing radiation, which augers well for serial imaging studies. Hyperpolarized ^{3}He and ^{129}Xe MRI have been shown to be reproducible and measurements or biomarkers derived using both approaches are sensitive to changes over short periods of time,[2, 3] as well as having the potential to guide treatment such as bronchoscopic lung volume reduction.[4] MRI ventilation information and ventilation defects can be quantified using the ventilation defect percent (VDP), which quantifies the volume of the lung not ventilated or poorly ventilated during a breath-hold scan of 8-12s.[5] Although the functional information hyperpolarized gas MRI provides is unique, the method is limited to research centres of excellence, which limits its clinical translation and use in multi-centre clinical cohort studies and clinical trials. Moreover, CT and thoracic CT protocols are universally available and this has facilitated the acquisition of CT in large cohort studies such as

COPDGene,[6] ECLIPSE,[7] SPIROMICS,[8] and CANCold,[9] which have together resulted in tens of thousands of thoracic CT images acquired in COPD patients for analysis.[10]

We postulated that by combining the use of texture analysis and machine learning, the ventilation information provided by hyperpolarized gas MRI could be transferred directly to thoracic CT acquired at the same breath-hold volume. The acquisition of a large number of MRI-CT pairs in the cohort study TinCAN,[11] provides an opportunity to train and test a machine learning approach to distinguishing ventilated from non-ventilated regions based on CT.

Therefore, the aim of this research was to develop and evaluate novel texture analysis tools to be used on CT images, using hyperpolarized gas MRI to determine the ground truth label. We hypothesized that a model utilizing first and second order features can be developed to classify CT regions as ventilated or non-ventilated based on hyperpolarized gas MRI ventilation maps.

2.2 Materials and Methods

2.2.1 Study Subjects and Image Acquisition

Subjects with a confirmed diagnosis of COPD provided informed written consent to a study protocol approved by a local research ethics board and Health Canada.[11] These participants have been extensively investigated in a longitudinal cohort study.[12] ^{1}H and ^{3}He MRI were performed on a 3T whole-body system (MR750 Discovery, General Electric Health Care [GEHC], Milwaukee, WI) as previously described.[11] Thoracic CT images were also acquired as previously described[11] on a 64-slice Lightspeed VCT scanner (GEHC, Milwaukee, WI) (64 × 0.625 mm, 120 kVp, 100 effective mA, rotation time = 500 ms, and pitch = 1.0). For CT, ^{1}H and ^{3}He imaging the subject was scanned in the supine position in breath-hold after inhalation of a 1-L bag from functional residual capacity to match lung volumes between scans. 10 subjects displaying CT evidence of emphysema (CT RA_{950} >9), and with a high ventilation defect percent (VDP>12%) were randomly selected, and randomly split into a training (n=7) and test (n=3) set.

2.2.2 Proposed Pipeline

Figure 1 displays the pipeline developed to classify CT volumes-of-interest (VOI), based on breath-hold CT images, feature extraction, a trained feature classifier and hyperpolarized gas MRI as ground truth.

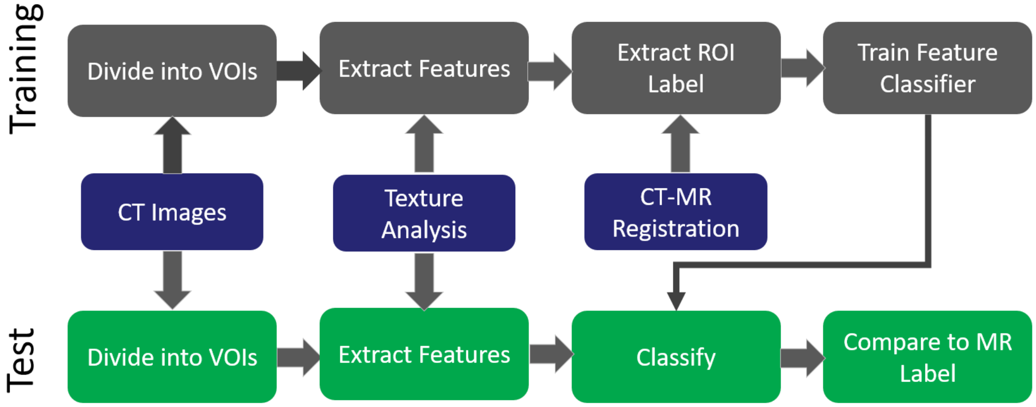

Figure 2-1: Proposed texture analysis pipeline for classifying CT volumes of interest (VOIs) into ventilation defects or ventilated.

2.2.3 Hyperpolarized MRI to Thoracic CT Registration

CT images were concatenated to 15mm thick slices to match the MRI dimensions. MRI data were resampled and cropped to result in 1.25x0.7mm pixels - the original CT x-y plane dimensions. ^{1}H MRI thoracic cavity images were registered to the CT using an affine landmark based registration, described previously for ^{1}H to ^{3}He registration (MATLAB R2018a; MathWorks, Natick, MA).[5] The calculated registration transformation was applied to the MR ventilation cluster maps, which were generated by registering the ^{1}H to ^{3}He and clustering using k-means clustering as previously described.[5] CT images were segmented using Pulmonary Workstation 2.0 (VIDA Diagnostics Inc., Coralville, IA).

CT and MR VOI were defined by applying a 3-dimensional grid, with isotropic dimensions of 15x15x15mm, on both the segmented CT and MR ventilation map. The MR ventilation map was labeled as background, ventilated and non-ventilated, with the label of a VOI being the mode, or most common, value. The grid was then shifted 7.5mm horizontally and 7.5mm vertically, to generate additional training samples, such that each voxel belongs to three separate VOI. This technique was further utilized when predicting the final label in the test set, as the mean was used between three overlapping 15x15x15 VOI, which then defined a 7.5x7.5x15mm region. Figure 2 shows the MR-CT registration and VOI extraction process.

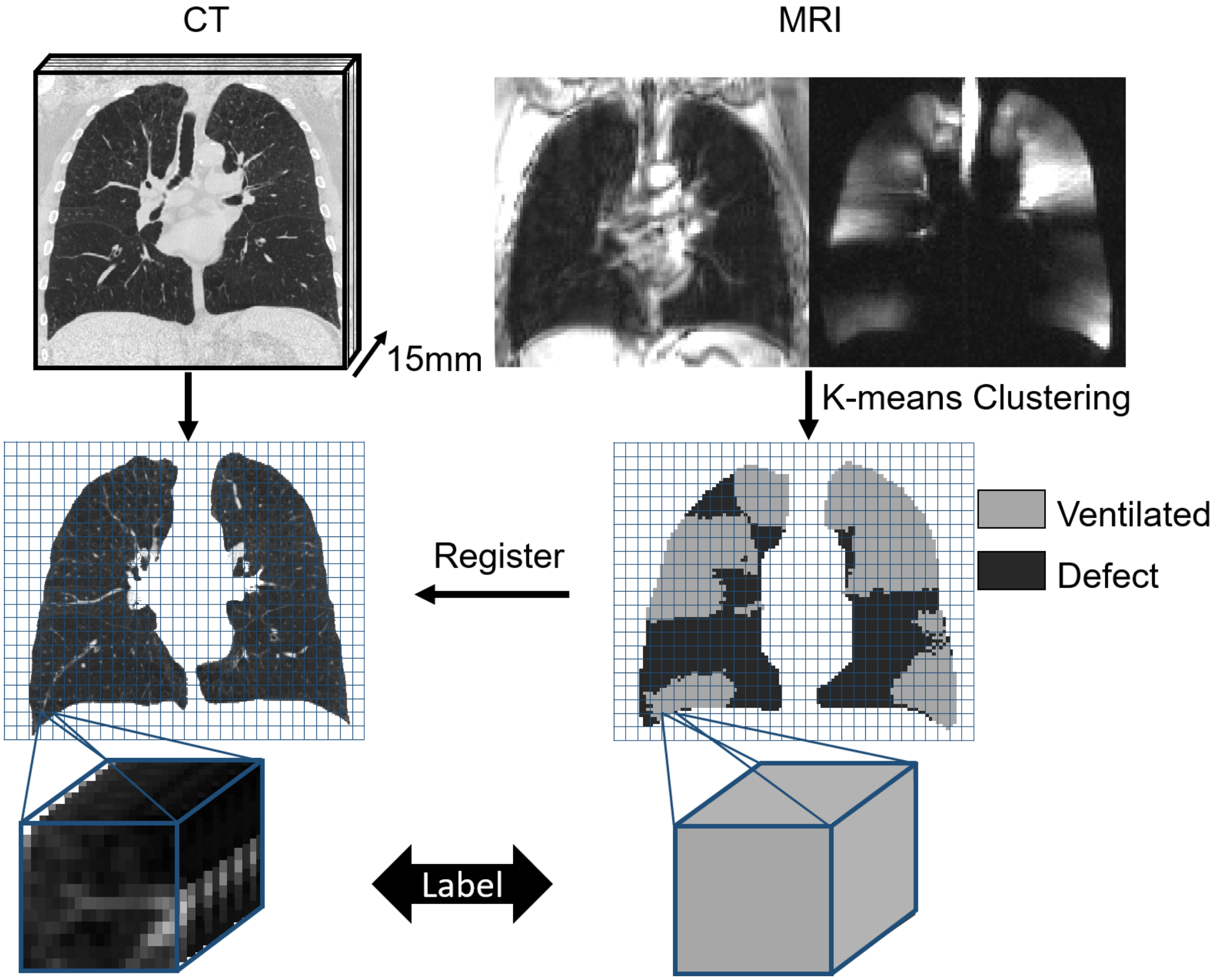

Figure 2-2: MRI to CT registration pipeline.
Displaying the 3-dimensional grid used to define CT VOIs and corresponding MR based ventilation label.

2.2.4 Thoracic CT Feature Extraction

First and second order features were extracted using a custom-built texture analysis software as described below (MATLAB R2018a; MathWorks, Natick, Mass).

First Order Statistics

The first order features used were mean CT density, standard deviation density, skewness, kurtosis, 95th percentile density, 15th percentile density (HU_{15}), relative area of the lung less than -950 HU (RA_{950}), relative area less than -910 HU (RA_{910}) and relative area less than -856 HU (RA_{856}).

Gray-level Co-occurrence Matrix

The gray level co-occurrence (GLCM) matrix is a measure of the number of times voxels of the same value appear next to each other.[13] The matrix was populated by classifying voxels based on Hounsfield Units (HU) into 20 bins from 0 to -1000 HU, each with a 50 HU size range. Using methodology previously described,[13] features were calculated as shown in the right side of Table 1, for the 13 unique 3-dimensional directions.

Cluster Volume Matrix

The run-length matrix is commonly used as a method to extract features from 2-dimensional images.[14] However, calculating run lengths in 3-dimensions becomes computationally intensive, and does not take into account regions that are fully, but not linearly, connected. Further, in COPD, cluster of low attenuating regions are clinically relevant.[15] Therefore, here we employed a combination of the run-length matrix with CT cluster analysis by creating the cluster volume matrix (CVM), for novel CT texture features. This is essentially a 3-dimensional extension of the run length matrix, where $p(i, j)$ is the number of clusters, and i is still the gray-level, but j is the 3-dimensional cluster size of the same gray-level. The features calculated from the CVM are the same as those calculated from a run-length matrix, as shown in the left column of Table 1. The matrix was populated by classifying into 40 HU wide groups between -500 and -1000, where all voxels greater than -500 were collapsed into a single group.

Table 2-1: Equations to calculate features from a gray-level run length matrix and to calculate features from a gray-level co-occurrence matrix.
$p(i,j)$ is an element of the gray-level run length matrix, where i corresponds to the image intensity, and j corresponds to the number of homogenous runs of length j and n_r is the total number of runs. $g(i,j)$ is an element of the co-occurrence matrix. $\mu = \sum_{i,j} i * g(i,j)$ is the mean, $\sigma = \sum_{i,j} g(i,j) * (i-\mu)^2$ is the variance.

CVM Feature	Equation	GLCM Feature	Equation
Short Run Emphasis (SRE)	$\frac{1}{n_r}\sum_{i,j}\frac{p(i,j)}{j^2}$	Energy	$\sum_{i,j} g(i,j)^2$
Long Run Emphasis (LRE)	$\frac{1}{n_r}\sum_{i,j} p(i,j) * j^2$	Entropy	$\sum_{i,j} -\log(g(i,j)) * g(i,j))$, if $g(i,j) \cong 0$ 0 if $g(i,j) = 0$
Gray-level Non-uniformity (GLNU)	$\frac{1}{n_r}\sum_{i}\left(\sum_{j} p(i,j)\right)^2$	Contrast	$\sum_{i,j} g(i,j) * (i-j)^2$
Run length Non-uniformity (RLNU)	$\frac{1}{n_r}\sum_{j}\left(\sum_{i} p(i,j)\right)^2$	Homogeneity	$\sum_{i,j}\frac{g(i,j)}{1+(i-j)^2}$
Run Percentage (RP)	$\frac{n_r}{\sum_{i,j} j * p(i,j)}$	Correlation	$\sum_{i,j}\frac{g(i,j) * (i-\mu) * (j-\mu)}{\sigma^2}$
Low gray-level run emphasis (LGRE)	$\frac{1}{n_r}\sum_{i,j}\frac{p(i,j)}{i^2}$		
High gray-level run emphasis (HGRE)	$\frac{1}{n_r}\sum_{i,j} p(i,j) * i^2$		
Short run low gray-level emphasis (SRLGE)	$\frac{1}{n_r}\sum_{i,j}\frac{p(i,j)}{i^2 * j^2}$		
Short run high gray-level emphasis (SRHGE)	$\frac{1}{n_r}\sum_{i,j} p(i,j) * \frac{i^2}{j^2}$		
Long run low gray-level emphasis (LRLGE)	$\frac{1}{n_r}\sum_{i,j} p(i,j) * \frac{j^2}{i^2}$		
Long run high-gray level emphasis (LRHGE)	$\frac{1}{n_r}\sum_{i,j} p(i,j) * j^2 * i^2$		

2.2.5 Training a Classification Model

In total there were 85 features extracted to describe each CT volume, which were then used as the input to the classifier model. To train the model we used an even number of ventilated and non-ventilated regions from each subject, randomly selecting ventilated regions to match the number of non-ventilated regions. To obtain a training accuracy, which could provide an adequate estimate of the entire dataset, the training set was trained in five iterations with each iteration being trained on 80% and tested on 20% of the training data, where the testing 20% is unique for each iteration. This 5-fold cross-validation training was performed using a logistic regression, linear support vector machine (SVM) and a quadratic SVM. To compare models, the mean accuracy of the 5-fold cross-validation was calculated and a receiver-operator-characteristic (ROC) curve was generated. From the ROC curve, the area under the curve (AUC) was also calculated as a global summary of the classifier performance.

2.3 Results

2.3.1 Study Subjects

Demographics, pulmonary function tests, CT and MR imaging measurements for ten subjects with COPD are provided in Table 2.

Table 2-2: COPD Subject demographics, pulmonary function tests, CT and MR imaging measurements

	Training (n=7)	**Test (n=3)**
Age years	72 (6)	81 (5)
Sex (M/F)	3/4	3/0
Pack Years	60 (40)	50 (20)
FEV_1 $\%_{pred}$	33 (7)	42 (13)
FEV_1/FVC	36 (8)	36 (7)
DL_{CO} $\%_{pred}$	30 (9)	29 (8)
RA_{950} %	21 (9)	21 (7)
VDP %	27 (7)	28 (2)

FEV_1=forced expiratory volume in 1 second; FEV_1/FVC=FEV_1 ratio with forced vital capacity; $\%_{pred}$=percent predicted; DL_{CO}=diffusing capacity for carbon monoxide; RA_{950}=relative area of CT histogram <-950 HU. VDP=ventilation defect percent.

2.3.2 Model Results

Three different classification algorithms were trained including logistic regression, linear SVM and quadratic SVM using ~20,000 VOI, with an even proportion of ventilated and ventilation defect VOI. The results for each classification method are displayed in Table 3. Quadratic SVM performed best in both accuracy and area-under-curve, so it was applied to the test set of patients. Table 3 shows accuracy and AUC and Figure 3 shows the confusion matrix and receiver-operator-characteristic curve for the test subjects.

Table 2-3: Results for training and test set of patients. Only the best performing model was applied to the test set.

	Training (n=7)	**Test (n=3)**
Number sub-regions	20718	17358
# ventilation defect	10359	12783
# well ventilated	10359	4575
Logistic Regression accuracy	67.3	-
Logistic Regression AUC	0.74	-
Linear SVM accuracy	67.3	-
Linear SVM AUC	0.73	-
Quadratic SVM accuracy	70.9	66.2
Quadratic SVM AUC	0.78	0.72

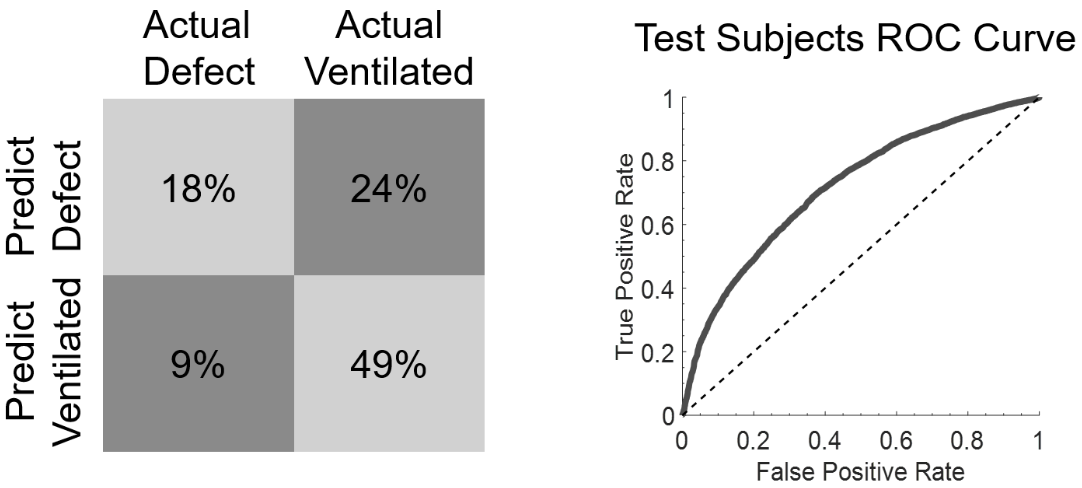

	Actual Defect	Actual Ventilated
Predict Defect	18%	24%
Predict Ventilated	9%	49%

Figure 2-3: Confusion matrix and receiver-operator-characteristics (ROC) curve for the test set of subjects.

The output of the model pipeline for a single test subject is shown in Figure 4 as a model score map and the binary map with spatial agreement between the model-predicted ventilation map and the ground truth ^{3}He ventilation map shown with yellow arrows.

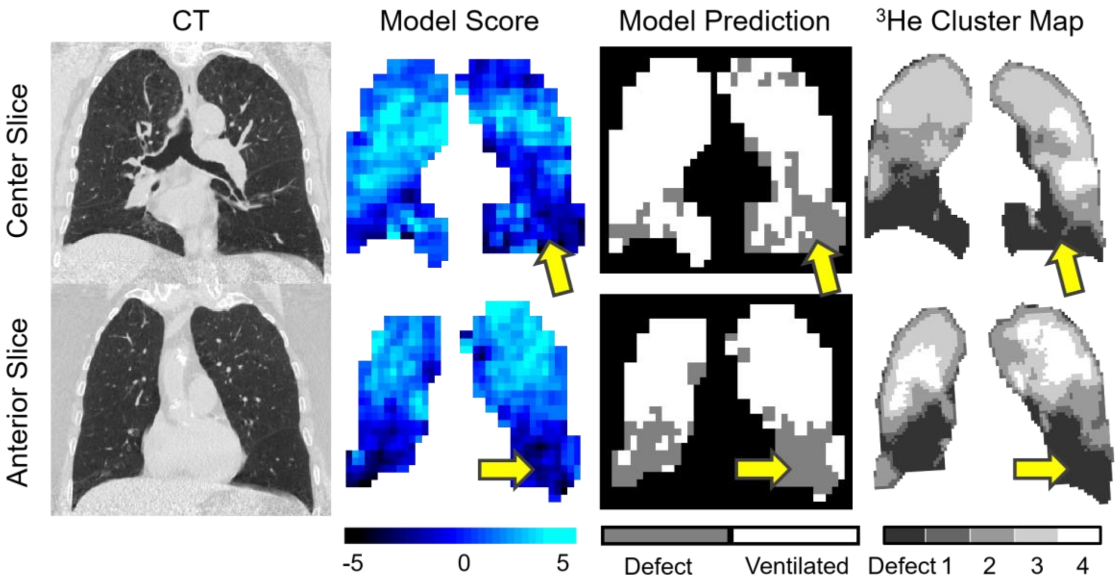

Figure 2-4: CT, Model predicted score, model binary prediction and ^{3}He cluster map for a test subject showing representative centre and anterior slices.

2.3.3 Comparison to Conventional CT Measures

Spatial correlation between ^{3}He ventilation defects and quantitative CT measures of emphysema were previously discovered and described using the TINCan cohort study.[16] To explore the predictive value of quantitative CT measures, and the additional value of texture features, we trained a logistic regression, linear SVM and quadratic SVM on the same patient dataset, using only RA_{950} and HU_{15}. The highest scoring model in the training set using only these two measurements and logistic regression resulted in 61% accuracy and an AUC of 0.66. This trained model was applied to the test set, with accuracy of 66% with an AUC of 0.63. Figure 5 shows the output of the logistic regression trained using only RA_{950} and HU_{15} next to the full model which showed qualitatively better prediction of ground truth.

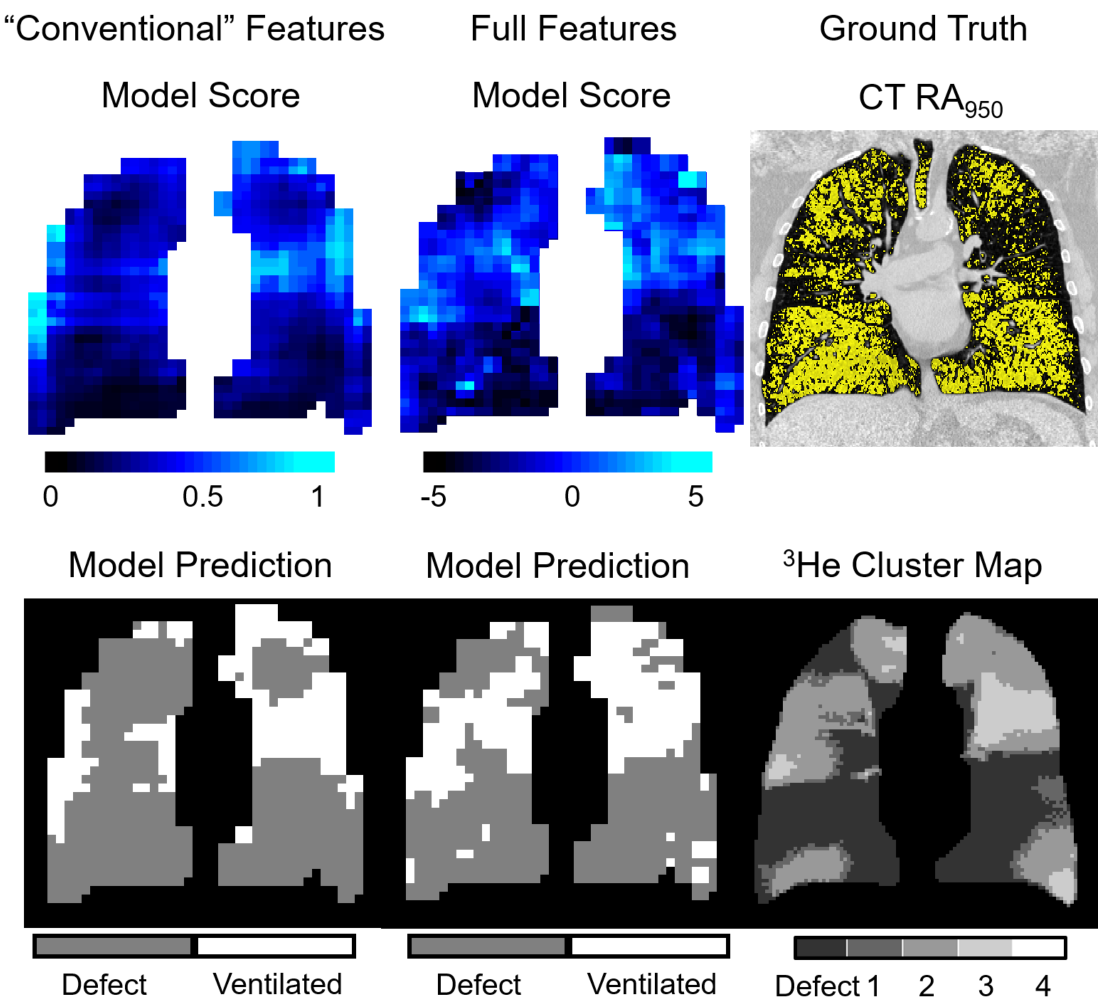

Figure 2-5: "Conventional" versus Full Feature Models
The output of the logistic regression trained using only RA_{950} and HU_{15} ("Conventional" Features), the output from the quadratic SVM model trained using the full set of features (Full Features), the CT showing region of low attenuation (RA_{950}), and the ground truth ^{3}He ventilation images.

2.4 New or Breakthrough Work to be Presented

We developed a pipeline to generate a new way to simulate ^{3}He MRI ventilation defect maps from a single-volume breath-hold CT and applied this in a proof-of-concept demonstration in a small cohort of patients with COPD. In a small training and test dataset of 10 COPD patients, this proposed approach yielded increased prediction success as compared to emphysema CT biomarkers alone. To our knowledge, this is the first demonstration of texture analysis and machine learning to predict ventilation abnormalities using single-volume thoracic CT.

2.5 Discussion and Conclusion

In this proof-of-concept demonstration, we developed a pipeline to co-register hyperpolarized gas MRI and thoracic CT and extract features from CT ROI to create a classification model and predict ventilated or non-ventilated. The prediction of lung ventilation functional information from thoracic CT was recently described using multi-volume CT and directly compared with hyperpolarized gas MRI.[17] Our approach is based on a single clinical CT in a small group of COPD patients and serves as validation for future developments. Future work will be done to extend this method to include a larger and more heterogeneous cohort of patients, which we hypothesize will increase both the performance and generalizability of the model.

2.6 References

1. Hoffman EA, Lynch DA, Barr RG, van Beek EJ, Parraga G, Investigators I. Pulmonary CT and MRI phenotypes that help explain chronic pulmonary obstruction disease pathophysiology and outcomes. J Magn Reson Imaging. 2016;43(3):544-57.

2. Parraga G, Ouriadov A, Evans A, et al. Hyperpolarized 3He ventilation defects and apparent diffusion coefficients in chronic obstructive pulmonary disease: preliminary results at 3.0 Tesla. Invest Radiol. 2007;42(6):384-91.

3. Kirby M, Svenningsen S, Owrangi A, et al. Hyperpolarized 3He and 129Xe MR imaging in healthy volunteers and patients with chronic obstructive pulmonary disease. Radiology. 2012;265(2):600-10.

4. Adams CJ, Capaldi DPI, Di Cesare R, McCormack DG, Parraga G, Canadian Respiratory Research N. On the Potential Role of MRI Biomarkers of COPD to Guide Bronchoscopic Lung Volume Reduction. Acad Radiol. 2018;25(2):159-68.

5. Kirby M, Heydarian M, Svenningsen S, et al. Hyperpolarized 3He magnetic resonance functional imaging semiautomated segmentation. Acad Radiol. 2012;19(2):141-52.

6. Regan EA, Hokanson JE, Murphy JR, et al. Genetic epidemiology of COPD (COPDGene) study design. COPD. 2010;7(1):32-43.

7. Vestbo J, Anderson W, Coxson HO, et al. Evaluation of COPD Longitudinally to Identify Predictive Surrogate End-points (ECLIPSE). Eur Respir J. 2008;31(4):869-73.

8. Couper D, LaVange LM, Han M, et al. Design of the Subpopulations and Intermediate Outcomes in COPD Study (SPIROMICS). Thorax. 2014;69(5):491-4.

9. Bourbeau J, Tan WC, Benedetti A, et al. Canadian Cohort Obstructive Lung Disease (CanCOLD): Fulfilling the need for longitudinal observational studies in COPD. COPD. 2014;11(2):125-32.

10. Gonzalez G, Ash SY, Vegas-Sanchez-Ferrero G, et al. Disease Staging and Prognosis in Smokers Using Deep Learning in Chest Computed Tomography. Am J Respir Crit Care Med. 2018;197(2):193-203.

11. Kirby M, Pike D, McCormack DG, Lam S, Coxson HO, Parraga G. Longitudinal Computed Tomography and Magnetic Resonance Imaging of COPD: Thoracic Imaging Network of Canada (TINCan) Study Objectives. Chronic Obstr Pulm Dis. 2014;1(2):200-11.

12. Kirby M, Eddy RL, Pike D, et al. MRI ventilation abnormalities predict quality-of-life and lung function changes in mild-to-moderate COPD: longitudinal TINCan study. Thorax. 2017;72(5):475-7.

13. Haralick RM, Shanmugam K, Dinstein Ih. Textural Features for Image Classification. IEEE Transactions on Systems, Man and Cybernetics. 1973;SMC-3(6):610-21.

14. Tang X. Texture information in run-length matrices. IEEE Trans Image Process. 1998;7(11):1602-9.

15. Mishima M, Hirai T, Itoh H, et al. Complexity of terminal airspace geometry assessed by lung computed tomography in normal subjects and patients with chronic obstructive pulmonary disease. Proc Natl Acad Sci U S A. 1999;96(16):8829-34.

16. Capaldi DP, Zha N, Guo F, et al. Pulmonary Imaging Biomarkers of Gas Trapping and Emphysema in COPD: (3)He MR Imaging and CT Parametric Response Maps. Radiology. 2016;279(2):597-608.

17. Tahir BA, Hughes PJC, Robinson SD, et al. Spatial Comparison of CT-Based Surrogates of Lung Ventilation With Hyperpolarized Helium-3 and Xenon-129 Gas MRI in Patients Undergoing Radiation Therapy. Int J Radiat Oncol Biol Phys. 2018;102(4):1276-86.

CHAPTER 3

3 CHRONIC OBSTRUCTIVE PULMONARY DISEASE: THORACIC CT TEXTURE ANALYSIS AND MACHINE LEARNING TO PREDICT PULMONARY VENTILATION

Building on Chapter 2 where the pipeline for texture analysis was developed, we apply it here in a relatively large cohort (n=95). Here we optimize the free parameters and build a texture model to predict ventilation based on widely available thoracic CT images.

The contents of this chapter were submitted to Radiology: A Westcott, D.P.I Capaldi, D.G McCormack, A Ward, A Fenster and G Parraga. Chronic Obstructive Pulmonary Disease: Thoracic CT Texture Analysis and Machine Learning to Predict Pulmonary Ventilation. Radiology (Submitted February 26, 2019).

3.1 Introduction

In patients with chronic obstructive pulmonary disease (COPD), structural remodeling of the airways, airway inflammation/obliteration and parenchyma destruction commonly result from chronic inhalation of combustibles including tobacco cigarettes and biomass fuels.[1] Pulmonary x-ray computed tomography (CT) is now widely used to visualize and quantify COPD lung structural abnormalities and these measurements have been exploited in large cohort studies including COPDGene,[2] ECLIPSE,[3] SPIROMICS,[4] and CANCold,[5] which have resulted in tens of thousands of thoracic CT images acquired in COPD patients.[6] While all of these studies have focused on anatomical measurements, complementary functional information may also be gleaned using inhaled xenon gas and dual-energy CT, or multi-volume CT acquisition through the breathing cycle in combination with advanced registration and analysis techniques.[7]

Hyperpolarized ^{3}He and ^{129}Xe magnetic resonance imaging (MRI) pulmonary measurements also provide high spatial and temporal resolution lung ventilation heterogeneity and microstructural information in COPD patients.[8, 9] Hyperpolarized gas MRI measurements in COPD patients are reproducible over short periods of time,[10] sensitive to therapy[11] and to the lung changes that accompany exacerbations.[12] In particular, ^{3}He and ^{129}Xe MRI ventilation heterogeneity, quantified as MRI ventilation defect percent (VDP),[13] is predictive of COPD exacerbations,[14] and longitudinal changes in quality of life and exercise capacity.[15] In spite of these unique advantages, hyperpolarized gas MRI has been limited to specialized research centres and has not been used in multi-centre cohort COPD studies and clinical trials, largely due to the high cost of the hyperpolarized gas and specialized equipment. Unfortunately, the unique functional information provided by hyperpolarized gas MRI has not been made as widely available as CT, for clinical evaluations of COPD patients. With the recent successful utilization of texture analysis and machine learning in medical imaging, we postulated it would be possible to identify the necessary and sufficient features in CT images to generate lung ventilation heterogeneity maps which would make this important lung functional information more widely available.

The TINCan cohort study[16] prospectively acquired volume-matched CT and MRI in a relatively large group of COPD patients and provides a unique opportunity to train and test a machine learning approach to generate pulmonary ventilation maps based on single-volume, non-contrast CT. We hypothesized that ventilation maps could be generated based on texture features and machine learning of CT images, and that such maps would significantly correlate spatially with hyperpolarized ^{3}He MRI ventilation defect percent (VDP) acquired experimentally in COPD patients. Such pulmonary ventilation predictions based on nearly universally available, conventional CT, may increase clinical access to valuable functional lung information beyond sites with hyperpolarized gas MRI. Therefore, the purpose of this study was to develop, train and test a pulmonary CT texture analysis and machine learning pipeline to predict ^{3}He MRI ventilation heterogeneity maps acquired in the same COPD patients.

3.2 Materials and Methods

3.2.1 Study Design and Pulmonary Tests

Participants provided informed written consent to a longitudinal cohort study,[17] approved by a local research ethics board in compliance with the Health Insurance Portability and Accountability Act (NCT=NCT02723474, Institutional Review Board #00000940).[16] Data were prospectively acquired from January 2010 to February 2017. Spirometry measurements were acquired according to the American Thoracic Society guidelines[18] using a whole-body system (MedGraphics Corporation, St Paul, MN). Body plethysmography was performed for the measurement of lung volumes and diffusing capacity of the lung for carbon monoxide (DL_{CO}) was measured using the attached gas analyzer. The St. George Respiratory Questionnaire (SGRQ)[19] was employed as a measure of quality of life.

Figure 3-1 shows the image processing pipeline we developed to generate ventilation maps based on thoracic CT, as well as the consort diagram. Participants were excluded if they did not have COPD, or if the CT acquisition parameters were prospectively altered to include a modified inspiration-expiration protocol/scheme. One patient dataset was used to perform texture parameter optimization and the remaining patient datasets were randomized to a training set, for tuning model hyperparameters, and a testing set.

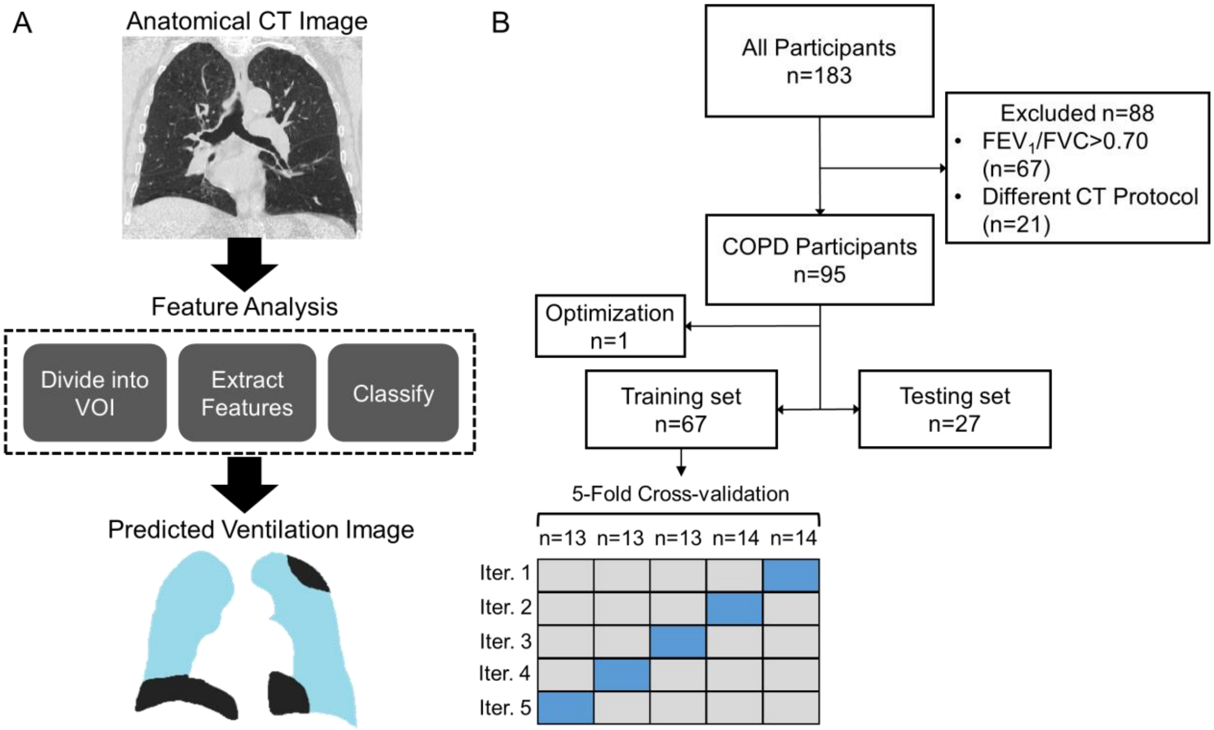

Figure 3-1: Schematic for Analysis.

A) Proposed texture analysis pipeline for generating predicted ventilation maps from thoracic CT. B) Consort diagram showing the participants that competed a visit, those excluded in this study due to not having COPD and those who had CT acquired with different voxel spacing. For the training set, participants were randomly divided into five groups. Training was performed during five iterations, where for each iteration the model was trained on four groups (gray rectangle), and validated on one group (blue rectangle).

3.2.2 Image Acquisition

Conventional proton (^{1}H) and ^{3}He MRI were performed on a whole-body 3T system (MR750 Discovery, General Electric Health Care [GEHC], Milwaukee, WI) with broadband imaging capabilities as previously described.[8] ^{1}H MRI was performed using a fast spoiled gradient-recalled-echo sequence, with acquisition parameters as previously described.[8] ^{3}He MRI employed a whole-body gradient set with maximum gradient amplitude of 50 mT/m and a single-channel, rigid elliptical transmit-receive chest coil (RAPID Biomedical GmbH, Wuerzburg, Germany). The basis frequency of the coil was 97.3 MHz and excitation power was 3 kW using an AMT 3T90 RF power amplifier (GEHC). ^{3}He gas was polarized to 30–40% polarization using a spin-exchange optical polarizer (Polarean Inc, Durham, NC). Thoracic CT was acquired on a 64-slice Lightspeed VCT scanner (GEHC, Milwaukee, WI) (64 × 0.625 mm, 120 kVp, 100 effective mA, tube rotation time = 500 ms, and pitch = 1.0). CT images were reconstructed using a slice thickness of 1.25 mm with a standard convolution kernel. The total effective dose to the participant was 1.8 mSv according to manufacturer settings and Imaging Performance Assessment of CT patient dosimetry calculator based on software from the Health Protection Agency of the United Kingdom (NRPB-SR250). The dimensions in the coronal plane for MRI were 3.1x3.1x15mm^3 and in the CT were 1.25x0.7x0.7mm^3.

3.2.3 Image co-Registration

Figure 3-2 shows the MRI-CT registration and volume-of-interest (VOI) extraction approach. MRI ^{1}H and ^{3}He images were registered using landmark registration, and k-means clustering was used to generate ventilation cluster maps, as previously described.[13] MRI data were resampled to 1.25x0.7mm voxels to match the original CT coronal plane dimensions and cropped to match the CT field-of-view. CT images were segmented using Pulmonary Workstation 2.0 (VIDA Diagnostics Inc., Coralville, IA), then were concatenated to 15mm thick slices in the coronal plane to match the MRI dimensions. The segmented ^{1}H MRI thoracic cavity masks were registered to the CT using a deformable registration, the modality independent neighborhood descriptor (MIND) registration.[20] The resultant registration transformation was applied to MRI ventilation cluster maps. Co-registration was evaluated using the Dice similarity coefficient (DSC).

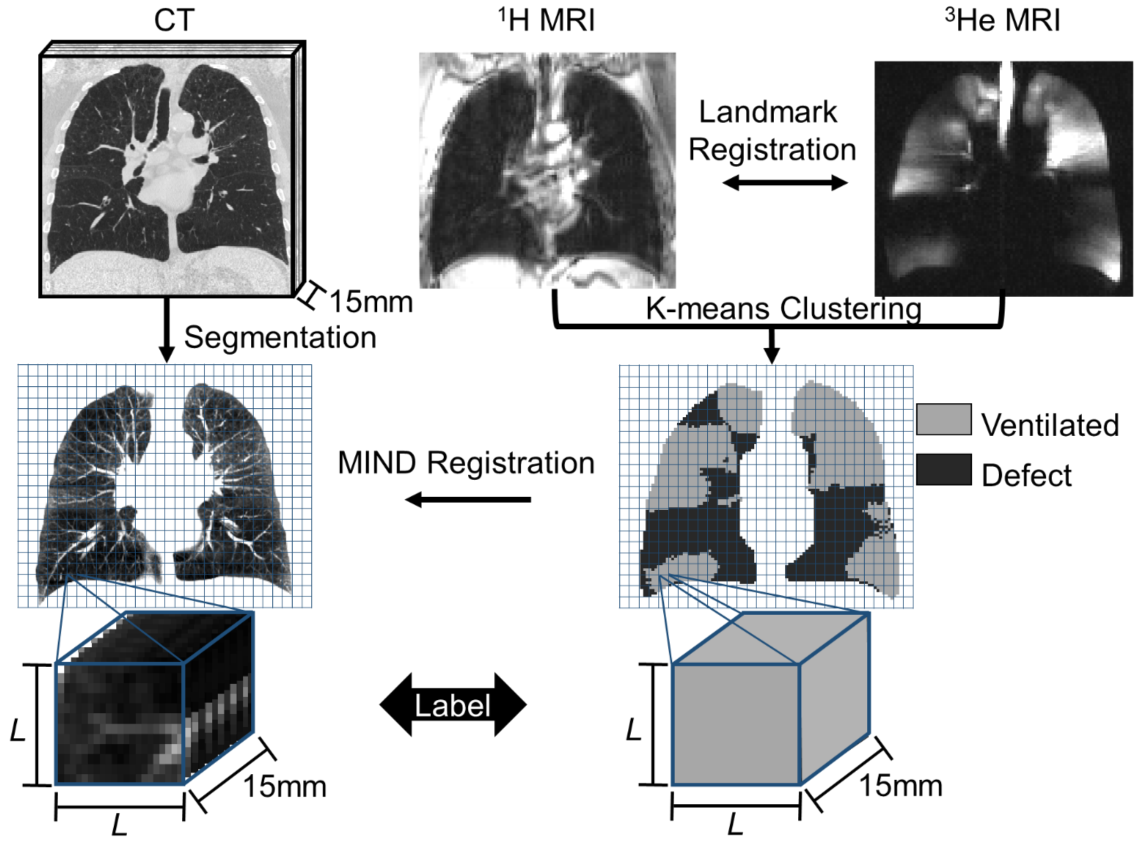

Figure 3-2: MRI to CT registration pipeline.
A 3-dimensional grid was used to define CT volume of interest (VOI) and the corresponding MRI based ventilation label where *L* is the length of the VOI in the coronal plane which is varied to determine the optimal VOI dimensions. MIND=modality independent neighborhood descriptor.

CT and MRI VOI were defined by applying a 3-dimensional grid, with dimensions of *L*x*L*x15mm^3, to the segmented CT and MRI ventilation map, where *L* was the VOI size in the coronal plane, which was optimized within the training set. The MRI ventilation map was labeled as background, ventilated and non-ventilated, with the label of each VOI being the mode, or most common, value. The grid was then shifted *L*/2mm horizontally and *L*/2mm vertically, to generate additional training samples, such that each voxel belonged to three separate VOIs. This technique was further utilized when predicting the final label in the test set, as the mean score of three overlapping *L*x*L*x15mm^3 VOIs was used, which then defined unique predictions for *L*/2x *L*/2x15mm^3 regions.

3.2.4 Thoracic CT Feature Extraction

First and second order features were extracted using a custom-built texture analysis software using MATLAB (MATLAB R2018a; MathWorks, Natick, Mass). A parameter search was performed to determine the texture parameters (GLCM bin width, CVM bin width and CVM bin range) using one patient dataset, which was then removed for the remainder of the analysis. The results from this parameter search is provided in Figure 3-3. Exemplar feature maps using these optimized parameters are shown in Figure 3-4. In total there were 87 unique features calculated per VOI, (i.e. global features). To provide the model more context in terms of COPD severity, each VOI feature was also divided by the average value of the feature within the same patient, and this generated an additional 87 features (i.e. ratio features), for a total of 174 features per VOI.

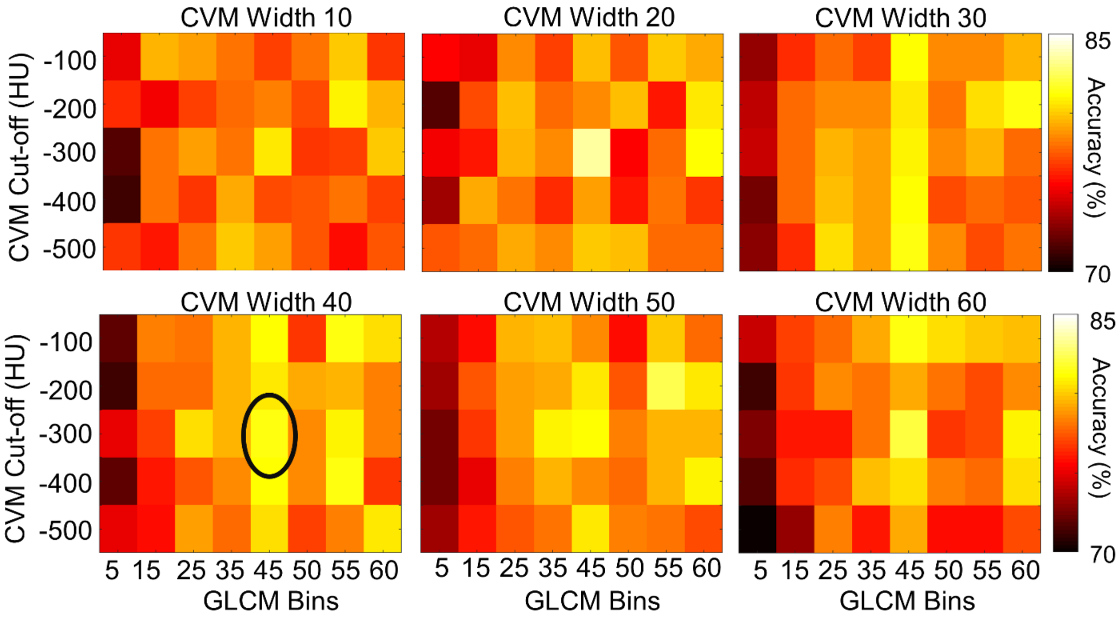

Figure 3-3: Texture parameter search.

Performed using single individual with VDP=25%. The set of parameters chosen were those which had the greatest validation accuracy with stable accuracy values surrounding it, as shown as CVM Width=40, CVM Cut-off=-300 HU, GLCM Bins=45.

First order features that were generated included mean CT density, standard deviation density, skewness, kurtosis, 2nd moment, 3rd moment, 95th percentile density, 15th percentile density (HU_{15}), relative area of the lung <-950 HU (RA_{950}), <-910 HU (RA_{910}) and <-856 HU (RA_{856}).

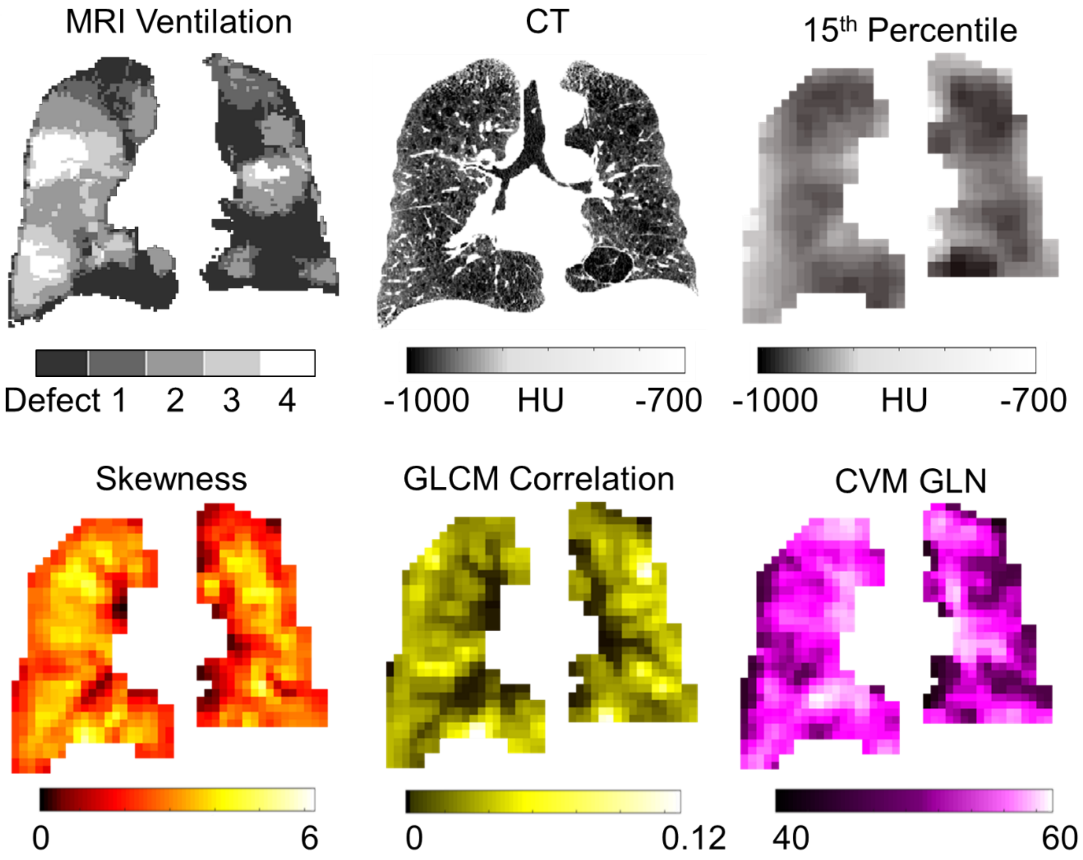

Figure 3-4: Hyperpolarized MRI ventilation, thoracic CT image and feature maps. Feature maps were calculated using VOI dimensions of 15x15x15mm^3. HU=Hounsfield Units; 15th percentile=the 15th percentile of CT density histogram; GLCM=gray level co-occurrence matrix; CVM=cluster volume matrix; GLN=gray level non-uniformity.

The gray level co-occurrence (GLCM) matrix[21] was populated by binning voxels based on Hounsfield Units (HU) into 45 bins from 0 to -1000 HU, where 45 bins was the result from the parameter search in the one patient removed. As previously described,[21] features were calculated as shown in the right side of Table 3-1 for the 13 unique 3-dimensional directions.

Table 3-1: Equations used to calculate features.
$p(i,j)$ is an element of the gray-level run length matrix, where i corresponds to the image intensity, and j corresponds to the number of homogenous runs of length j and n_r is the total number of runs. $g(i,j)$ is an element of the co-occurrence matrix. $\mu = \sum_{i,j} i * g(i,j)$ is the mean, $\sigma = \sum_{i,j} g(i,j) * (i-\mu)^2$ is the variance.

CVM Feature	Equation	GLCM Feature	Equation
Short Run Emphasis (SRE)	$\frac{1}{n_r}\sum_{i,j}\frac{p(i,j)}{j^2}$	Energy	$\sum_{i,j} g(i,j)^2$
Long Run Emphasis (LRE)	$\frac{1}{n_r}\sum_{i,j} p(i,j) * j^2$	Entropy	$\sum_{i,j} -\log(g(i,j)) * g(i,j))$, if $g(i,j) \cong 0$ 0 if $g(i,j) = 0$
Gray-level Non-uniformity (GLN)	$\frac{1}{n_r}\sum_{i}\left(\sum_{j} p(i,j)\right)^2$	Contrast	$\sum_{i,j} g(i,j) * (i-j)^2$
Run length Non-uniformity (RLN)	$\frac{1}{n_r}\sum_{j}\left(\sum_{i} p(i,j)\right)^2$	Homogeneity	$\sum_{i,j}\frac{g(i,j)}{1+(i-j)^2}$
Run Percentage (RP)	$\frac{n_r}{\sum_{i,j} j * p(i,j)}$	Correlation	$\sum_{i,j}\frac{g(i,j) * (i-\mu) * (j-\mu)}{\sigma^2}$
Low gray-level run emphasis (LGRE)	$\frac{1}{n_r}\sum_{i,j}\frac{p(i,j)}{i^2}$		
High gray-level run emphasis (HGRE)	$\frac{1}{n_r}\sum_{i,j} p(i,j) * i^2$		
Short run low gray-level emphasis (SRLGE)	$\frac{1}{n_r}\sum_{i,j}\frac{p(i,j)}{i^2 * j^2}$		
Short run high gray-level emphasis (SRHGE)	$\frac{1}{n_r}\sum_{i,j} p(i,j) * \frac{i^2}{j^2}$		
Long run low gray-level emphasis (LRLGE)	$\frac{1}{n_r}\sum_{i,j} p(i,j) * \frac{j^2}{i^2}$		
Long run high-gray level emphasis (LRHGE)	$\frac{1}{n_r}\sum_{i,j} p(i,j) * j^2 * i^2$		

Although run-length matrix is commonly used as a method to extract features from 2-dimensional images,[22] this becomes computationally intensive, and does not account for regions that are fully, but not linearly, connected which can be accounted for using low attenuating clusters.[23] Therefore, here we employed a combination of the run-length matrix with CT cluster analysis by creating a new texture parameter, the cluster volume matrix (CVM). This is a 3-dimensional analog of the run length matrix, where $\mathrm{p(i,j)}$ is the number of clusters, i is the gray level, and j is the 3-dimensional cluster size of the same gray level. The features calculated from the CVM are the same as those calculated from a run-length matrix, as shown on the left side of Table 3-1. The matrix was populated by binning voxels into 18 bins between -300 and -1000 HU, where all voxels with values greater than -300 were collapsed into a single bin and all voxels less than -1000HU were included in the lowest density bin.

3.2.5 Feature Selection

With the intention to avoid model overfitting and maximize model generalizability, a forward feature selection scheme was developed in MATLAB. As shown in Figure 1B, training data were divided into five different groups, and five-fold cross validation was performed using logistic regression, where features were iteratively added based on the feature that lead to the greatest improvement of the validation area-under-the-curve (AUC), calculated from the receiver operator characteristic (ROC) curve. As shown in Figure 3-5, this was performed up to 20 features, as the AUC plateaued to a maximum when 20 features were used. Features which were in the first 20 features selected for at least two of the five-fold cross-validation steps were included in the final model to ensure the features consistently contribute to an optimal model.

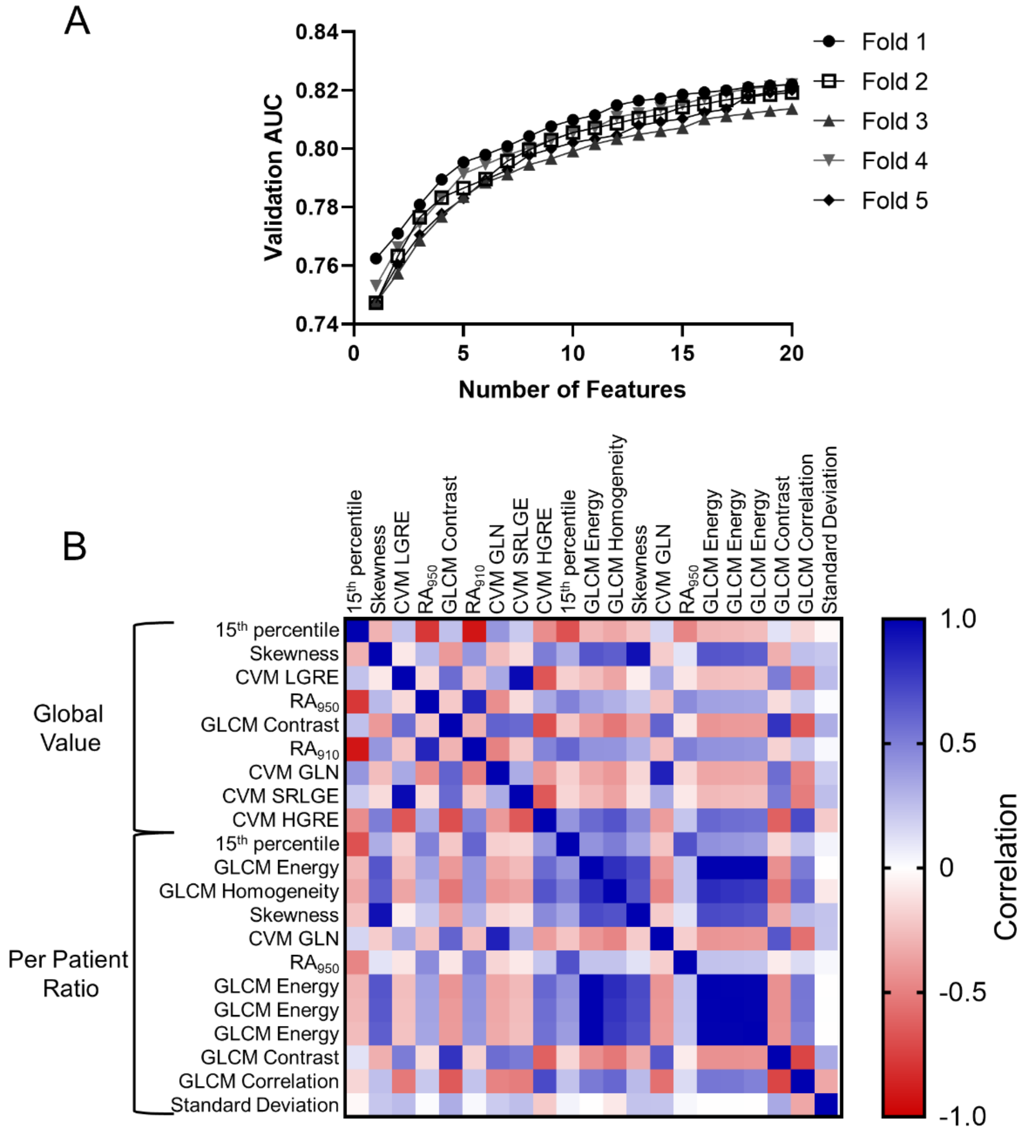

Figure 3-5: Details of Training set Outputs.

A) Number of features and validation AUC where features were iteratively included based on maximal increase to the model during forward feature selection B) Correlation plot for features included in the final model.

15th percentile=15th percentile of CT Hounsfield Units (HU); CVM = cluster volume matrix; LGRE=low gray-level run emphasis; RA_{950}=relative area of CT histogram <-950 HU; GLCM=gray level co-occurrence matrix; GLN=gray level non-uniformity; SRLGE=short run low gray-level emphasis; HGRE=high gray-level run emphasis

3.2.6 Training the Classification Model

To simplify the anatomical heterogeneity included in the model while maintaining the information that is representive of the entire lung, we included the centre-most six slices (of ~15 total slices) that encompass 58±5 percent volume of the lung. In the training set, the VOI size and sampling scheme were optimized to maximize AUC. The VOI dimensions were 15 mm in the posterior to anterior direction and were varied from $15x15mm^2$ to $30x30mm^2$ in the coronal plane. Due to a greater number of ventilated versus non-ventilated VOI, the method for sampling VOI to create the training set was critical. Under-sampling the majority class (ventilated volumes) was used in the training set with varying methods to ensure that patients with a lower magnitude of ventilation defect percent were adequately represented in the training data set. To accomplish this, at least as many ventilated as non-ventilated volumes were randomly sampled from each participant. Within the training set, to include a balance of patients with large ventilation defects, and patients with a lower magnitude of ventilation defect percent, a threshold was varied to define the minimum percentage of the lung sampled (i.e. for threshold=20%, participants with VDP<20%, ventilated volume sampled=20% of the lung).

Once all parameters and features were selected, 5-fold cross-validation training was performed using a logistic regression, linear support vector machine (SVM) and a quadratic SVM. These classifiers were tested as they had greater performance compared to random forest, linear discriminant and nearest neighbor methods on previous experiments. The data were standardized and hyperparameter optimization was performed using Matlab (Classification Learner app) for each model to find the optimal hyperparameters, as displayed in Table 3-2. The mean cross-validation AUC were used to compare models.

Table 3-2: Quadratic SVM Training Hyperparameters.
The results of hyperparameter optimization for quadratic support vector machine using the Sequential Minimal Optimization solver, trained using 5-fold cross-validation and selecting the model with the highest mean validation accuracy.

Metric	Value
Bias	1.2001
Box Constraint	1.0
Kernel Scale	1.8248

3.2.7 Statistics

All statistical analyses were performed using GraphPad Prism, V8.0 (GraphPad Software Inc., La Jolla, CA). To determine group differences, unpaired parametric t-tests were used when the data were normally distributed, and non-parametric Mann-Whitney tests were used when the data were not normally distributed as tested using the Shapiro-Wilk test for normality. Pearson correlation coefficients were used to determine the relationships between model, MRI and pulmonary function measurements. Results were considered significant when the probability of a two-tailed type I error (alpha) was less than 5% ($p<0.05$).

3.3 Results

Demographic, pulmonary function tests and imaging measurements provided in Table 3-3 show there were no significant differences between training and testing data sets.

Table 3-3: Participant demographics, pulmonary function and imaging measurements.

Parameter (±SD)	**All Participants n=94**	**Training n=67**	**Test n=27**	**Difference *p*-value**
Age years	70 (9)	70 (8)	69 (10)	0.6
Female sex %	33	31	48	0.1
Pack Years years	50 (30)	49 (29)	50 (27)	0.9
FEV_1 $\%_{pred}$	63 (25)	63 (25)	61 (24)	0.6
FEV_1/FVC %	51 (13)	51 (13)	51 (13)	1
DL_{CO} $\%_{pred}$	56 (23)	54 (21)^	57 (22)	0.7
SGRQ	40 (18)	41 (18)†	37 (20)‡	0.5
RA_{950} %	10 (10)	10 (10)	10 (10)	1
VDP %	12 (12)	12 (11)	11 (12)	0.9
DSC %	95 (1)	95 (1)	95 (1)	0.8

FEV_1=forced expiratory volume in 1 second; FEV_1/FVC=FEV_1 ratio with forced vital capacity; $\%_{pred}$=percent predicted; DL_{CO}=diffusing capacity for carbon monoxide; RA_{950}=relative area of CT histogram <-950 HU; VDP=ventilation defect percent; DSC=dice similarity coefficient for CT-MRI co-registration.
†n=64; ‡n=26; ^n=66

As shown in Table 3-4, the best performing VOI size was 30x30mm^2 while the optimal sampling threshold required a minimum of 30% ventilated lung, based on the highest AUC while maintaining the sensitivity once the AUC plateaued. Table 3-4 also shows that by varying the sampling pattern there was a trade-off between sensitivity and specificity.

Therefore, feature selection was performed using 5-fold cross-validation with VOI dimensions of $30x30x15mm^3$ and a sampling minimum of 30%.

Table 3-4: Volume of interest and training sample patterns.
To optimize coronal VOI dimensions, the sampling scheme ensured ≥ 30% ventilated lung was evaluated. To optimize the sampling scheme, for each participant evaluated in the training set, at least as many ventilated samples as non-ventilated samples were evaluated. To ensure that disease severity (ventilation, ventilation defects) was represented to train the model, a minimum percent of the ventilated lung was sampled.

VOI dimensions	Validation Accuracy	Validation AUC	Validation Sensitivity	Validation Specificity
		Coronal VOI Size		
$15x15mm^2$	81.5	0.773	0.440	0.885
$20x20mm^2$	78.6	0.784	0.584	0.822
$25x25mm^2$	80.1	0.804	0.605	0.833
$30x30mm^2$	85.0	0.820	0.485	0.906
Sampling Scheme	**Minimum % Lung Sampled**			
0	69.4	0.776	0.729	0.688
10	78.7	0.808	0.661	0.807
20	82.6	0.816	0.576	0.864
30	85.0	0.820	0.485	0.906
40	86.3	0.820	0.382	0.937

Table 3-5 shows that first-order density-based features have the largest individual AUC and both global and ratio values helped optimize the model, where a total of 21 features were included in the final model. The correlation plot for all included features (Figure S2B) shows the strong correlation between GLCM features in different directions. During training, logistic regression, linear SVM and quadratic SVM achieved validation accuracy/AUC of 85.2%/0.82, 86.3%/0.81 and 87.0%/0.86, respectively. Therefore, the quadratic SVM model was applied to the test set.

Table 3-5: Features utilized and AUC for training group.
(participants n=67, VOI n=48,313)

Feature	AUC
15th percentile global	0.765
Skewness global	0.505
15th percentile ratio	0.713
GLCM Energy [-1,1,1] ratio	0.585
GLCM Homogeneity [0,1,0] ratio	0.570
Skewness ratio	0.507
CVM GLN ratio	0.620
RA_{950} ratio	0.711
CVM LGRE global	0.550

RA_{950} global	0.761
GLCM Energy [1,1,-1] ratio	0.586
GLCM Energy [1,0,0] global	0.584
GLCM Contrast [1,0,1] global	0.588
RA_{910} global	0.753
CVM GLN global	0.660
GLCM Energy [1,1,0] ratio	0.583
GLCM Contrast [1,0,-1] ratio	0.594
CVM SRLGE global	0.552
CVM HGRE global	0.570
GLCM Correlation [1,0,-1] ratio	0.594
Standard deviation ratio	0.535

Global=value; ratio=value of VOI feature divided by mean feature value for whole lung; 15th percentile=15th percentile of CT Hounsfield Units (HU); CVM = cluster volume matrix; LGRE=low gray-level run emphasis; RA_{950}=relative area of CT histogram <-950 HU; GLCM=gray level co-occurrence matrix; GLN=gray level non-uniformity; SRLGE=short run low gray-level emphasis; HGRE=high gray-level run emphasis.

Figure 3-6 shows the predicted ventilation maps for four subjects within the test set, along with the experimentally-acquired CT and MRI ventilation scans. A qualitative spatial agreement between the model ventilation prediction and the MRI ventilation is observed, as well as noting the magnitude of predicted ventilation defects corresponds to that observed in the MRI ventilation.

Figure 3-6: Representative CT, MRI and model outputs for four participants in testing set. S1: FEV_1=116%$_{pred}$, FEV_1/FVC=67%, DL_{CO}=107%$_{pred}$; S2: FEV_1=39%$_{pred}$, FEV_1/FVC=34%, DL_{CO} =63%$_{pred}$; S3: FEV_1 =25%$_{pred}$, FEV_1/FVC=29%, DL_{CO} =17%$_{pred}$; S4: FEV_1=30%$_{pred}$, FEV_1/FVC=30%, DL_{CO} =39%$_{pred}$.

In Figure 3-7, test-set evaluations are shown where the final model achieved an accuracy of 87.9% and an AUC of 0.82. Figure 3-7 also shows the significant and strong relationship between model-predicted VDP and hyperpolarized MRI VDP (r=0.90, p=<0.0001) as well as their significant relationships with FEV_1 (Model r=-0.65, p<0.001; MRI r=-0.70, p<0.0001) FEV_1/FVC (Model r=-0.73, p<0.0001; MRI r=-0.75, p<0.0001), DL_{CO} (Model r=-0.69, p<0.0001; MRI r=-0.65, p<0.001) and SGRQ (Model r=0.59, p<0.005; MRI r=0.65, p<0.001).

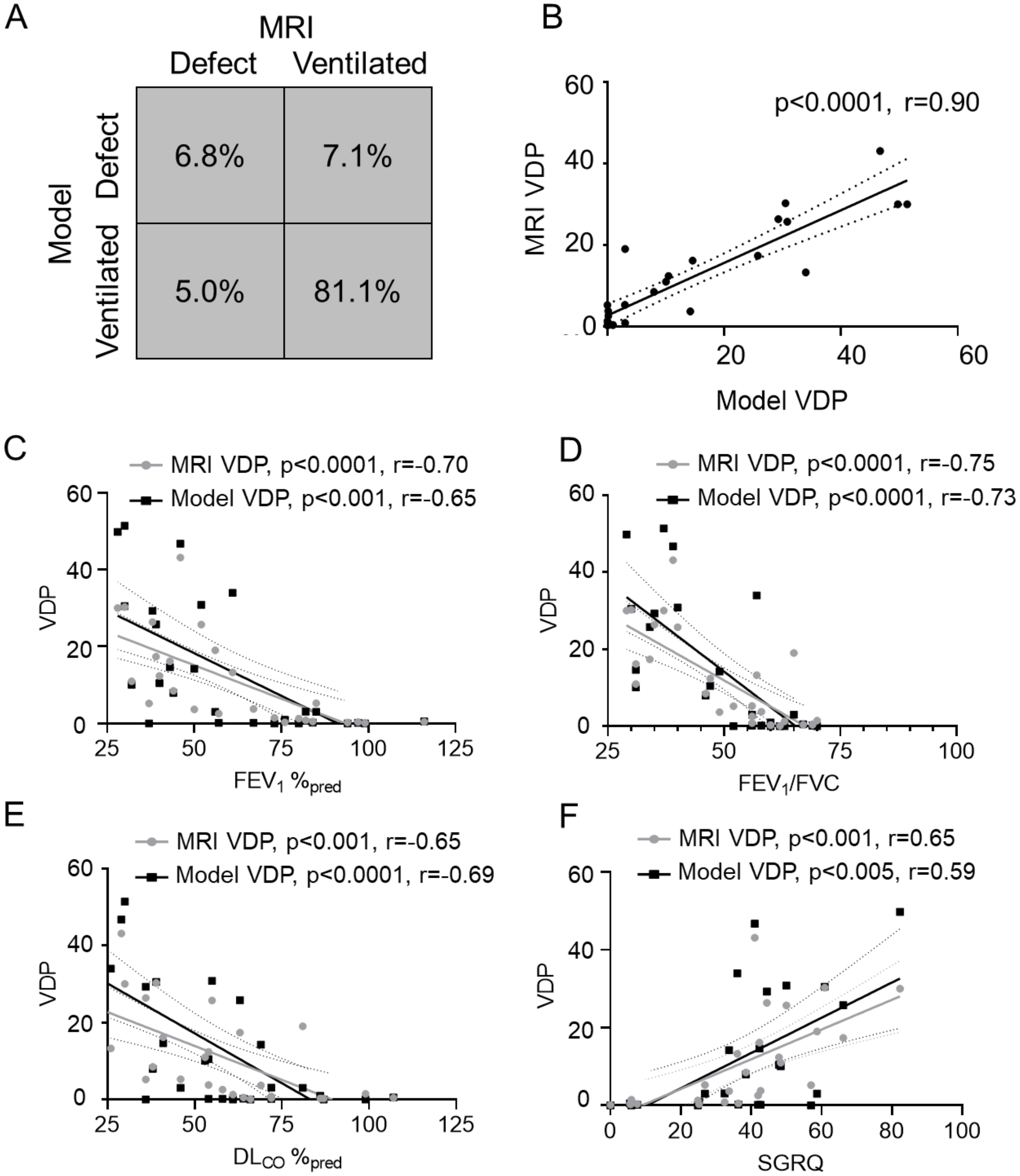

Figure 3-7: Testing Set Model Outputs and Relationships.

A) Confusion matrix showing the model predicted, and the ground truth MRI classification, where accuracy=87.9%, AUC=0.82, sensitivity=0.58, specificity=0.92 (VOI n = 32457); B) Predicted VDP versus the observed VDP (r=0.90, p<0.0001, $y = 0.65x + 3$). C-F) clinical measures versus model VDP and MRI VDP. DL_{CO}= Diffusing capacity of the lung for carbon monoxide; VDP= ventilation defect percent; FEV_1=forced expiratory volume in one second; FVC=functional vital capacity; SGRQ=St. George Respiratory Questionnaire.

3.4 Discussion

We developed a CT analysis pipeline that combined texture feature analysis with machine learning to generate pulmonary ventilation heterogeneity maps for direct comparison with MRI ventilation maps acquired in patients. The pipeline was trained and tested in a cohort of 95 COPD patients in whom volume-matched MRI and CT were acquired within 10 minutes of each other. We made the following observations: 1) the highest performing model on the training set was applied to the testing set where it classified ventilated and non-ventilated VOI with 88% accuracy and an AUC of 0.82, 2) there were significant and strong correlations between model-predicted VDP and MRI VDP, and, 3) both model-predicted and MRI VDP were significantly related to clinically-relevant measurements in the same patients including SGRQ, DL_{CO} and FEV_1/FVC.

The pipeline we created generated a model that classified ventilated and non-ventilated volumes with 88% accuracy and an AUC of 0.82. It is important to note that we chose the parameters and final model based on maximizing the AUC, such that both sensitivity and specificity of detecting ventilation heterogeneities were considered for algorithm performance. Density-based first order features generated the largest AUC, which was consistent with the spatial overlap between emphysema and ventilation defects, and in agreement with previous experimental results.[14, 24] The influence of both global and ratio features for predicting ventilation underscores the importance of considering disease severity in relation to the rest of an individual's lung, and relative to all patient lungs.

Model VDP was strongly and significantly related to MRI VDP. The strong relationship between model and MRI VDP also provides strong support for the notion that the model well-predicted a large range of disease severity present within this study. Model-predicted VDP and MRI VDP were also significantly related to clinically-relevant pulmonary function measurements, including FEV_1/FVC and DL_{CO} as well as SGRQ. This is an important result in the context of previous automated disease quantification methods developed using texture analysis,[25-29] which were trained using unsupervised learning, or with previously developed disease classification systems. In contrast, the predicted-model trained here provided a quantitative measure that was spatially-dependent and trained using ventilation as the ground truth.

We acknowledge numerous study limitations including the fact that TINCan comprised a convenience sample with a large number of moderate to severe patients, so generalizability should be considered in this context. We also acknowledge that only the centre ~60% of the lung was included in the analysis in order to simplify CT-MRI co-registration. Nevertheless, the centre six slices provide an appropriate representation of all five lung lobes, with a mean VDP difference of 1±2% between the slices we used and whole lung measurements. CT protocol and scanner image reconstruction may influence texture features,[30, 31] and as such, the generalizability of the trained model presented here to other scanners and CT acquisition protocols needs to be considered. With that in mind, it is expected that the inclusion of the normalized features (to whole lung means) may help mitigate inter-scanner and inter-site variability. While application of our approach to a multi-centre dataset will evaluate its utility, it is worth noting that many of the density-based measures such as RA_{950} and HU_{15} are already successfully used in clinic as well as in multi-site studies.[32, 33]

In 95 patients with COPD, machine learning and texture analysis were used to generate predicted pulmonary ventilation heterogeneity maps from anatomical thoracic CT and these maps significantly and strongly correlated with MRI ventilation, pulmonary function measurements and quality of life. This technology, when externally validated, will enable widespread generation of ventilation heterogeneity maps using nearly-ubiquitous CT scanners, providing a novel way to generate ventilation maps beyond the few centres with hyperpolarized MRI.

3.5 References

1. Vogelmeier CF, Criner GJ, Martinez FJ, et al. Global Strategy for the Diagnosis, Management, and Prevention of Chronic Obstructive Lung Disease 2017 Report. GOLD Executive Summary. Am J Respir Crit Care Med. 2017;195(5):557-82.

2. Regan EA, Hokanson JE, Murphy JR, et al. Genetic epidemiology of COPD (COPDGene) study design. COPD. 2010;7(1):32-43.

3. Vestbo J, Anderson W, Coxson HO, et al. Evaluation of COPD Longitudinally to Identify Predictive Surrogate End-points (ECLIPSE). Eur Respir J. 2008;31(4):869-73.

4. Couper D, LaVange LM, Han M, et al. Design of the Subpopulations and Intermediate Outcomes in COPD Study (SPIROMICS). Thorax. 2014;69(5):491-4.

5. Bourbeau J, Tan WC, Benedetti A, et al. Canadian Cohort Obstructive Lung Disease (CanCOLD): Fulfilling the need for longitudinal observational studies in COPD. COPD. 2014;11(2):125-32.

6. Gonzalez G, Ash SY, Vegas-Sanchez-Ferrero G, et al. Disease Staging and Prognosis in Smokers Using Deep Learning in Chest Computed Tomography. Am J Respir Crit Care Med. 2018;197(2):193-203.

7. Hoffman EA, Lynch DA, Barr RG, van Beek EJ, Parraga G, Investigators I. Pulmonary CT and MRI phenotypes that help explain chronic pulmonary obstruction disease pathophysiology and outcomes. J Magn Reson Imaging. 2016;43(3):544-57.

8. Parraga G, Ouriadov A, Evans A, et al. Hyperpolarized 3He ventilation defects and apparent diffusion coefficients in chronic obstructive pulmonary disease: preliminary results at 3.0 Tesla. Invest Radiol. 2007;42(6):384-91.

9. Kirby M, Svenningsen S, Kanhere N, et al. Pulmonary ventilation visualized using hyperpolarized helium-3 and xenon-129 magnetic resonance imaging: differences in COPD and relationship to emphysema. J Appl Physiol (1985). 2013;114(6):707-15.

10. Parraga G, Mathew L, Etemad-Rezai R, McCormack DG, Santyr GE. Hyperpolarized 3He magnetic resonance imaging of ventilation defects in healthy elderly volunteers: initial findings at 3.0 Tesla. Acad Radiol. 2008;15(6):776-85.

11. Kirby M, Mathew L, Heydarian M, Etemad-Rezai R, McCormack DG, Parraga G. Chronic obstructive pulmonary disease: quantification of bronchodilator effects by using hyperpolarized (3)He MR imaging. Radiology. 2011;261(1):283-92.

12. Kirby M, Kanhere N, Etemad-Rezai R, McCormack DG, Parraga G. Hyperpolarized helium-3 magnetic resonance imaging of chronic obstructive pulmonary disease exacerbation. J Magn Reson Imaging. 2013;37(5):1223-7.

13. Kirby M, Heydarian M, Svenningsen S, et al. Hyperpolarized 3He magnetic resonance functional imaging semiautomated segmentation. Acad Radiol. 2012;19(2):141-52.

14. Kirby M, Pike D, Coxson HO, McCormack DG, Parraga G. Hyperpolarized (3)He ventilation defects used to predict pulmonary exacerbations in mild to moderate chronic obstructive pulmonary disease. Radiology. 2014;273(3):887-96.

15. Kirby M, Mathew L, Wheatley A, Santyr GE, McCormack DG, Parraga G. Chronic obstructive pulmonary disease: longitudinal hyperpolarized (3)He MR imaging. Radiology. 2010;256(1):280-9.

16. Kirby M, Pike D, McCormack DG, Lam S, Coxson HO, Parraga G. Longitudinal Computed Tomography and Magnetic Resonance Imaging of COPD: Thoracic Imaging Network of Canada (TINCan) Study Objectives. Chronic Obstr Pulm Dis. 2014;1(2):200-11.

17. Kirby M, Eddy RL, Pike D, et al. MRI ventilation abnormalities predict quality-of-life and lung function changes in mild-to-moderate COPD: longitudinal TINCan study. Thorax. 2017;72(5):475-7.

18. Miller MR, Hankinson J, Brusasco V, et al. Standardisation of spirometry. Eur Respir J. 2005;26(2):319-38.

19. Jones PW, Quirk FH, Baveystock CM, Littlejohns P. A self-complete measure of health status for chronic airflow limitation. The St. George's Respiratory Questionnaire. Am Rev Respir Dis. 1992;145(6):1321-7.

20. Heinrich MP, Jenkinson M, Bhushan M, et al. MIND: modality independent neighbourhood descriptor for multi-modal deformable registration. Med Image Anal. 2012;16(7):1423-35.

21. Haralick RM, Shanmugam K, Dinstein Ih. Textural Features for Image Classification. IEEE Transactions on Systems, Man and Cybernetics. 1973;SMC-3(6):610-21.

22. Tang X. Texture information in run-length matrices. IEEE Trans Image Process. 1998;7(11):1602-9.

23. Mishima M, Hirai T, Itoh H, et al. Complexity of terminal airspace geometry assessed by lung computed tomography in normal subjects and patients with chronic obstructive pulmonary disease. Proc Natl Acad Sci U S A. 1999;96(16):8829-34.

24. Capaldi DP, Zha N, Guo F, et al. Pulmonary Imaging Biomarkers of Gas Trapping and Emphysema in COPD: (3)He MR Imaging and CT Parametric Response Maps. Radiology. 2016;279(2):597-608.

25. Park YS, Seo JB, Kim N, et al. Texture-based quantification of pulmonary emphysema on high-resolution computed tomography: comparison with density-based quantification and correlation with pulmonary function test. Invest Radiol. 2008;43(6):395-402.

26. Xu Y, Sonka M, McLennan G, Guo J, Hoffman EA. MDCT-based 3-D texture classification of emphysema and early smoking related lung pathologies. IEEE Trans Med Imaging. 2006;25(4):464-75.

27. Ginsburg SB, Lynch DA, Bowler RP, Schroeder JD. Automated texture-based quantification of centrilobular nodularity and centrilobular emphysema in chest CT images. Acad Radiol. 2012;19(10):1241-51.

28. Yang J, Angelini ED, Balte PP, et al. Unsupervised Discovery of Spatially-Informed Lung Texture Patterns for Pulmonary Emphysema: The MESA COPD Study. Med Image Comput Comput Assist Interv. 2017;10433:116-24.

29. Chabat F, Yang GZ, Hansell DM. Obstructive lung diseases: texture classification for differentiation at CT. Radiology. 2003;228(3):871-7.

30. Shafiq-Ul-Hassan M, Zhang GG, Latifi K, et al. Intrinsic dependencies of CT radiomic features on voxel size and number of gray levels. Med Phys. 2017;44(3):1050-62.

31. Yasaka K, Akai H, Mackin D, et al. Precision of quantitative computed tomography texture analysis using image filtering: A phantom study for scanner variability. Medicine (Baltimore). 2017;96(21):e6993.

32. Schroeder JD, McKenzie AS, Zach JA, et al. Relationships between airflow obstruction and quantitative CT measurements of emphysema, air trapping, and airways in subjects with and without chronic obstructive pulmonary disease. AJR Am J Roentgenol. 2013;201(3):W460-70.

33. Coxson HO, Dirksen A, Edwards LD, et al. The presence and progression of emphysema in COPD as determined by CT scanning and biomarker expression: a prospective analysis from the ECLIPSE study. Lancet Respir Med. 2013;1(2):129-36.

CHAPTER 4

4 CONCLUSIONS AND FUTURE DIRECTIONS

In this final chapter, a summary and overview is provided for the main observations and conclusions presented in Chapter 2 and Chapter 3. Limitations related to specific studies, as well as general limitations are provided, along with potential mitigation strategies for the limitations. Finally, the chapter concludes by discussing future directions for the methods developed and discussed here.

4.1 Overview and Research Objectives

Pulmonary imaging has been used to provide novel insights into COPD, specifically utilizing hyperpolarized gas MRI for ventilation imaging, which unfortunately, has been limited in application to date due to the large associated cost. Texture analysis is an increasingly popular technique for classifying lung disease severity and detecting cancer in thoracic CT. The overarching objective of this thesis was to develop and apply a texture analysis pipeline to predict pulmonary ventilation from thoracic CT, thereby extending the availability of specialized pulmonary ventilation imaging. We postulated the structural information contained within a single-volume breath hold CT could inform on regional lung ventilation. The specific research objectives were to first develop a pipeline to perform texture analysis to predict pulmonary ventilation from thoracic CT, and second, apply this pipeline in a cohort of COPD patients to generate predicted ventilation maps.

4.2 Summary and Conclusions

In Chapter 2, we first proposed the method of using texture analysis to predict pulmonary ventilation. Here, the pipeline was developed using a small cohort of COPD patients as a proof-of-concept demonstration. In this small cohort, we observed that utilizing a volume by volume prediction provided a large number of training samples, which were used to train a classifier. The observations in this proof-of-concept study demonstrated the potential of this approach to be applied in a large cohort.

In Chapter 3, we applied, and improved, upon the methods developed in Chapter 2. An important addition to these methods was the normalization of extracted features to patient whole lung values. This allows the model to account for the context of patient disease severity, as well as the regional disease severity within a patient. 95 patients were randomized to optimization (n=1), training (n=67) and testing (n=27) datasets. Texture analysis and machine learning were used to create model-predicted ventilation maps from CT, which strongly correlated with MRI ventilation maps, DL_{CO} and quality of life measurements in COPD. These results indicate the potential for the approach presented in this thesis to be applied in predicting pulmonary ventilation, using widely available CT protocols.

4.3 Limitations

Chapter 2 is a proof-of-concept demonstration of the method developed, and the results must therefore be taken in that context. The patients within this cohort were hand selected based on the presence of severe emphysema as determined using CT emphysema measures, and the presence of a large magnitude of ventilation defects. This was done to enforce a near equal balance of ventilated and not ventilated samples for training, however, this strategy also introduced a large bias into the generalizability of the results reported. Despite choosing patients with similar emphysema and ventilation defect characteristics, there may be large physiological differences between the training and testing datasets due to a small sample size. It is therefore difficult to ascertain whether the drop-in performance observed from training to testing was due to suboptimal selection of parameters (possibly overfitting), or due to testing on patients that had substantially different disease manifestation. To address these limitations, a larger, more heterogeneous cohort of patients should be explored, which allows for a more thorough investigation into the optimal model parameters.

Chapter 3 addressed many of the major limitations of the study presented in Chapter 2, including utilizing a larger cohort of COPD patients, however, there were still a number of limitations. Firstly, the patient data used in the analysis were from the TINCan cohort, which is comprised of a large number of moderate to severe patients compared to the general COPD population, and so the generalizability must be considered in this context.

We also acknowledge that only the centre ~60% of the lung was included in the analysis, which was done to minimize the anatomical differences within CT. The centre slices are typically a good representation of the whole lung, and allow for visualization of all five lobes. To quantify any potential difference this introduced, the VDP for the centre six slices, as used in this study, was subtracted from the whole lung VDP, and there was an average difference of 1±2%, which is less than the VDP minimal clinically important difference of 2%.[1] Further, while texture analysis has been widely studied as a promising method to quantify underlying patterns within medical images, it is known that CT protocol and scanner image reconstruction may influence textural features,[2, 3] and as such, the generalizability of the trained model presented here to other sites at this time is unknown. With that in mind, it is expected that the inclusion of the ratio of VOI features to whole lung feature mean may help mitigate some scanner to scanner variability. The application to a multi-site dataset is necessary to fully quantify the ability to translate the trained model. With a dataset taken from multiple scanners, a feature selection step could be included to select only features which are reproducible across sites. Although a multi-site comparison is a necessary step towards clinical application of texture analysis, many of the density based measures such as RA_{950} and HU_{15} are already successfully used in clinic as well as in multi-site studies.[4, 5] Due to this wide use, and the fact that the largest contributors to the model are these density based measures, it is hypothesized the model may be successful in being generalized to multiple sites.

A general limitation to the work presented in this thesis is the complexity of the prediction problem being addressed. As discussed, previous studies in COPD have shown there are hallmark physiological changes, including tissue destruction and airway inflammation. There are also more recent observations which include vascular abnormalities and airway pruning. To motivate the work presented here, we have hypothesized these changes will not be homogenous throughout the lung, but may be more localized within regions of ventilation defects. This hypothesis has not yet been widely studied, and the notion of vascular abnormalities within defected regions is a current area of research. Despite the current limited knowledge of the research related to the underlying hypothesis of this work, the texture analysis pipeline and results presented here may be an important tool to explore questions of the pathophysiological basis of ventilation defects.

4.4 Future Directions

4.4.1 Robustness of Texture Model

As mentioned in the limitations, future work must be done to study the generalizability of the model created to multi-site datasets. Differences in a multi-site dataset that may effect the texture features include the acquisition parameters, scanner vendor and reconstruction kernel. Within the TINCan dataset, which was acquired at the same site as the data presented in this thesis, there is a subset of patients who underwent scans with varying voxel spacing, ranging from in-plane voxel dimensions of 0.58x0.58mm^2 to 0.85x0.85mm^2. There are fourteen patients with different voxel dimensions, where images were acquired with the same scanner, with the same bag-matched breath hold technique, and with available ground truth hyperpolarized MRI ventilation images. We hypothesize the first-order measures will transfer well to the study with different voxel spacing, however the transferability of the second-order features, as well as those normalized to patient whole lung values, remains unknown. Applying the model generated in Chapter 3 to this subset of patients will allow for conclusions to be drawn on the robustness of the features to different acquisition parameters.

4.4.2 Lung Function Prediction in Lung Cancer

Patient who undergo radiation therapy for lung cancer require treatment plans for the delivery of the treatment. Advances in radiation planning and delivery allow for the possibility to minimize the radiation to certain areas in the lung, and thereby increasing it to other regions. In lung cancer this can be used to create functional lung avoidance plans, where the regions within the lung that have the greatest function are spared in the treatment plan at the expense of regions which are not functioning well, such as ventilation defects.[6-10]

The method developed within this thesis may allow for the extraction of this information from a simple breath hold CT. Lung cancer and COPD are highly related epidemiologically,[11, 12] and therefore it is hypothesized that the results obtained within this thesis indicate similar results may be obtained in lung cancer patients. However, additional complexities will be introduced when training on lung cancer patients. The most obvious will be the presence of the tumor, and the effect that may have on ventilation, as well as the fact that the shape, size and location of tumors vary greatly between lung cancer patients.

4.4.3 Deep Learning for Lung Function Synthesis

There has been a drastic increase in the interest in deep learning for medical image analysis. Both within, and outside, the medical field convolutional neural networks have shown great promise for image classification problems. Recently in a large cohort of COPD patients, deep learning has been applied to create automated disease staging.[13] However, this study also highlights the challenges with deep learning discussed in Section 1.6.1. The large dataset provided a computational challenge, and subsequently the input data used were limited to four slices to represent the whole lung, and only a modest success in predicting disease stage was observed. Despite TINCan not having thousands of images available, this does provide a benefit as the data is very focused and well understood. Additionally, utilizing ventilation images as ground truth provides a more spatially and quantitatively rich measure compared to training to predict a single patient measure such as disease stage.

To apply deep learning to the problem of predicting pulmonary ventilation from single volume thoracic CT, there are two methods which we hope to explore. The first is by utilizing a similar pipeline as presented in Chapter 2 and Chapter 3, where the image is split into volumes of interest, then each VOI is classified as ventilated or not ventilated by utilizing a CNN with a binary classification as the output layer. Another method is to use entire CT image as the input, and have the binary ventilation image as the output layer. Work has been done to create and train architecture for similar tasks of image synthesis, such as predicting a CT image from an MR image.[14, 15]

Each method has its own benefits and limitations. If the VOI prediction is used, there will be a large number of training samples, and it is well known deep learning approaches increase in performance with a large amount of data. However, this method will not fully utilize the spatial relationship between different regions in the image as predictions are made based only on the local information. For example, it is known mucus plugs within the lung are associated with ventilation defects,[16] however, the ventilation defect will extend beyond the abnormality if the airflow obstruction is within one of the large airways. Conversely, the image-to-image synthesis method will be able to more fully account for the relationship between different regions as the neural network is trained on the entire lung volume. However, it will be limited to a smaller number of training samples (in both the case it is trained 2D slice by slice, and especially if trained on the entire 3D volume). Further, training a 3D neural network with an entire CT as the input will be quite computationally intensive.

In both methods, it will be possible to leverage transfer learning – where a network is trained on a larger dataset which allows it to develop the ability to recognize the fundamentals that make up an image, for example learning edge detection. This is often utilized in medical imaging, where networks are trained on large, open-source labeled datasets such as ImageNet. It is hypothesized that an intermediate stage of transfer learning may help with the adaptation to medical images. In this case, there are large open-source labeled datasets of planar chest x-rays.[17] A network originally trained on natural objects in ImageNet, may be applied and fine-tuned to classify the planar chest x-rays, conceivably learning to detect more subtle abnormalities that are seen within lung diseases. This network may then be applied to classify image VOI, or as the encoder/decoder weight initialization for an image synthesis network.

4.5 Significance and Impact

In patients with chronic obstructive pulmonary disease (COPD), structural remodeling of the airways, airway inflammation/obliteration and parenchyma destruction commonly result from chronic inhalation of combustibles including tobacco cigarettes and biomass fuels.[18] Pulmonary x-ray computed tomography (CT) is now widely used to visualize and quantify COPD structural lung abnormalities and these measurements have been exploited in large cohort studies. Hyperpolarized ^{3}He and ^{129}Xe magnetic resonance imaging (MRI) pulmonary measurements also provide high spatial and temporal resolution lung ventilation heterogeneity and microstructural information in COPD patients. The most significant limitation to the widespread application of these techniques is that they are scarcely available due to the high cost of such technology. The methods and models generated in this thesis, when externally validated, will enable translation of ventilation heterogeneity maps using nearly-ubiquitous CT scanners, providing a novel way to generate ventilation maps beyond the few centres with hyperpolarized MRI.

4.6 References

1. Eddy RL, Svenningsen S, McCormack DG, Parraga G. What is the minimal clinically important difference for helium-3 magnetic resonance imaging ventilation defects? Eur Respir J. 2018;51(6).

2. Shafiq-Ul-Hassan M, Zhang GG, Latifi K, et al. Intrinsic dependencies of CT radiomic features on voxel size and number of gray levels. Med Phys. 2017;44(3):1050-62.

3. Yasaka K, Akai H, Mackin D, et al. Precision of quantitative computed tomography texture analysis using image filtering: A phantom study for scanner variability. Medicine (Baltimore). 2017;96(21):e6993.

4. Schroeder JD, McKenzie AS, Zach JA, et al. Relationships between airflow obstruction and quantitative CT measurements of emphysema, air trapping, and airways in subjects with and without chronic obstructive pulmonary disease. AJR Am J Roentgenol. 2013;201(3):W460-70.

5. Coxson HO, Dirksen A, Edwards LD, et al. The presence and progression of emphysema in COPD as determined by CT scanning and biomarker expression: a prospective analysis from the ECLIPSE study. Lancet Respir Med. 2013;1(2):129-36.

6. Hoover DA, Capaldi DP, Sheikh K, et al. Functional lung avoidance for individualized radiotherapy (FLAIR): study protocol for a randomized, double-blind clinical trial. BMC Cancer. 2014;14:934.

7. Ireland RH, Tahir BA, Wild JM, Lee CE, Hatton MQ. Functional Image-guided Radiotherapy Planning for Normal Lung Avoidance. Clin Oncol (R Coll Radiol). 2016;28(11):695-707.

8. Lee E, Zeng J, Miyaoka RS, et al. Functional lung avoidance and response-adaptive escalation (FLARE) RT: Multimodality plan dosimetry of a precision radiation oncology strategy. Med Phys. 2017;44(7):3418-29.

9. Yamamoto T, Kabus S, von Berg J, Lorenz C, Keall PJ. Impact of four-dimensional computed tomography pulmonary ventilation imaging-based functional avoidance for lung cancer radiotherapy. Int J Radiat Oncol Biol Phys. 2011;79(1):279-88.

10. Lavrenkov K, Christian JA, Partridge M, et al. A potential to reduce pulmonary toxicity: the use of perfusion SPECT with IMRT for functional lung avoidance in radiotherapy of non-small cell lung cancer. Radiother Oncol. 2007;83(2):156-62.

11. Young RP, Hopkins RJ, Christmas T, Black PN, Metcalf P, Gamble GD. COPD prevalence is increased in lung cancer, independent of age, sex and smoking history. Eur Respir J. 2009;34(2):380-6.

12. Janssen-Heijnen ML, Schipper RM, Razenberg PP, Crommelin MA, Coebergh JW. Prevalence of co-morbidity in lung cancer patients and its relationship with treatment: a population-based study. Lung Cancer. 1998;21(2):105-13.

13. Gonzalez G, Ash SY, Vegas-Sanchez-Ferrero G, et al. Disease Staging and Prognosis in Smokers Using Deep Learning in Chest Computed Tomography. Am J Respir Crit Care Med. 2018;197(2):193-203.

14. Han X. MR-based synthetic CT generation using a deep convolutional neural network method. Med Phys. 2017;44(4):1408-19.

15. Nie D, Trullo R, Lian J, et al. Medical Image Synthesis with Context-Aware Generative Adversarial Networks. Med Image Comput Comput Assist Interv. 2017;10435:417-25.

16. Dunican E, Fahy J, Mummy D, et al., editors. Regional Ventilation Defects Measured on Hyperpolarized 3He MRI Are Associated with Mucus Plugging Measured on CT in Asthma. American Thoracic Society; 2016.

17. Wang XS, Peng YF, Lu L, Lu ZY, Bagheri M, Summers RM. ChestX-ray8: Hospital-scale Chest X-ray Database and Benchmarks on Weakly-Supervised Classification and Localization of Common Thorax Diseases. 30th Ieee Conference on Computer Vision and Pattern Recognition (Cvpr 2017). 2017:3462-71.

18. Vogelmeier CF, Criner GJ, Martinez FJ, et al. Global Strategy for the Diagnosis, Management, and Prevention of Chronic Obstructive Lung Disease 2017 Report. GOLD Executive Summary. Am J Respir Crit Care Med. 2017;195(5):557-82.

APPENDIX

Appendix A – Hyperpolarized ^{3}He MRI Ventilatory Apparent Diffusion Coefficient of Alpha-1 Antitrypsin Deficiency

In Appendix A we developed a new ^{3}He MRI biomarker of emphysema which incorporates both abnormal ventilation heterogeneity and the apparent diffusion coefficient (ADC) – this biomarker overcomes limitations in longitudinally following emphysema progression using ADC.

The contents of this chapter have previously been published in Journal of Magnetic Resonance Imaging and permission to reproduce the article was granted by John Wiley and Sons and is provided in Appendix C.
A Westcott, DPI Capaldi, A Ouriadov, DG McCormack and G Parraga. Hyperpolarized ^{3}He MRI Ventilatory Apparent Diffusion Coefficient of Alpha-1 Antitrypsin Deficiency. JMRI. 10.1002/jmri.26202.

To the Editor:

Alpha-1 antitrypsin deficiency (AATD) leads to disabling chronic obstructive pulmonary disease (COPD). Current therapy aimed at slowing lung disease progression includes exogenous alpha-1 antitrypsin augmentation therapy but there are few potential new treatments under development. Currently used measurements of AATD-related emphysema include the forced expiratory volume in 1 second (FEV_1) and the diffusing capacity of carbon monoxide (DL_{CO}); both are relatively insensitive to therapy[1] although CT lung density measurements have been shown to worsen more slowly in treated patients.[2]

Hyperpolarized magnetic resonance imaging (MRI) has emerged as a possible alternative or complementary method for evaluating lung microstructure and function.[3] Longitudinal worsening of MRI ventilation-defect-percent (VDP) was shown to be related to symptoms and exercise capacity in COPD patients in whom FEV_1 was not predictive.[4] The apparent diffusion coefficient (ADC) measured using ^{3}He and ^{129}Xe MRI has also been demonstrated in patients with AATD.[5] Although ^{3}He MRI ADC is highly reproducible,[6] these values only report from well-ventilated lung which is important because as AATD emphysema worsens over time, no inhaled gas MRI information can be gleaned from unventilated lung regions.

Our goal was to develop a new biomarker of AATD emphysema that incorporates functional and microstructural abnormalities which would be sensitive to disease changes over time. We evaluated a single patient with a clinical diagnosis of AATD, who provided written informed consent to study protocols (registered at clinicaltrials.gov as NCT02279329 and NCT02723474) approved by a local research ethics board and federal regulatory agency. He was evaluated using spirometry, plethysmography according to guidelines[7] and MRI at each visit; he also completed the St. George Respiratory Questionnaire (SGRQ) and six minute walk test (6MWT) and thoracic CT on a 64-slice Lightspeed VCT scanner (General Electric Healthcare, Milwaukee, WI) (64 × 0.625 mm, 120 kVp, 100 effective mA, tube rotation time = 500 ms, and pitch = 1.0) in breath-hold after inhalation of a 1-L N_2 bag from FRC on visits 2, 4 and 6. The total effective dose was 1.8 mSv (Health Protection Agency of the United Kingdom NRPB-SR250). MRI was performed on a 3T system (MR750 Discovery, GEHC, Milwaukee, WI) as previously described[6] using a multi-slice interleaved 2-dimensional gradient echo diffusion-weighted sequence for seven 30-mm coronal slices (900 µs selective radio frequency pulse, flip angle $\theta = 4°$, echo time = 3.9 ms, repetition time = 5.6 ms, bandwidth = 62.5 kHz, in-plane resolution = $3.125 \times 3.125 \text{mm}^2$, b = 0, 1.6 s/cm^2); the diffusion-sensitization gradient pulse ramp up-down time=500 µs and diffusion time=1460 µs.

The relative area of the CT density-histogram with values < -950 HU (RA_{950}) and MRI ventilation-defect-percent (VDP) were measured using custom-built (MATLAB R2014b; MathWorks, Natick, Mass) software.[8] ADC maps were generated using ^{3}He diffusion-weighted images as previously described.[9] To determine regional information, the apical region was segmented from the basal region based on the location of the carina.

It was previously shown in patients with severe COPD that ventilation defects spatially and quantitatively correlated with emphysematous bullae[10] which reinforces the notion that lung regions with severe emphysema have long time-constants for filling and cannot be ventilated during a short breath-hold scan. To account for this, we considered the diffusing capacity of the lung for carbon monoxide (DL_{CO}) normalized to the ventilated alveolar volume, which generates K_{CO}, as shown in equation 1:

$$K_{CO} = \frac{DL_{CO}}{V_A} \tag{1}$$

where V_A is the alveolar volume, or the "accessible" volume available for gas exchange. In a similar manner, we proposed to normalize ADC in relation to ventilation, which we term the ventilatory ADC (vADC) as:

$$vADC = \frac{ADC}{1-\frac{VDP}{100}} \tag{2}$$

We prospectively evaluated a single AATD patient who attended six visits over a 65 month period and received augmentation therapy for the duration of the study, except for a few months between visit 3 and visit 4. At the first visit where quality of life measurements were recorded, the 6MWD was normal. As shown in Figure 1A, measurements were evaluated using linear regression with the time as the independent variable to calculate slope, r^2 and *p*-value. ^{3}He MRI ventilation and ADC maps show there was qualitative, visually-obvious evidence of increasing ADC values in the apical lung regions and enlarged ventilation defects in the basal lung regions. In Figure 1A and Figure 1C, FEV_1 (slope=-1.8, r^2=0.94, *p*=0.001), RA_{950} (slope=0.86, r^2=1, *p*=0.02), vADC (slope=0.03, r^2=0.77, *p*=0.02), and VDP (slope=2.7, r^2=0.79, *p*=0.02) significantly changed over time (significant non-zero slope). However, DL_{CO} (*p*=0.70), ADC (*p*=0.20) and FEV_1/FVC (*p*=0.05) did not significantly change. These results, along with other important measures, are reflected in the quantitative results shown in Figure 1B.

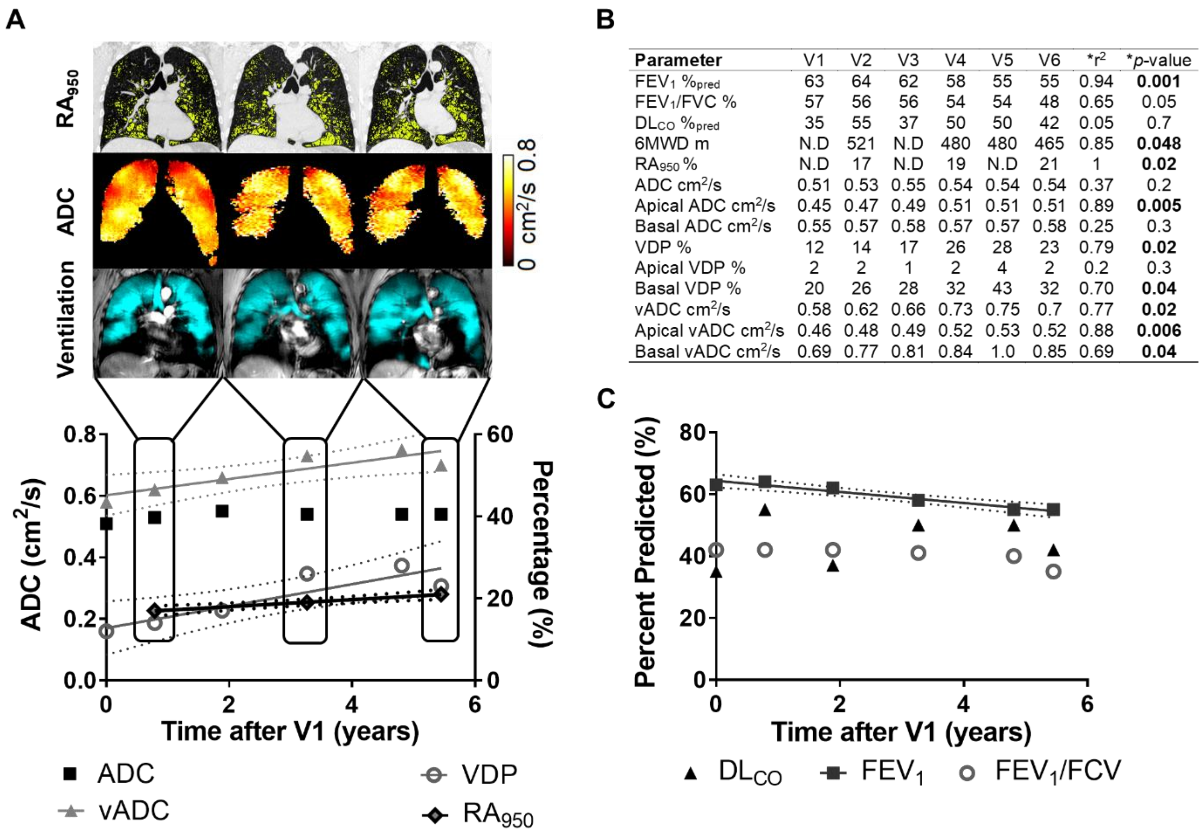

Parameter	V1	V2	V3	V4	V5	V6	*r^2	**p*-value
FEV$_1$ %$_{pred}$	63	64	62	58	55	55	0.94	**0.001**
FEV$_1$/FVC %	57	56	56	54	54	48	0.65	0.05
DL$_{CO}$ %$_{pred}$	35	55	37	50	50	42	0.05	0.7
6MWD m	N.D	521	N.D	480	480	465	0.85	**0.048**
RA$_{950}$ %	N.D	17	N.D	19	N.D	21	1	**0.02**
ADC cm^2/s	0.51	0.53	0.55	0.54	0.54	0.54	0.37	0.2
Apical ADC cm^2/s	0.45	0.47	0.49	0.51	0.51	0.51	0.89	**0.005**
Basal ADC cm^2/s	0.55	0.57	0.58	0.57	0.57	0.58	0.25	0.3
VDP %	12	14	17	26	28	23	0.79	**0.02**
Apical VDP %	2	2	1	2	4	2	0.2	0.3
Basal VDP %	20	26	28	32	43	32	0.70	**0.04**
vADC cm^2/s	0.58	0.62	0.66	0.73	0.75	0.7	0.77	**0.02**
Apical vADC cm^2/s	0.46	0.48	0.49	0.52	0.53	0.52	0.88	**0.006**
Basal vADC cm^2/s	0.69	0.77	0.81	0.84	1.0	0.85	0.69	**0.04**

Figure 1: A) Longitudinal imaging measurements and ^{3}He MRI static ventilation (cyan) coregistered with ^{1}H MRI; ^{3}He MRI apparent diffusion coefficient (ADC) maps; Thoracic CT RA$_{950}$ maps; **B)** Participant measurements over 65 months; **C)** Clinical pulmonary function measurements, 95 % confidence intervals shown for significant regressions.
FEV$_1$=forced expiratory volume in 1 second; %$_{pred}$=percent predicted; FVC=forced vital capacity; DL$_{CO}$=diffusing capacity of the lungs for carbon monoxide; 6MWD=Six minute walk distance; VDP=ventilation defect percent; ADC=apparent diffusion coefficient; RA$_{950}$=relative area of the CT density histogram of attenuation values <-950 Hounsfield Units; vADC=ventilatory ADC.

In this proof of concept demonstration, it is important to note that vADC was generated and used based on the assumption that in patients with advanced COPD, ventilation defects are dominated by emphysematous bullae and not airways disease.[10] This is certainly also the case in AATD patients where emphysematous destruction dominates. However, in patients with mild COPD, ventilation defects also derive from gas trapping due to small-airways disease[10] and for these patients, different weightings of the ratio of ADC and VDP should be generated and tested. In this specific AATD patient with GOLD grade 2 COPD and severe emphysema, vADC, and VDP as well as apical ADC, RA$_{950}$, 6MWD and FEV$_1$

significantly changed over the 65 month followup period. Somewhat surprisingly, this was not the case for DL_{CO}, perhaps because it can be highly variable over time.

We also observed that vADC significantly increased in both apical and basal regions, whereas VDP did not significantly change in the apical regions and ADC did not significantly change in the basal lung regions. These findings are certainly consistent with previous longitudinal MRI results in COPD patients in whom worsening emphysematous bullae resulted in larger ventilation abnormalities as disease progressed. We acknowledge that vADC has not been widely tested yet and a large scale study is required in patients with severe emphysema that includes both K_{CO} and patient outcomes. Nevertheless, this preliminary study in a single AATD patient showed that vADC significantly changed while ADC did not. Moreover, vADC changes were concordant with significantly worse 6MWD and CT measurements which supports its use as a biomarker of airspace enlargement in patients with severe emphysema.

REFERENCES

1. Schluchter MD, Stoller JK, Barker AF, et al. Feasibility of a clinical trial of augmentation therapy for alpha(1)-antitrypsin deficiency. The Alpha 1-Antitrypsin Deficiency Registry Study Group. Am J Respir Crit Care Med. 2000;161(3 Pt 1):796-801.

2. Chapman KR, Burdon JG, Piitulainen E, et al. Intravenous augmentation treatment and lung density in severe alpha1 antitrypsin deficiency (RAPID): a randomised, double-blind, placebo-controlled trial. Lancet. 2015;386(9991):360-8.

3. Kauczor HU, Ebert M, Kreitner KF, et al. Imaging of the lungs using 3He MRI: preliminary clinical experience in 18 patients with and without lung disease. J Magn Reson Imaging. 1997;7(3):538-43.

4. Kirby M, Pike D, Sin DD, Coxson HO, McCormack DG, Parraga G. COPD: Do Imaging Measurements of Emphysema and Airway Disease Explain Symptoms and Exercise Capacity? Radiology. 2015;277(3):872-80.

5. Ouriadov A, Lessard E, Sheikh K, Parraga G, Canadian Respiratory Research N. Pulmonary MRI morphometry modeling of airspace enlargement in chronic obstructive pulmonary disease and alpha-1 antitrypsin deficiency. Magn Reson Med. 2017;79(1):439-48.

6. Parraga G, Ouriadov A, Evans A, et al. Hyperpolarized 3He ventilation defects and apparent diffusion coefficients in chronic obstructive pulmonary disease: preliminary results at 3.0 Tesla. Invest Radiol. 2007;42(6):384-91.

7. Miller MR, Hankinson J, Brusasco V, et al. Standardisation of spirometry. Eur Respir J. 2005;26(2):319-38.

8. Kirby M, Heydarian M, Svenningsen S, et al. Hyperpolarized 3He magnetic resonance functional imaging semiautomated segmentation. Academic radiology. 2012;19(2):141-52.

9. Kirby M, Heydarian M, Wheatley A, McCormack DG, Parraga G. Evaluating bronchodilator effects in chronic obstructive pulmonary disease using diffusion-weighted hyperpolarized helium-3 magnetic resonance imaging. J Appl Physiol (1985). 2012;112(4):651-7.

10. Kirby M, Pike D, Coxson HO, McCormack DG, Parraga G. Hyperpolarized (3)He ventilation defects used to predict pulmonary exacerbations in mild to moderate chronic obstructive pulmonary disease. Radiology. 2014;273(3):887-96.

Appendix B - Rapid Single-breath Hyperpolarized Noble Gas MRI Based Biomarkers of Airspace Enlargement.

In Appendix B we used accelerated 129Xe MRI to generate alveolar morphometry estimates in patients with COPD and alpha-1 antitrypsin deficiency. The use of accelerated MRI allows for collection of the data in a single breath-hold scan, versus multiple-breath methods previously used. I was co-first author on this work with my colleague Fumin Guo.

The contents of this chapter have previously been published in Journal of Magnetic Resonance Imaging and permission to reproduce the article was granted by John Wiley and Sons and is provided in Appendix C.
A Westcott, F Guo, G Parraga and A Ouriadov. Rapid single-breath hyperpolarized noble gas MRI-based biomarkers of airspace enlargement. 10.1002/jmri.26574.

INTRODUCTION

Chronic obstructive pulmonary disease (COPD), characterized by both small airway dysfunction and airspace enlargement, is a leading cause of morbidity and mortality and is responsible for 700,000 costly hospitalization days annually in the United States.[1] Important and promising work with ^{3}He MRI has led to the development of physiologically relevant biomarkers of obstructive lung disease including the apparent diffusion coefficient (ADC) and mean linear intercept (L_m), derived from multi-b diffusion weighted MRI and utilized to probe the microstructure of the lung.[2] Due to the increasing scarcity and cost of ^{3}He, the continuation of hyperpolarized gas imaging necessitates decreasing the number of ^{3}He doses or moving towards the use of ^{129}Xe.[3-5] However, the low gyromagnetic ratio of ^{129}Xe and the gradient strengths typical for clinical scanners (5G/cm) dictate that rapid MRI acquisition strategies be developed to facilitate the uptake of ^{129}Xe diffusion-weighted imaging.[6] This is especially true for multi-b diffusion-weighted MRI because currently, whole lung datasets are difficult to acquire during the relatively short 10-16 second breath-hold timeframe[7] feasible in patients with lung disease. However, it was recently demonstrated[8] that 6 b-value, lower spatial resolution (7x7x30mm3 voxels) whole-lung coverage can be achieved in 10 seconds using a GRAPPA approach with a dedicated, phased receive-array coil system.

Previously, three-dimensional multi-b diffusion-weighted MRI[9] required a number of independent doses of gas for each slice as typically 4 or 5 different b values (including 0) are required in order to generate curves with sufficient data for analysis and each of these b values requires a single breath-hold image with freshly inhaled gas contrast,[7] culminating in a total of three xenon doses. This is an important cost and time/patient effort issue. Therefore, the ability to accelerate the acquisition has the potential to provide cost savings in two critical areas: the cost of the xenon gas, and the time needed for the scans. Each xenon dose costs approximately \$250 US (1L of 50/50 ^{129}Xe/^{4}He, 86% enriched), in addition to an average collection time of 20 minutes per xenon bag, necessitating at least an hour of personnel and patient time for three separate scans. Further, multiple scans can lead to lung volume variability and patient distress or fatigue. While a multi-breath approach has been feasible in small research studies, the increased time for acquisition, the potential for lung volume mismatch and repeated doses of hyperpolarized gas will likely not be compatible with larger scale clinical examinations or use. Recently, a stretched-exponential-model[10] combined with under-sampling in the imaging and diffusion directions[11] was proposed for the evaluation of hyperpolarized gas multiple b-value diffusion-weighted MRI. The major advantage of this method is the possibility to significantly speed up data acquisition using acceleration factors (AF) between 7 and 10.[11] This is potentially more rapid than the compressed-sensing methods recently published for diffusion-weighted MRI[10] and also provides high spatial resolution images. This approach provides a method to generate four non-zero b-values for diffusion-weighted ^{129}Xe MRI in a single breath-hold, or alternatively be applied to combine ^{3}He static ventilation and multi-b diffusion weighted scans into a single breath-hold. We hypothesized that a previous method[11] could be extended to provide whole lung hyperpolarized gas MRI-based emphysema biomarkers for ^{3}He and ^{129}Xe, including static-ventilation (SV), T_2*,[12] ADC and morphometry maps with high spatial image resolution. Therefore, in this proof-of-concept evaluation, our objective was to develop a rapid, cost-efficient and patient friendly approach that generates emphysema biomarkers in a small group of patients with emphysema.

THEORY

In pulmonary diffusion MRI, the limitations of non-renewable gas hyperpolarization, breath-hold duration, and the inherently longer diffusion-weighted scans have motivated the development of rapid image acquisition and reconstruction techniques. Accordingly, previous efforts have focused on accelerated image acquisition including parallel imaging, compressed sensing, deep learning and combinations of these approaches. For example, k-t methods (e.g., k-t BLAST/SENSE) represent a model-based approach that employs the prior information of signal covariance matrix from training data to improve image resolution.[13] K-t methods were also combined with compressed sensing (e.g., k-t SPARSE, k-t FOCUSS) to reconstruct high spatial-temporal resolution images with minimal aliasing artefacts from under-sampled data. In particular, k-t FOCUSS[14] comprises of a prediction step, a residual encoding step, and the optimal sample allocation between the two. Another model-based approach, MARTINI,[15] employs mono-exponential T_2 decay as prior, and directly estimates tissue properties (T_2 and spin density) from a set of under-sampled k-space data using a nonlinear inverse reconstruction algorithm. Other approaches including SAKE,[16] LORAKS[17] and ALOHA[18] arrange k-space data into a structured annihilating filter-based Hankel matrix and employ the low-rankness of the matrix for image reconstruction. In particular, SAKE investigates the correlation between multiple receiver coils, LORAKS requires finite spatial support and smooth phase prior, ALOHA relates transform sparsity to low-rankness of the Hankel matrix in the Fourier domain and reconstructs images through matrix completion. Here we employed a compressed sensing-based framework with a Split Bregman numerical solver to reconstruct high resolution images from under-sampled k-space data by exploiting the implicit spatial and b-value sparsity of MR images.

We denote $I = \{I_1^H, I_2^H \ldots I_N^H\}^H$ as the N ventilation images that we aim to reconstruct from undersampled k-space data $f = \{f_1^H, f_2^H \ldots f_N^H\}^H$ corresponding to the N b-values, where H represents Hermitian transpose. Here the spatial sparsity of each diffusion MR image is mathematically formulated using total variation (TV) of the image, i.e. $|\nabla I_i|$. In addition, the sparsity along the b-value direction can be regarded as the gradient of diffusion MR images I_i and I_{i-1} acquired at adjacent b-values b_i and b_{i-1}, $i = 2 \ldots N$, i.e.,

$$MI_i = I_i - I_{i-1} \cdot e^{-\left((\bar{D}b_i)^{\bar{\alpha}} - (\bar{D}b_{i-1})^{\bar{\alpha}}\right)}, \tag{1}$$

where $\bar{D}$ and $\bar{\alpha}$ are the mean diffusivity and heterogeneity values, respectively, and can be estimated from previously acquired images.[11] To this end, we proposed to reconstruct the images I from undersampled k-space data f in both the spatial and b-value directions while maintaining data consistency as follows:

$$\min_I \alpha\|\nabla I\|_1 + \beta\|MI\|_1 + \frac{\mu}{2}\|FI - f\|^2, \qquad [2]$$

where M is the linear operator defined in Eqn. [1], F represents the undersampled Fourier transform, α, β and μ are positive constants that balance the weight of three terms.

The unconstrained TV-ℓ_1/ℓ_2 optimization problem in Eqn. [2] was solved using a Split Bregman algorithm[19] and we note that it can also be solved using convex optimization techniques.[20] The Split Bregman algorithm introduces a number of dummy variables, i.e., $d_x = \nabla_x I$, $d_y = \nabla_y I$ and $m = MI$, for each constraint weighted by constant λ. The Split Bregman algorithm iterates in two phases until convergence:

1. $(I^{k+1}, d_x^{k+1}, d_y^{k+1}, m^{k+1}) = \arg\min_{I,d_x,d_y,m} \alpha\|d_x\| + \alpha\|d_y\| + \beta\|m\| + \frac{\mu}{2}\|FI - f^k\|^2 + \frac{\lambda}{2}\|d_x - \nabla_x I - b_x^k\|^2 + \frac{\lambda}{2}\left\|d_y - \nabla_y I - b_y^k\right\|^2 + \frac{\lambda}{2}\|m - MI - b_m^k\|^2$. This step can be spilt into several subproblems each optimizing a single variable sequentially because these variables are independent from each other. In particular, the subproblem of I involves only ℓ_2-norm and can be solved analytically.

2. Update the dummy variables as: $b_{x,y}^{k+1} = b_{x,y}^k + \nabla_{x,y} I^{k+1} - d_{x,y}^{k+1}$, $b_m^{k+1} = b_m^k + MI^{k+1} - m^{k+1}$ and $f^{k+1} = f^k + f - FI^{k+1}$.

The signal dependence related to diffusion-sensitization can be determined through the probability density function or diffusion propagator (P) for fluid diffusion in confined media with unknown geometry:[21-23]

$$S(b)/S_0 = \int_0^\infty P(D)\exp(-D\cdot\bar{b})\,dD \qquad [3]$$

where S(b) is the signal at a particular b-value and S_0 is the MR signal-intensity in the absence of diffusion-sensitizing gradients. The diffusion propagator can be ascertained through the inverse Laplace transform of S(b)[22] and to apply this, the analytical representation for S(b) is required. Thus, experimental S(b) values can be fit as demonstrated for multi-b diffusion-weighted ^{3}He MRI[10, 11, 23] as follows:

$$S(b)/S_0 = \exp(-D' \cdot \bar{b})^{\alpha} \quad [4]$$

where D' is the apparent diffusivity and α is the heterogeneity index ($0<\alpha\leq 1.0$). The diffusion propagator can be determined through substitution of Eqn. [4] into Eqn. [1] and then applying the inverse Laplace transform:[22]

$$P(D) = \frac{B/D'}{(D/D')^{(1-\alpha/2)/(1-\alpha)}} \exp\left[-\frac{(1-\alpha)\alpha^{\alpha/(1-\alpha)}}{(D/D')^{\alpha/(1-\alpha)}}\right] f(D) \quad [5]$$

And

$$f(D) = \begin{cases} 1/[1+C\,(D/D')^{(0.5\alpha-\alpha^2)/(1-\alpha)}], \\ \alpha \leq 0.5, \\ 1+C\,(D/D')^{(0.5\alpha-\alpha^2)/(1-\alpha)}, \\ \alpha > 0.5 \end{cases} \quad [6]$$

where f(D) is the auxiliary function and parameters B and C are functions of the heterogeneity index.[22] Mean D estimates can be determined using the probability density function distribution to calculate specific to acinar duct mean diffusion length maps[21] ($Lm_D = \sqrt{2\Delta D}$, where Δ is the diffusion time and D is the diffusivity). For multi-b diffusion-weighted ^{3}He MRI, L_m is empirically observed to be proportional to Lm_D:[23]

$$L_m = -562\,\mu m + 4.3 \cdot Lm_D \quad [7]$$

Lm_D depends on both diffusion time and diffusivity, so Eqn. [7] cannot be used for ^{129}Xe MRI-based L_m estimates. In order to extend Eqn. [7] to ^{129}Xe gas, the empirical relationship in Eqn. [8] was previously determined and proposed:[24]

$$L_m = -562\,\mu m + 4.3 \cdot Lm_D \cdot \sqrt{\frac{2D_0^{He}\,\Delta_{He}}{2D_0^{Xe}\,\Delta_{Xe}}} \quad [8]$$

where D_0^{He} is the diffusion coefficient of ^{3}He (0.88 cm^2/s) in gas mixture, Δ_{He}=1.46 ms, D_0^{Xe} is the diffusion coefficient of ^{129}Xe (0.12 cm^{2}s^{-1}/0.14 cm^{2}s^{-1} [25]) in gas mixture and Δ_{Xe} is the diffusion time.

MATERIALS and METHODS

Study Participants

We enrolled 12 participants, including four never-smokers, four COPD ex-smokers with emphysema and one alpha-1 antitrypsin deficiency (AATD) patient with COPD who were included in the retrospective study as well as three COPD ex-smokers with emphysema who were included in the prospective study; all provided written informed consent to an ethics board-approved protocolthat was compliant with the Health Insurance Portability and Accountability Act (HIPAA, USA). Ex-smokers with COPD and AATD patients with COPD were enrolled between 50-80 years of age; never-smokers without a history of tobacco smoking or chronic respiratory disease were enrolled between 45-80 years of age.

Pulmonary Function Tests and CT

Spirometry, plethysmography and the diffusing-capacity-of-the-lung-for-carbon-monoxide (DL_{CO}) were performed according to American Thoracic Society (ATS) guidelines[26] using a plethysmograph and attached gas analyzer (MedGraphics Corporation. St. Paul, MN USA). X-ray computed tomography (CT) was also performed supine (64-slice Lightspeed VCT scanner GEHC, Milwaukee, WI USA; 64×0.625 mm, 120 kVp, effective mA=100, tube rotation time=500 ms, pitch=1.0) using a spiral acquisition in breath-hold after inhalation of 1L N_2 from functional residual capacity (FRC). A slice thickness of 1.25 mm and standard convolution kernel were used.

^{129}Xe and ^{3}He MRI Acquisition

MRI was performed at 3T (MR750, GEHC, Waukesha WI) using whole-body gradients (G_{max}=5 G/cm, slew rate=200 $mTm^{-1}s^{-1}$) as previously described.[7] ^{129}Xe gas (86% enriched, measured polarization 12-40%) was provided by commercial polarizer systems (XeBox-E10, Xemed LLC, Durham, NH; XeniSpin™, Polarean Inc, Durham, NC). All subjects inhaled 1L of a 50/50 by volume ^{129}Xe/^{4}He gas mixture from functional residual capacity (FRC). In all xenon measurements the diffusion-sensitization gradient pulse ramp up/down time=500 μs, constant time=2 ms, Δ_{Xe}=5 ms, providing four b-values 0, 12.0, 20.0, and 30.0 s/cm^2. Three ^{129}Xe doses were used in the diffusion-weighted measurements, except for a single AATD patient who could not undertake multiple breath-holds, and in whom data was acquired in a single xenon dose at a lower resolution to obtain whole lung coverage with a diffusion-weighted, whole lung 3D FGRE pulse sequence. For patients with COPD and never-smokers, two interleaved acquisitions (diffusion-weighted, multi-slice 2D Fast Gradient Recall Echo (FGRE) pulse sequence (similar to Figure 1A), TE/TR=9.8msec/11.0msec, matrix size=128x80, number of slices=7; slice thickness=30 mm, and FOV=40x40 cm^2) one with and one without diffusion-sensitization (i.e. b=0 and b=12 s/cm^2 or b=0 and b=20 s/cm^2 or b=0 and b=30 s/cm^2) for each line of k-space in each image slice were acquired to ensure that RF depolarization (optimal 5^o constant flip angle was used) and T_1 relaxation effects were minimal.[7] For ^{129}Xe MRI in the AATD patient, four interleaved acquisitions (diffusion-weighted, whole lung 3D FGRE, 0.5ms rectangular RF pulse, VFA, TE/TR=9.0msec/10.0msec, matrix size=64x64, number of slices=8; slice thickness=30 mm, and FOV=40x40 cm^2). Four interleave cycles were initiated at the maximum b-value (b=30s/cm^2) to ensure that maximum MR signal was acquired at greater b-values as previously described.[23]

For ^{3}He MRI, polarized ^{3}He gas (polarization ~40%) was provided by a commercial system (Helispin^{TM}, Polarean Inc, Durham, NC [27]). Subjects inhaled 1L of a $^3He/N_2$ a gas mixture (30/70 by volume) from FRC as previously described.[28] For ^{3}He MRI, an accelerated (AF=7) multi-slice interleaved (six interleaves) centric 2D FGRE diffusion-weighted sequence (Figure 1A and B) under-sampled in the imaging and diffusion direction as it is shown in Figure 1C (bottom panel)[11] was acquired for seven 15mm coronal slices (reconstructed matrix size=128x128, total acquisition time=12 s, 0.9 ms selective RF pulse, TE/TR=4.1ms/5.6ms, bandwidth=62.5 kHz, FOV=40x40 cm^2, b=0, 1.6, 3.2, 4.8, 6.4 s/cm^2). An optimal 7.4^o constant-flip-angle (120 [20 per b-value] RF pulses per slice) was used.

Figure 1 outlines the pulse sequence used and the k-space sampling method, where the sparsity occurs in the diffusion direction, as shown using the varying sampling patterns for different b-value images. The diffusion-sensitization gradient pulse ramp up/down time=0.5 ms with Δ_{He}=1.46 ms which was initiated at the maximum *b*-value to ensure that maximum MR signal was acquired at greater *b*-values as previously described.[23] Additionally, a short-TE (TE=1.3ms) b=0 image was used to generate the SV image and T_2* map. A single breath-hold was used to generate all ^{3}He maps.

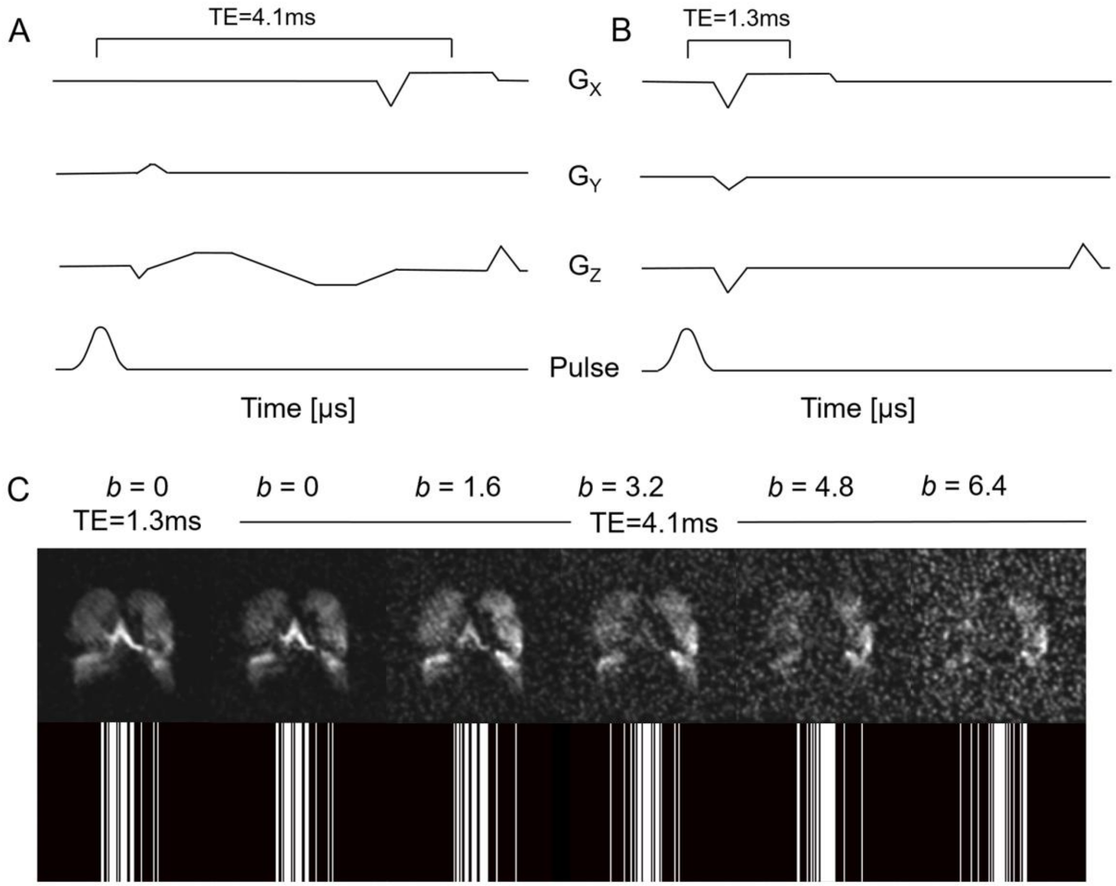

Figure 1: MRI Pulse Sequence Schematic, Sparsity Pattern and Reconstructed ^{3}He Images A) Diffusion-Weighted, Multi-Slice 2D Fast Gradient Recall Echo (FGRE) pulse sequence with diffusion-sensitizing along z-direction. Δ=1.46ms, TE=4.1ms. Five interleaves, starting at the maximum b-value (6.4 s/cm^2) ensures multiple b-value approach; B) An extra interleave with no diffusion-weighting (b=0) and significantly reduced TE (1.3ms) utilized to generate a short TE static ventilation image and T_2* map by using a long TE static ventilation image (b=0) from A); C) k-space under-sampling scheme (bottom panel), ensuring a variety of sparsity patterns for each b-value (AF=7) employed in diffusion direction, with resulting images where the signal decay with higher diffusion gradient induced signal decay is evident. A short TE static ventilation image, a long TE static ventilation image and four diffusion-weighted images (top panel) shown from left to right. The SNR value varies from 35 (short TE static ventilation image) to 4 (maximum b-value image).

Image Analysis

^{129}Xe data were retrospectively under-sampled in both imaging and diffusion directions ensuring AF=7 to validate the reconstruction method[11] and using the regularization parameters previously determined.[19] A single slice (six images) reconstruction was completed within approximately 2-3 minutes using Matlab 2016 on a standard PC workstation with 3.0GHz CPU using a previously developed approach.[11] The ADC (b=0 and 12 s/cm^2) and morphometry maps ((Lm_D),[10] mean-linear-intercept (L_m)[23]) were generated as previously described[11, 23] and compared with corresponding maps calculated for the fully-sampled k-spaces. ^{3}H MRI data were reconstructed as previously described,[11] and static-ventilation (short-TE image), T_2* (TE$_1$/TE$_2$=1.3ms/4.1ms), ADC (0 and 1.6 s/cm^2) and morphometry (Lm_D/L_m) maps were generated. (MATLAB R2017 MathWorks, Natick, MA) was used to generate all hyperpolarized gas maps. Image SNR was calculated using a 15x15 voxel square region of interest inside a lung region of homogeneous signal and using the same 15x15 voxel square region of interest outside the lung where there is no lung signal.[29]

A semi-automated segmentation approach was used to generate ventilation defect percent (VDP), as previously described.[30] ADC maps were generated for two b-values on a voxel-by-voxel basis as previously described.[4] The relative area of the CT density histogram with attenuation values <-950 Hounsfield units (RA$_{950}$)[31] was determined using Pulmonary Workstation 2.0 (VIDA Diagnostics Inc., Coralville, IA).

Statistics

Differences between ADC and L_m values generated from fully and undersampled k-space were calculated on a voxel-by-voxel basis for a single slice[10] using Eqn. [9]:

$$\text{Difference} = \sum_{i=1}^{N}\sum_{j=1}^{M}\left[\frac{\text{FullySampled}_{ij} - \text{Undersampled}_{ij}}{\text{FullySampled}_{ij}}\right]\cdot 100\% \qquad [9]$$

where N and M are the corresponding image matrix sizes. Multivariate analysis of variance (MANOVA) and independent t-tests were performed using SPSS Statistics, V22.0 (SPSS Inc., Chicago, IL). Results were considered significant when the probability of two-tailed type I error (α) was less than 5% ($p<.05$).

RESULTS

Table 1 summarizes pulmonary function, CT and demographic measurements for all participants. Figure 1C (top panel) shows representative images reconstructed from the under-sampled data in the imaging and diffusion direction of k-space (bottom panel, AF=7) including a short TE static ventilation image, a long TE static ventilation image and four diffusion-weighted images shown from left to right. The SNR value varied from 35 (short TE static ventilation image) to 4 (maximum b-value image).

Table 1: Participant demographic and imaging measurements.

Parameter (Mean±SD)	Emphysema Subjects (n=8)			Never-Smokers (n=4, ^{129}Xe)
	COPD (n=3, ^{3}He)	COPD (n=4, ^{129}Xe)	AATD (n=1, ^{129}Xe)	
Male Sex n (%)	3(100)	3 (75)	1 (100)	2 (50)
Age years	81 (6)	68 (10)	67 (-)	66 (13)
FVC $\%_{pred}$	104 (40)	100 (21)	102 (-)	102 (8)
FEV_1 $\%_{pred}$	89 (37)	58 (30)	55 (-)	103 (6)
FEV_1/FVC %	82 (84)	42 (14)	40 (-)	76 (2)
RV $\%_{pred}$	46 (43)	160 (57)	170 (-)	102 (9)
TLC $\%_{pred}$	60 (50)	123 (8)	130 (-)	102 (8)
RV/TLC $\%_{pred}$	50 (43)	48 (14)	131 (-)	39 (9)
DL_{CO} $\%_{pred}$	56 (6)	39 (13)	50 (-)	104 (12)
VDP %	20 (6)	28 (14)	-	4 (.3)
RA_{950} %	-	19 (9)	-	-

COPD=ex-smoker with COPD; FEV_1=forced-expiratory-volume-1-sec; %pred= percent-predicted; FVC=forced-vital-capacity; RV=residual-volume; TLC=total-lung-capacity; DL_{CO}=diffusing capacity of the lung for carbon monoxide; VDP=ventilation defect percent; RA_{950}=relative area of the CT density histogram < - 950 Hounsfield units

Figure 2 shows centre coronal slice CT and MRI ventilation images as well as MRI ADC and L_m maps for a representative never-soker, COPD and AATD patients obtained for fully-sampled and retrospectively accelerated methods. CT images reflected low attenuating areas (<-950 HU) in the COPD/AATD patients with RA_{950}=12% and 19% respectively, where the AATD CT is from a visit 19 months prior.

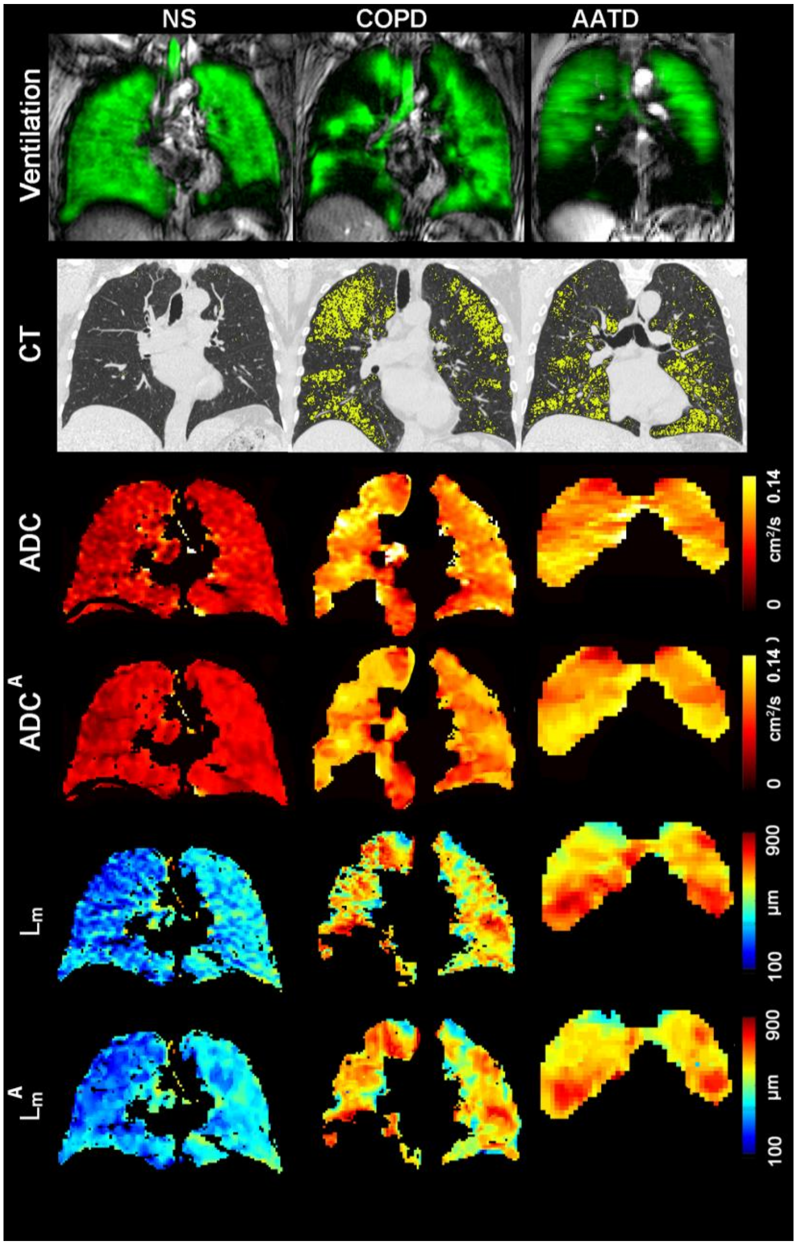

Figure 2: Representative CT and ^{129}Xe MRI Maps

SV=MRI static ventilation; ADC=apparent-diffusion-coefficient; L_m=MRI mean-linear-intercept; ADC^A=ADC obtained with accelerated approach; L_m^A= L_m obtained with accelerated approach.

NS=Elderly never-smoker, FEV_1=105%$_{pred}$, DL_{CO}=94%$_{pred}$, RA_{950}=0.14%, ADC/ADC^A=0.05cm^2 s^{-1}/0.05cm^{2}s^{-1}, L_m/L_m^A=300µm/280µm, VDP=3.92%;

COPD=Ex-smoker with COPD, FEV_1=59%$_{pred}$, DL_{CO}=43%$_{pred,}$ RA_{950}=12%, ADC/ADC^A =0.08cm^2 s^{-1}/0.08cm^{2}s^{-1}, L_m/L_m^A=540µm/550µm, VDP=15%;

AATD=alpha-one antitrypsin deficiency, FEV_1=58%$_{pred}$, DL_{CO}=50%$_{pred}$, RA_{950}=19%, ADC/ADC^A =0.08cm^2 s^{-1}/0.09cm^{2}s^{-1}, L_m/L_m^A=580µm/570µm, VDP=27%.

Table 2 summarizes ^{129}Xe airspace enlargement biomarkers calculated from the center slice, ADC and L_m, for all ^{129}Xe study participants. Mean ADC/ADC^A, (^{A}=acceleration) and L_m/L_m^A estimates for the never-smokers (0.05cm^{2}s^{-1}/0.05cm^{2}s^{-1} and 290µm /280µm) were significantly smaller than the corresponding mean estimates for COPD/AATD patients (0.09cm^{2}s/0.09cm^{2}s and 540µm/530µm; all $p<.001$) for fully-sampled and accelerated methods. For the never-smoker subgroup, a mean difference of 14%/12% was observed between the fully-sampled and the accelerated approach for the ADC and L_m values, respectively. For the COPD subgroup a mean difference of 12%/8% was observed between fully-sampled and accelerated data ADC and L_m values, respectively. For the AATD subject a mean difference of 11%/9% observed between fully-sampled and accelerated data ADC and L_m values, respectively.

Table 2: ^{129}Xe MRI Parenchyma Measurements and Morphometry Estimates.

	ADC cm^2/s	**ADC^A cm^2/s**	**L_m µm**	**L_m^A µm**	**ADC difference**	**L_m difference**
Never-Smoker	**.05 (.01)**	**.05 (.01)**	**290 (100)**	**280 (110)**	**14%**	**12%**
NS-1	.04 (.01)	.05 (.01)	310 (90)	320 (80)	9%	10%
NS-2	.05 (.02)	.05 (.01)	280 (110)	260 (90)	16%	14%
NS-3	.04 (.01)	.04 (.01)	280 (90)	280 (150)	16%	12%
NS-4	.05 (.01)	.05 (.01)	300 (120)	280 (100)	15%	13%
COPD	**.09 (.02)**	**.08 (.01)**	**490 (120)**	**480 (250)**	**12%**	**8%**
COPD-1	.10 (.02)	.10 (.01)	500 (130)	480 (120)	12%	8%
COPD -2	.08 (.02)	.08 (.01)	540 (100)	550 (90)	9%	6%
COPD -3	.08 (.02)	.08 (.01)	450 (120)	440 (100)	13%	8%
COPD -4	.09 (.03)	.08 (.02)	490 (140)	480 (120)	16%	9%
AATD	**.08 (.02)**	**.09 (.02)**	**580 (140)**	**570 (130)**	**11%**	**9%**
NS-COPD/AATD p-value	**<0.001**	**<0.001**	**<0.001**	**<0.001**	**0.4**	**<0.01**

NS= Never-Smokers; COPD=COPD ex-smoker; AATD=alpha-one antitrypsin deficiency; ADC=apparent-diffusion-coefficient; L_m=MRI mean-linear-intercept; ADC^A=ADC obtained with accelerated approach; L_m^A= L_m obtained with accelerated approach.

Figure 3 shows representative center slice SV, T_2*, ADC, Lm_D and L_m maps for three COPD subjects reconstructed from the originally under-sampled k-space (AF=7). Table 3 shows mean estimates of T_2* ADC, Lm_D and L_m and the signal-to-noise (SNR) values for b=0/b=6.4s/cm^2 images and SV image used to calculate ventilation-defect-percent.[4]

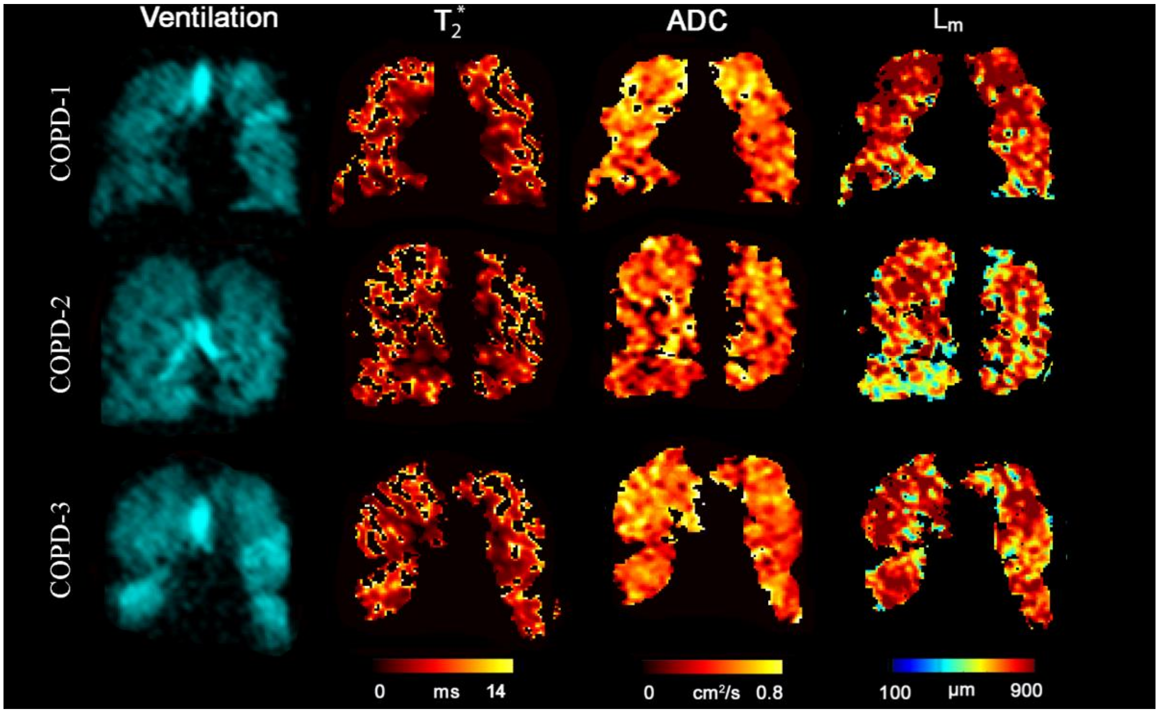

Figure 3: Representative ^{3}He MRI Maps obtained for COPD patients
Ventilation = MRI Static Ventilation Image; VDP = MRI ventilation defect percentage; T_2* = MRI free induction decay time constant; ADC = MRI apparent-diffusion-coefficient; Lm_D = MRI mean-airway-length-scale; L_m = MRI mean-linear-intercept;
COPD-1: VDP =6, T_2* = 7 ms, ADC =0.50 cm^2 s^{-1}, Lm_D = 290 µm, L_m = 800 µm
COPD-2: VDP =17, T_2* = 8 ms, ADC = 0.40 cm^2 s^{-1}, Lm_D= 270 µm, L_m = 680 µm
COPD-3: VDP = 17, T_2* = 9 ms, ADC = 0.40 cm^2 s^{-1}, Lm_D= 290 µm, L_m = 760 µm

Table 3: ^{3}He MRI Parenchyma Measurements

Parameter (SD)	COPD-1	COPD-2	COPD-3
VDP, %	6	17	17
T_2* (ms)	7 (5)	8 (5)	9 (5)
ADC (cm^2/s)	0.50 (0.15)	0.40 (0.15)	0.40 (0.15)
Lm_D (µm)	290 (40)	270 (40)	290 (40)
L_m (µm)	800 (190)	680 (180)	760 (170)
SNR (SV)	30	25	30
SNR (b=0)	22	17	20
SNR (b=6.4s/cm^2)	6	4	6

COPD=COPD ex-smoker; VDP = ventilation defect percentage; T_2*= free induction decay time constant; ADC = apparent diffusion coefficient; Lm_D = mean airway length scale; L_m = mean linear intercept estimate; SV = static ventilation; SNR = signal to noise ratio.

DISCUSSION

In this proof-of-concept study, we investigated the feasibility of undersampling in imaging and diffusion-weighted directions for potential use as a clinical tool. In a single ^{3}He breath-hold we were able to obtained static ventilation SV, T_2*, ADC and morphometry maps using ^{3}He diffusion-weighted lung MRI in a single 16 sec breath-hold. Further, we demonstrated that this acceleration scheme may be applied to ^{129}Xe imaging in order to acquire whole lung ADC and morphological measurements in a single breath-hold, without significant penalty to imaging information. In both nuclei, this acceleration can help save up to two gas doses, decrease MRI scan time, and make the scan more tolerable for a patient with lung disease.

By acquiring VDP/T_2*/ADC/morphometry estimates during a single ^{3}He scan, we eliminate the need for two separate static ventilation and diffusion-weighted scans. The ^{3}He T_2*-results suggested that T_2* values were in the 7-9ms interval for severe emphysema patients; ^{3}He MRI T_2* values have previously been measured in young healthy volunteers on 3T GE (7±1.4ms) [32] and Philips (10.8±1.8ms) MRI systems.[29] The mean T_2* values we reported were in the same range (7-9 ms), and therefore, the free induction decay estimates we generated were likely physiologically realistic for the age and disease status of the participants in this study. Likely, T_2* estimates depend on alveolar surface-to-volume ratio and, therefore, can be potentially used as a biomarker. Another potential role for T_2* mapping is signal correction. The SNR of static ventilation images, which ranged between 25 and 30, was more than adequate for VDP calculations and can be generated alongside ADC values in a single rapid breath-hold.[4] Moreover, the SNR we observed was typical for multi b-value diffusion-weighed data acquired without acceleration.[33] Thus, no special denoising procedure was required prior to regularized reconstruction.

In order to validate this acceleration method, we conducted a sub-study with fully-sampled ^{129}Xe data. For all participants the mean ADC/ADC^A values as well as L_m/L_m^A values were not significantly different between acquisition methods (all p>.4). For the never-smoker subgroup, a mean difference of 14%/12% was observed between the fully-sampled and the accelerated approach for the ADC and L_m values, respectively and this difference was not significant. For the COPD subgroup, a mean difference of 12%/8% was observed between the fully-sampled and the accelerated approach for the ADC and L_m values, respectively and this was not significant. AATD subject results have confirmed that ADC/L_m MRI estimates can be obtained in a single 16 sec breath-hold with the accelerated method. Figure 2 shows that there is a difference between right and left lung in a COPD patient. This is likely due to volume mismatch between the multiple-b value breath-hold co-registered images. If this is indeed the cause, this highlights the importance of a single breath method for multiple-b value collections. Acceleration provides numerous advantages for difficult clinical cases (by limiting the number of breath-holds required in respiratory-compromised patients), for reduction of costs and for reduction of image analysis requirements that stem from multiple breath-hold scans. For example, by reducing the need for up to 5 different contrast gas breath-holds, the cost was reduced from approximately $US 1200 to $US 200 for the gas contrast which is in the same cost range as blood-based contrast agents. The time required to acquire the data is also reduced from approximately 40 minutes to 10 minutes. Both of these savings combine and result in substantial time and dollar cost savings as well as improved patient comfort and safety/tolerability.

In this development study, we acknowledge a number of important study limitations, including potential errors introduced into the fully-sampled data from multiple breath-holds, as well as possible errors introduced because of low SNR. When separate breath-holds are employed, image co-registration is required to ensure voxel-wise spatial agreement between images. Unfortunately, co-registration results are not always accurate, and this further highlights the need for, and importance of a single breath method for multiple-b value acquisitions. We also recognize and acknowledge that for maximum b-value images, SNR is less than the Rose criteria of SNR=5,[34] which serves as a general guide for image quality. However, this is an expected signal reduction due to the strong diffusion attenuation for the patients with severe emphysema (Figure 1C, top panel). Nevertheless, for larger b-value images, such as the $b=6.4 s/cm^2$ image, the relative values are low compared to the lower b-value images so the influence on curve fitting is also low. Certainly, low SNR images must also be considered as a limitation, however, new polarization methods onboard commercially-available turnkey systems have recently increased ^{129}Xe polarization levels (~40% polarization of a 400ml volume in 15-20 minutes) with the result being substantially improved image quality and SNR. We also recognize that for this study, we used D, α and Lm_D values of best-fit and did not collect statistics on the fitting error/residual to exclude pixels. Finally, Eqn. [8] was not validated with histology or morphometry methods and this is in contrast to Eqn. [7].[23] However, we note that Eqn. [8] was used only to validate the proposed acceleration method reconstruction by applying retrospective k-space under-sampling to the multiple breath-hold data so this would not likely influence the reliability of the accelerated diffusion-weighted multi b-value ^{3}He MRI method.

Accelerated ^{129}Xe MRI provides a way to generate alveolar morphometry estimates to regionally characterize emphysema and airspace enlargement in patients with COPD and AATD in a single breath-hold scan using a single gas dose. This means that multi-breath methods (which are not as cost-efficient and may lead to lung volume variability and patient distress or fatigue) or longer duration scans are no longer required and can be replaced with accelerated methods. The emphysema biomarkers obtained for this pilot study in COPD patients are the first demonstration of this acceleration (7x) method.

REFERENCES

1. Collaborators USBoD. The state of us health, 1990-2010: Burden of diseases, injuries, and risk factors. JAMA. 2013;310(6):591-606.

2. Yablonskiy DA, Sukstanskii AL, Woods JC, et al. Quantification of lung microstructure with hyperpolarized 3He diffusion MRI. J Appl Physiol. 2009;107(4):1258-65.

3. Mugler JP, 3rd, Altes TA. Hyperpolarized 129Xe MRI of the human lung. J Magn Reson Imaging. 2013;37(2):313-31.

4. Kirby M, Svenningsen S, Owrangi A, et al. Hyperpolarized 3He and 129Xe MR imaging in healthy volunteers and patients with chronic obstructive pulmonary disease. Radiology. 2012;265(2):600-10.

5. Kaushik SS, Cleveland ZI, Cofer GP, et al. Diffusion-weighted hyperpolarized 129Xe MRI in healthy volunteers and subjects with chronic obstructive pulmonary disease. Magn Reson Med. 2011;65(4):1154-65.

6. Kaushik SS, Robertson SH, Freeman MS, et al. Single-breath clinical imaging of hyperpolarized 129xe in the airspaces, barrier, and red blood cells using an interleaved 3D radial 1-point Dixon acquisition. Magn Reson Med. 2016;75(4):1434-43.

7. Ouriadov A, Farag A, Kirby M, McCormack DG, Parraga G, Santyr GE. Lung morphometry using hyperpolarized (129) Xe apparent diffusion coefficient anisotropy in chronic obstructive pulmonary disease. Magn Reson Med. 2013;70(6):1699-706.

8. Chang YV, Quirk JD, Yablonskiy DA. In vivo lung morphometry with accelerated hyperpolarized (3) He diffusion MRI: a preliminary study. Magn Reson Med. 2015;73(4):1609-14.

9. Pike D, Mohan S, Ma W, Lewis JF, Parraga G. Pulmonary imaging abnormalities in an adult case of congenital lobar emphysema. J Radiol Case Rep. 2015;9(2):9-15.

10. Chan HF, Stewart NJ, Parra-Robles J, Collier GJ, Wild JM. Whole lung morphometry with 3D multiple b-value hyperpolarized gas MRI and compressed sensing. Magn Reson Med. 2017;77(5):1916-25.

11. Abascal JFPJ, Desco M, Parra-Robles J. Incorporation of prior knowledge of the signal behavior into the reconstruction to accelerate the acquisition of MR diffusion data. ArXiv e-prints [Internet]. 2017; 1702. Available from: http://adsabs.harvard.edu/abs/2017arXiv170202743A.

12. Xu X, Norquay G, Parnell SR, et al. Hyperpolarized 129Xe gas lung MRI–SNR and T2* comparisons at 1.5 T and 3 T. Magn Reson Med. 2012;68(6):1900-4.

13. Tsao J, Boesiger P, Pruessmann KP. k-t BLAST and k-t SENSE: dynamic MRI with high frame rate exploiting spatiotemporal correlations. Magn Reson Med. 2003;50(5):1031-42.

14. Jung H, Ye JC, Kim EY. Improved k-t BLAST and k-t SENSE using FOCUSS. Phys Med Biol. 2007;52(11):3201-26.

15. Sumpf TJ, Uecker M, Boretius S, Frahm J. Model-based nonlinear inverse reconstruction for T2 mapping using highly undersampled spin-echo MRI. J Magn Reson Imaging. 2011;34(2):420-8.

16. Shin PJ, Larson PE, Ohliger MA, et al. Calibrationless parallel imaging reconstruction based on structured low-rank matrix completion. Magn Reson Med. 2014;72(4):959-70.

17. Haldar JP. Low-rank modeling of local k-space neighborhoods (LORAKS) for constrained MRI. IEEE Trans Med Imaging. 2014;33(3):668-81.

18. Lee D, Jin KH, Kim EY, Park SH, Ye JC. Acceleration of MR parameter mapping using annihilating filter-based low rank hankel matrix (ALOHA). Magn Reson Med. 2016;76(6):1848-64.

19. Goldstein T, Osher S. The Split Bregman Method for L1-Regularized Problems. SIAM J Imaging Sci. 2009;2(2):323-43.

20. Guo F, Yuan J, Rajchl M, et al. Globally optimal co-segmentation of three-dimensional pulmonary 1H and hyperpolarized 3He MRI with spatial consistence prior. Med Image Anal. 2015;23(1):43-55.

21. Parra-Robles J, Marshall H, Hartley RA, Brightling CE, Wild JM. Quantification of lung microstructure in asthma using a 3He fractional diffusion approach [abstract]. ISMRM 22nd Annual Meeting. 2014:3529.

22. Berberan-Santos MN, Bodunov EN, Valeur B. Mathematical functions for the analysis of luminescence decays with underlying distributions 1. Kohlrausch decay function (stretched exponential). Chemical Physics. 2005;315(1-2):171-82.

23. Ouriadov A, Lessard E, Sheikh K, Parraga G, Canadian Respiratory Research N. Pulmonary MRI morphometry modeling of airspace enlargement in chronic obstructive pulmonary disease and alpha-1 antitrypsin deficiency. Magn Reson Med. 2018;79(1):439-48.

24. Ouriadov A, Lessard E, Guo F, et al. Accelerated Diffusion-weighted 129Xe MRI Morphometry of Emphysema in COPD and Alpha-1 Antitrypsin Deficiency Patients [abstract]. ISMRM 25th Annual Meeting, Honolulu, Hawaii, USA. 2017([abstract]):1763.

25. Ouriadov A, Farag A, Kirby M, McCormack DG, Parraga G, Santyr GE. Pulmonary hyperpolarized (129) Xe morphometry for mapping xenon gas concentrations

and alveolar oxygen partial pressure: Proof-of-concept demonstration in healthy and COPD subjects. Magn Reson Med. 2015;74(6):1726-32.

26. Miller MR, Hankinson J, Brusasco V, et al. Standardisation of spirometry. Eur Respir J 2005;26(2):319-38.

27. Miller G, Altes T, Brookeman J, De Lange E, Mugler Iii J. Hyperpolarized 3He lung ventilation imaging with B 1-inhomogeneity correction in a single breath-hold scan. Magn Reson Mater Phys Biol Med. 2004;16(5):218-26.

28. Kirby M, Pike D, McCormack D, et al. Longitudinal Computed Tomography and Magnetic Resonance Imaging of COPD: Thoracic Imaging Network of Canada (TINCan) Study Objectives. J COPD F. 2014;1(2):200-11.

29. Dominguez-Viqueira W, Ouriadov A, O'Halloran R, Fain SB, Santyr GE. Signal-to-noise ratio for hyperpolarized (3)He MR imaging of human lungs: a 1.5 T and 3 T comparison. Magn Reson Med. 2011;66(5):1400-4.

30. Kirby M, Heydarian M, Svenningsen S, et al. Hyperpolarized 3He magnetic resonance functional imaging semiautomated segmentation. Acad Radiol. 2012;19(2):141-52.

31. Zach JA, Newell Jr JD, Schroeder J, et al. Quantitative CT of the Lungs and Airways in Healthy Non-Smoking Adults. Investigative radiology. 2012;47(10):596.

32. Deppe MH, Parra-Robles J, Ajraoui S, et al. Susceptibility effects in hyperpolarized 3He lung MRI at 1.5T and 3T. J Magn Reson Imaging. 2009;30(2):418-23.

33. Paulin GA, Ouriadov A, Lessard E, Sheikh K, McCormack DG, Parraga G. Noninvasive quantification of alveolar morphometry in elderly never- and ex-smokers. Physiol Rep. 2015;3(10).

34. Rose A. The sensitivity performance of the human eye on an absolute scale. J Opt Soc Am. 1948;38(2):196-208.

Appendix C - Advanced Pulmonary MRI to Quantify Alveolar and Acinar Duct Abnormalities: Current Status and Future Clinical Applications

Appendix C is a review article presenting a historical overview of measurements of alveolar and acinar duct abnormalities, from ex vivo studies to current in vivo measurements, as utilized in Appendix A and Appendix B.

The contents of this chapter have previously been published in Journal of Magnetic Resonance Imaging and permission to reproduce the article was granted by John Wiley and Sons and is provided in Appendix C.
A Westcott, DG McCormack, G Parraga and A Ouriadov. Advanced pulmonary MRI to quantify alveolar and acinar duct abnormalities: Current status and future clinical applications. 10.1002/jmri.26574.

OVERVIEW

Chronic diseases of the lung frequently involve parenchymal tissue destruction and/or fibrosis, terminal airspace enlargement, bronchiectatic airways and emphysematous damage. Such chronic lung diseases include but are not limited to, interstitial lung disease and fibrosis, chronic obstructive pulmonary disease (COPD), bronchopulmonary dysplasia (BPD) related to extreme preterm birth, bronchiolitis obliterans related to lung transplant and emphysema related to alpha-one antitrypsin deficiency (AATD). The development of new therapies and the longitudinal monitoring of disease progression and response to therapy in patients has been challenging because currently there are no clinically-available, direct, non-invasive *in vivo* measurements of the lung tissue pathologies that mechanistically drive disease initiation and progression. To address this serious clinical and knowledge gap, highly sensitive and specific measurements of lung parenchyma abnormalities, are required. In this review, we focus on obstructive lung diseases such as COPD and BPD and review currently used *ex vivo* measurement tools including histological and micro-CT measurements of biopsy samples. We also summarize emerging pulmonary magnetic resonance imaging (MRI) methods that provide non-invasive *in vivo* measurements of the terminal bronchioles and acinar duct geometry and morphology. We discuss important new findings related to these developments, as well as future research directions and clinical opportunities.

RATIONALE: CLINICAL GAPS AND UNANSWERED QUESTIONS

For over 7 decades, the spirometry measurement of the forced expiratory volume in 1s (FEV_1), first invented in the 1800s,[1] has remained the clinical measurement tool for diagnosing chronic lung disease and for informing clinical management of patients over time. Unfortunately, it is well-understood that FEV_1 is insensitive to changes in the parenchyma and small airways that are now believed to be the sites where chronic lung disease initiates.[2, 3] Moreover, parenchymal changes that alter the acinar ducts and diminish the surface area for gas exchange are currently clinically measured using the diffusing capacity of the lungs for carbon monoxide (DL_{CO}). While DL_{CO} measurements are relatively inexpensive and straightforward to acquire, rigorous quality assurance of equipment is required and even in frequently and expertly calibrated units, DL_{CO} measurements can be highly variable over time in patients[4] which has effectively limited its use in longitudinal studies.[5] As an alternative, CT lung density and airway measurements may be qualitatively or quantitatively evaluated[6] although the combination of the limited spatial resolution of thoracic CT (1mm isotropic) and radiation burden does not support the use of CT for longitudinal or serial investigations, especially in young or middle-aged patients. Unfortunately, therefore, there remain significant gaps in our understanding of how chronic lung disease initiates and progresses at the level of the acinar ducts and terminal bronchioles. Moreover, it is difficult if not impossible to sensitively measure response to therapy in patients.

HISTORICAL FRAMEWORK

Histology and Stereology

Some of the earliest understandings of lung disease pathogenesis stemmed from the pivotal work of Leopold and Gough,[7] over six decades ago. Their histological evaluation of 140 post-mortem emphysema samples (all but 10 male) were fixed under inflation and compared with normal post-mortem findings. They made qualitative observations using light microscopy of two-dimensional fixed samples which were ground-breaking; using this approach, they made the first descriptions of the pathogenesis of emphysema in relation to inflammation, bronchiolar caliber and emphysematous airspace enlargement.

This seminal work and questions about the underlying physiology being probed by the DL_{CO} measurement motivated the development of three-dimensional lung morphometry approaches and measurements based on two-dimensional cross- sectional histology samples, by a number of groups and pioneered by Weibel, Ochs and colleagues.[8, 9] As shown in Figure 1, the overall three-dimensional structure of the lungs may be discerned and measured using stereology methods.[10, 11] Stereological measurements of excised lung sections include, through-point counts, intersect counts and transect-counting, from which an estimation of lung volume, surface area or mean linear intercept (L_m) can be made.[12-14] While this approach has been fundamental to our understanding of lung disease pathogenesis, unfortunately, it relies on excised lung tissue from post-mortem or post-surgical samples and thus this is limited to *ex vivo* analyses. This certainly limits longitudinal evaluations and hence this approach tends to focus on single time-point or cross-sectional studies.

Micro-Computed tomography (CT)

The concept of micro-CT was first developed in the early 1980s,[15-17] where this method was employed by material scientists for imaging the internal structures of small objects. Some of these early conceptual developments were commercialized in the early 1990s[18, 19] and scanners that typically comprised of an X-ray source (focal diameter <100 µm) and a thin x-ray detector were used to enable *ex vivo* and small animal *in vivo* samples measurements. In fact, currently used micro-CT in combination with synchrotron radiation provides images with approximately 10µm isotropic spatial resolution.[20] Turn-key, commercially available micro-CT systems have been employed to visualize and quantify lung tissue measurements in mice,[21] rats,[22-25] pigs[26] and cadaveric human lung specimens.[20, 27, 28] Micro-CT has also been applied to study patient lung tissue samples, as shown in Figure 1, and provides a way to generate high spatial resolution images of normal and abnormal parenchyma tissue resected from patients.[3] However, micro-CT scan speed and the radiation doses needed to generate images with the spatial resolution required to measure lung abnormalities means that the method is feasible mainly for *ex vivo* and cadaveric or end-stage small animal model tissue measurements.[29, 30]

Figure 1: Lung tissue histology and micro-CT images.
Top panels show histology slides for normal and COPD patient and scalar bar is 500 µm adapted from Woods et al. 2006 Mag Reson Med.[103] Bottom panels show micro-CT images for normal and emphysematous tissue with scalar bar 1mm, adapted from Watz et al. 2005 Radiology.[27]

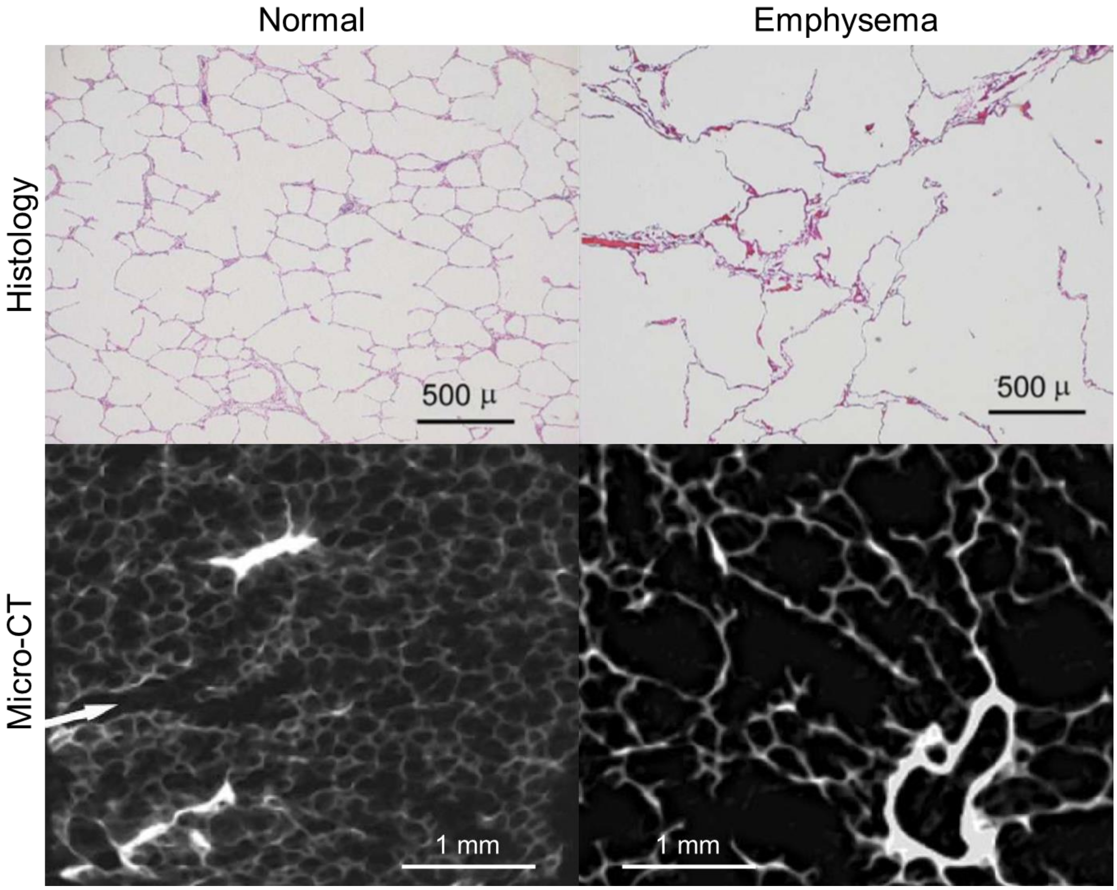

Thoracic CT

Important pathological observations made using *ex vivo* morphometry have led an American Thoracic Society/European Respiratory Society (ATS/ERS) joint task force to consider this approach as the gold standard for evaluating clinical interventions, severity of disease and response to treatment.[31] Translating such *ex vivo* findings to inform clinical treatment decisions and disease monitoring requires *in vivo*, non-invasive measurements such as provided using clinical thoracic x-ray computed tomography (CT). CT was first used for pulmonary exams in the late 1970s, and this led to a number of studies of COPD-related emphysema studies.[32-36] For over three decades now, low dose, multi-detector thoracic CT has provided this opportunity in patients with a wide variety of chronic lung diseases.[37-40] In particular, thoracic CT provides a way to visualize the large airways and provide measurements such as wall thickness and lumen diameter *in vivo*. Due mainly to dose and to spatial resolution limitations, it is typically possible to segment and measure airways to the ~7th generation. Despite these spatial resolution limits, CT provides macroscopic quantitative measures which indirectly informs on the microstructure within a voxel, based on the premise that a voxel near -1000 Hounsfield Units (HU) contains minimal parenchymal tissue. Quantitative measures that are commonly used include the relative area < -950 HU (RA_{950}), the 15th percentile HU and slope calculated from low attenuating clusters.[41-43] In addition to CT emphysema measurements, CT may also be used to evaluate lung surface area to volume ratios.[44] The advent and development of thoracic CT has provided enormous clinical and research value for *in vivo* lung measurements, but its use is still limited because of radiation exposure concerns in patients and because of the fundamental spatial resolution of method itself.

HYPERPOLARIZED NOBLE GAS MRI

Overview

Recently, hyperpolarized noble gas magnetic resonance imaging (MRI) has been employed to visualize and measure pulmonary structure and function *in vivo* in patients. The pulmonary hyperpolarized gas MRI era started with the publication of mouse lung ^{129}Xe MRI by pioneers in the field of hyperpolarization physics.[45] The original observations led to the development of inhaled noble gas diffusion-weighted measurements in animal models of emphysema[46] and in patients with COPD.[47] Because serial monitoring is critical gap for small animal and patient studies, non-invasive inhaled hyperpolarized magnetic resonance imaging (MRI) has emerged as a possible alternative or complementary method for evaluating lung microstructure and function.[48, 49] Importantly, during a 10-15s breathhold, diffusion-weighted pulse sequences may be employed to determine the apparent diffusion coefficient (ADC) of ^{3}He[47] and ^{129}Xe[50] gases, both of which have been measured in COPD patients with emphysema[51] and in AATD patients.[52] The ^{3}He MRI ADC was shown to be highly reproducible[48, 53] and to correlate with DL_{CO},[54] reflecting regional emphysema.[55] MRI diffusion-weighted pulse sequences provide maps and regional ADC measurements that reflect the Brownian motion of the inhaled gas that is restricted within the airways and alveoli.[56] Because ^{3}He in particular and ^{129}Xe to a lesser extent is inert, its displacement reflects the size of the alveolar structures that restrict its movement. As such, pulmonary MRI ADC values provide non-invasive estimates of alveolar dimensions; these have been used to measure the microanatomical abnormalities associated with emphysema in COPD.[47, 55, 57-63]

It is reasonable to ask the question: ***Why MRI in patients with obstructive lung disease?*** MRI has been used to investigate emphysematous changes in current and ex-smokers[64-66] with COPD and to monitor potential lung regrowth in rodents[67] and lung cancer patients.[68, 69] The relationship of *in vivo* MRI estimates and histological measurements in excised tissues were also determined.[70, 71] These previous results have generated a strong foundation for the optimization and strategic clinical research application of MRI in patients, to directly measure treatment efficacy and help accelerate the development of novel therapies including cell-based and whole organ replacement therapy. Therefore, as there have been a number of thorough reviews on the history, technological background and development of hyperpolarized gas MRI,[72-74] this review will focus on the emerging sub-field of hyperpolarized gas morphometry, and the unique role it can play in guiding patient management.

MRI Apparent Diffusion Coefficients

Estimates of the self-diffusion coefficient of liquids or gases are based on the Einstein equation:

$$D = \frac{< r >^{2}}{2nt_{d}}, \qquad [1]$$

where D is a self-diffusion coefficient, $<r>^{2}$ is the mean square displacement of a Brownian molecule, n is a dimension (n=1, 2, 3) and t_{d} is the diffusion observation time. If D does not depend on the diffusion observation time and the direction of diffusion, there is by definition, free isotropic diffusion which may be characterized using Gaussian distributions.[75] However, liquid or gas diffusion inside a confined media may deviate from the free isotropic diffusion, and in such cases, D is a function of $t_{d,}$ and is more appropriately described as an Apparent Diffusion Coefficient (ADC), which depends on both t_d and the geometry of the confining medium. MRI ADC measurements typically require only two data points, one with and another without a single-direction diffusion-sensitizing pulse. D values may also depend on the direction of the diffusion measurement or is anisotropic so that diffusion in one direction is more rapid than in another direction. An example of anisotropic diffusion is a gas molecule diffusion inside the Weibel model of an acinar duct airway,[76] shown in Figure 2 with the added assumption of non-permeable walls[75] and infinitely long ducts. In such a model, the diffusion measured along the duct direction or a longitudinal diffusion (with anisotropic diffusion coefficient (D_L)) should approach free diffusion. However, the diffusion measured perpendicular to the duct axis direction, or a transverse diffusion (with anisotropic diffusion coefficient (D_T)) is restricted by that dimension. Restricted or non-free diffusion means that diffusing gas molecules start to interact with the duct walls, the transverse diffusion becomes restricted and the measured D_T should be less than D_L based on Eq [1]. This intuitive example demonstrates that gas molecules can be utilized with MRI to probe the micro-geometry of alveoli with submillimeter spatial resolution even when voxels are significantly larger in size. A number of theories describing restricted diffusion features were published where the main focus was extraction of geometric information, such as the size and shape of pores or channels[77-80] and the surface-to-volume ratio (S/V) of porous space.[81, 82]

Table 1: Typical MRI acquisition parameters

	2D Diffusion-weighted ^{3}He MRI	**3D Diffusion-weighted ^{129}Xe MRI**	**3D Diffusion-weighted ^{129}Xe MRI With CS AF=7**
TR/TE (ms)	3.9/5.6	11/10	11/10
Flip Angle	4^{o}	VFA	VFA
FOV (cm^2)	40 x 40	40 x 40	40 x 30
Matrix size	128 x 80	128 x 80	128 x 128
Slice number	7	7	7
Orientation	Coronal	Coronal	Coronal
Voxel size (mm^3)	3.1 x 3.2 x 30	3.1 x 3.2 x 30	3.1 x 3.2 x 30
b-value (s/cm^2)	0, 1.6, 3.2, 4.8, 6.4	0, 12, 20, 30, 40	0, 12, 20, 30, 45
Diffusion time (ms)	1.46	5	5.2
Scan time (sec)	16	>16*	>16
Cylinder (ref 85)	Yes	Yes	Yes

Single Compartment (ref 52)	Yes	No	No
Stretched Exponential (ref 90)	Yes	No	Yes

VFA= variable flipped angle; FOV=field of view; TR= relaxation time; TE=echo time *16s for two b-values only. CS=compressed sensing, AF=acceleration factor.

Figure 2: Schematic for Weibel Acinar Duct cylindrical model
Cylinder model of acinar airways showing the two anisotropic diffusion coefficients: D_L representing diffusion parallel to the acinar airway and D_T representing diffusion perpendicular to the acinar airway. The dashed arrows show the directions of the two anisotropic diffusion coefficients where R = external airway radius, r = internal airway radius, h = alveolar sleeve depth and L = alveolar length. Adapted from Yablonskiy et al. 2002 PNAS (51).

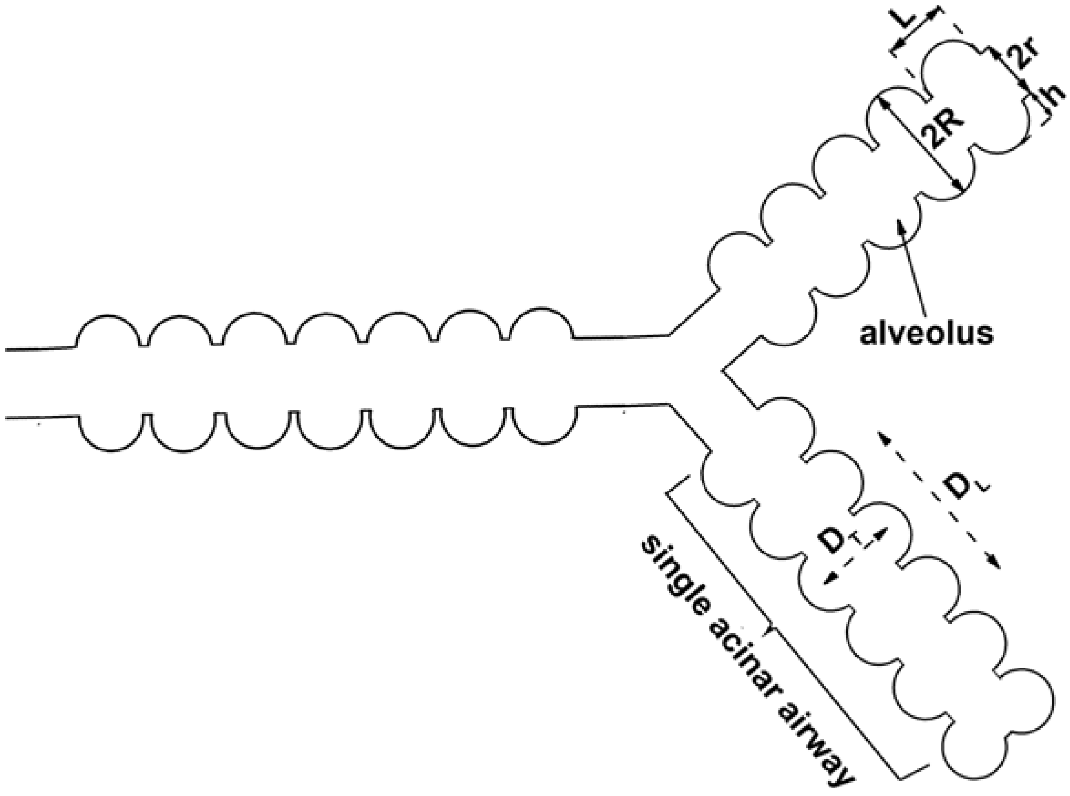

MRI Sub-voxel Resolution Morphometry Modelling

To provide clinically-relevant measurements of alveolar sizes and geometries, MRI morphometry was first proposed by Yablonskiy[27] using hyperpolarized ^{3}He MRI and further developed by a team of pioneers in St Louis at Washington University.[58, 61, 83-85]

MRI morphometry requires multiple-b value sampling (four different b-values or more) in order to probe a wide range of the alveolar sizes. To model MRI diffusion measurements, the Weibel model of the acinar duct was first employed and this resembles a long cylinder that represents the terminal bronchiole with acini. Using this specific geometry, anisotropic diffusion coefficients D_L and D_T depend on the internal (r) and external (R) radii of the acinar duct (Figure 2) in multi-b value measurements. Correlations between clinically relevant alveolar estimates such as mean airspace chord length, alveolar surface-to-volume ratio and MRI-derived r/R (shown in Figure 2) have been observed.[86]

Figure 3: Hyperpolarized ^{3}He MRI Static Ventilation and Apparent Diffusion Coefficient Maps and Thoracic CT
Ex-smoker with COPD: FEV_1=32%$_{pred}$, FEV_1/FVC=28%$_{pred}$, DL_{CO}=37%$_{pred}$, RA_{950} = 18%; and AATD patient: FEV_1=61 %$_{pred}$, FEV_1/FVC=60%, DL_{CO}=21%$_{pred}$, RA_{950} = 31%; MRI and thoracic CT with RA_{950} mask in yellow

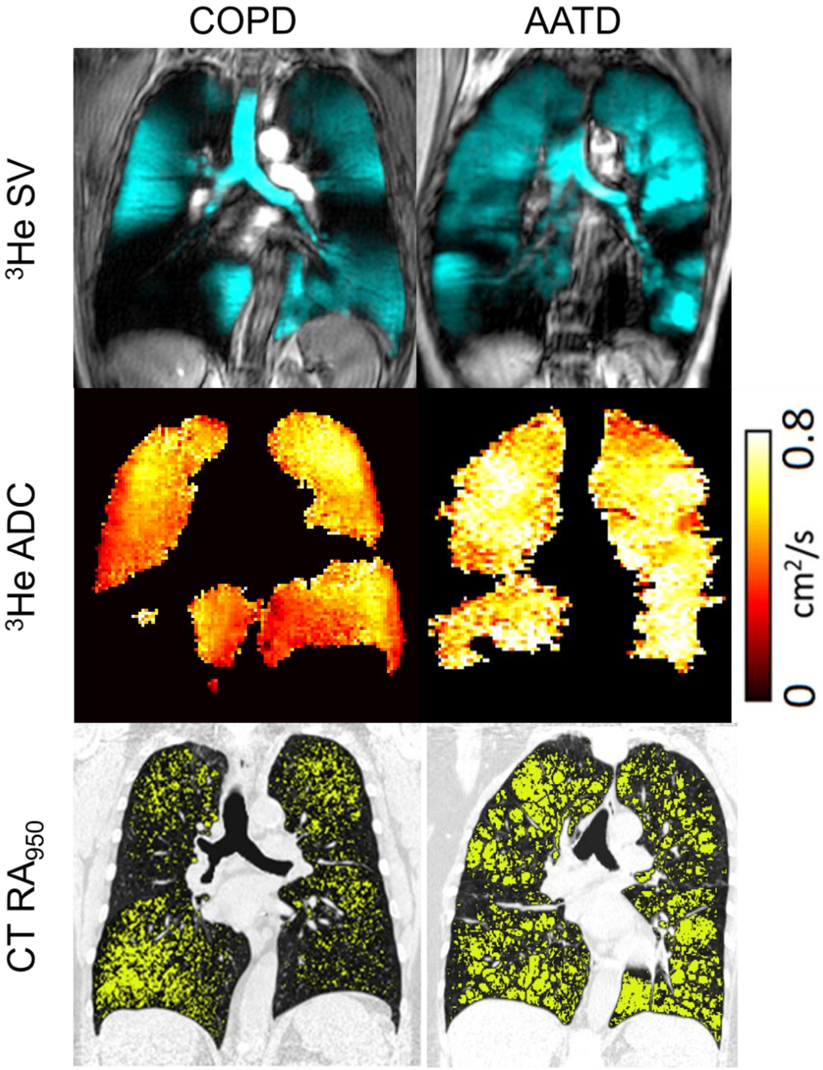

COPD = Ex-smoker with COPD, AATD: = Alpha-1 antitrypsin deficiency, Yellow pixels on CT RA_{950} maps correspond to voxels < -950 Hounsfield Units.

Recently, an alternative to the cylinder model -the stretched exponential model was developed and this approach does not assume any underlying geometry, and so this may be used to fit any multi-b diffusion attenuation using general signal decay equations[87] and a dedicated mathematical framework.[88] Because the stretched exponential model does not assume any specific geometry for the acinar duct, MRI estimates based on this approach still require validation with histological ground truth and with the morphometry estimates based on the cylinder model.[52] A major advantage of the stretched exponential model approach is that it may be combined with compressed sensing[89] to accelerate image acquisition using under-sampling in the imaging and diffusion directions.[90]

Currently, a cylinder morphometry model is the most widely-used, and is histologically-validated[70] in patients and histology/micro CT-validated in animal models.[71, 91-93] Although the cylinder model has a complete mathematical framework for both ^{3}He and ^{129}Xe clinical/pre-clinical lung morphometry,[85, 94, 95] most morphometry studies were conducted with ^{3}He gas. This is largely due to increased scan times needed for ^{129}Xe measurements, which makes the stretched exponential model a promising alternative. Figure 4 shows representative centre slice ^{3}He morphometry and CT images obtained for COPD, AATD and BPD patients. The bottom panel shows MRI-derived L_m maps generated for these patients all of whom show different emphysema patterns. For the representative COPD patient, there was augmented ADC reflecting emphysema in the apical lung regions (hotter colours indicate larger L_m values). The distribution of MRI-derived L_m values were also in agreement with the regional distribution of CT RA_{950}.

Figure 4: Hyperpolarized ^{3}He MRI-derived L_m and thoracic CT RA_{950} in patients with COPD, AATD and BPD.

Top panel is ex-smoker with COPD; FEV_1=126%$_{pred}$, FEV_1/FVC=63%, DL_{CO}=62%$_{pred}$, RA_{950} = 11%, L_m = 500 µm; middle panel is AATD patient; FEV_1=58%$_{pred}$, FEV_1/FVC= 41%, DL_{CO}=50%$_{pred}$, RA_{950} = 17%; L_m = 720 µm and bottom panel is BPD patient; FEV_1=36%$_{pred}$, FEV_1/FVC= 39%, DL_{CO}= 76%$_{pred}$, RA_{950} = 16%, L_m = 420 µm.

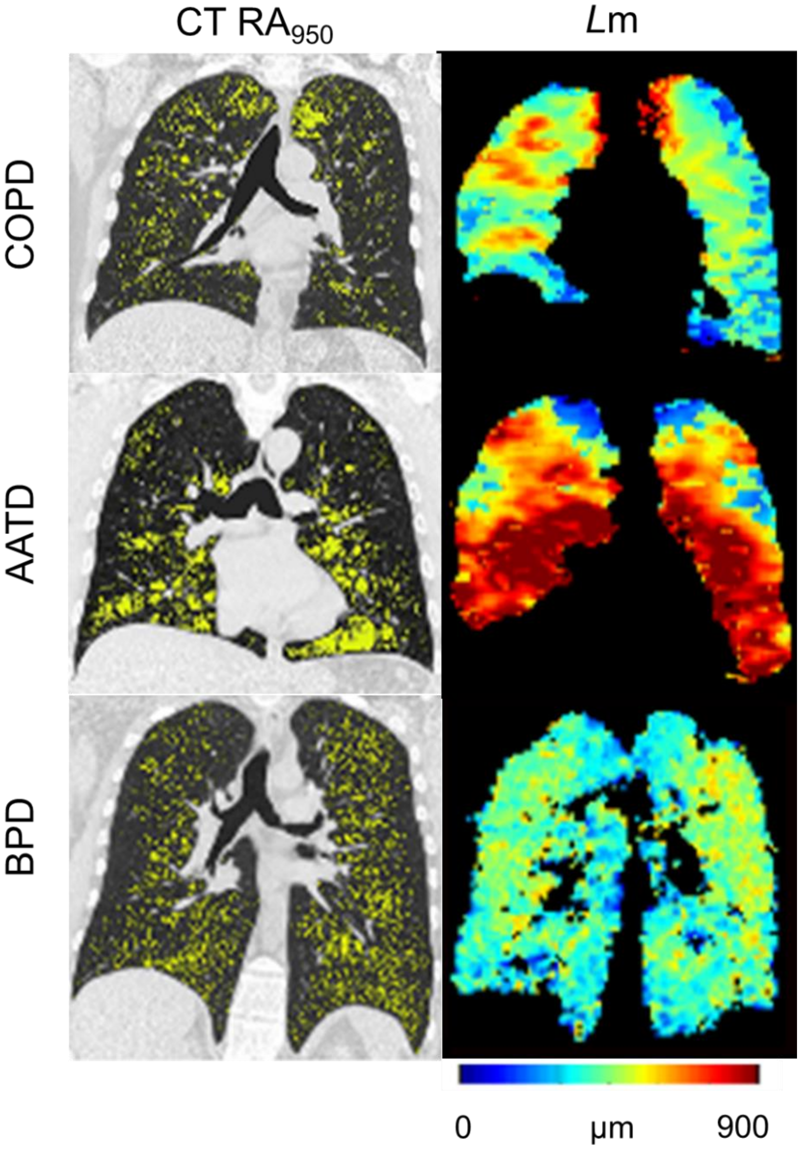

Yellow pixels on CT RA_{950} maps correspond to voxels < -950 Hounsfield Units.

Validation of MRI morphometry

All key preclinical and clinical findings using ^{3}He/^{129}Xe MRI are summarized in Table 2 which shows that MRI-derived lung morphometry has been directly compared with micro-

CT/histology-based estimates in small animal models. In Figure 4, the mean L_m for the COPD patient was 500 µm, significantly greater than the mean L_m estimate reported in elderly never-smokers,[96] which suggests that L_m can be used as emphysema biomarker and can be directly compared with histological values. In mouse studies, MRI-derived L_m values were in agreement with stereological measurements from lung histology and CT measurements.[91] A small animal model of mild emphysema was also investigated using ^{129}Xe MRI morphometry and histological measurements and a systematically increased L_m was reported.[93] In patient studies, L_m values were also shown to agree with stereological measurements.[85] Excellent correspondence between MRI based L_m estimates and the histology mean linear intercept estimates was confirmed.[70, 71] Although there has not been a direct comparison of ^{129}Xe morphology measurements to histology, there has recently been comparisons of ^{129}Xe to ^{3}He derived measures.[97]

Table 2: MRI-derived and Histology Mean Linear Intercept (L_m) values in small animal models and patients

	Mean Linear Intercept (L_m)			
	^{3}He MRI	**Histology**	**^{129}Xe MRI**	**Histology**
Clinical*:				
Normal lung	100 µm	105 µm	-	-
Normal lung	170 µm	140 µm	-	-
Mild emphysema	250 µm	240 µm	-	-
Mild emphysema	360 µm	360 µm	-	-
Severe emphysema	590 µm	590 µm	-	-
Severe emphysema	670 µm	660 µm	-	-
Small animal models:				
Healthy mice[a]	60±4 µm	52±2 µm	-	-
Sham mice[b]	66±5 µm	64±9 µm	-	-
Pneumonectomy mice[b]	68±3 µm	65±9 µm	-	-
Control rats[c]	-	-	79±12 µm	70±15 µm
Irradiated rats[c]	-	-	54±17 µm	57±12 µm
Healthy rats[d]	-	-	110±7 µm	80±7 µm
Emphysematous rats[d]	-	-	130±9 µm	100±4 µm

*Data from (85); [a]Data from (91) [b]Data from (67) [c]Data from (71) [d] Data from (93)

APPLICATIONS

Table 3 summarizes recent findings using MRI ADC and morphometry values in patients with COPD, BPD, lung cancer radiation-induced lung injury, post-surgical lung regrowth and lung transplant.

Table 3: Summary of MRI Morphometry Studies by Disease foci of interest

Application	Nuclei	Patient-based Study Literature References	Small-Animal Model Study Literature References
Volunteers	^{3}He	(103), (85), (97), (64), (90), (52), (93), (99), (97)	(93), (92)
	^{129}Xe	(65), (97), (129)	(126)
COPD	^{3}He	(13), (103), (85), (104), (84), (97)	
	^{129}Xe	(65), (97), (129)	(93)
AATD	^{3}He	(52), (99)	
BPD	^{3}He	(105)	
CF	^{129}Xe	(101)	
Lung Growth	^{3}He	(68)	(67)
RILI	^{3}He		(102)
	^{129}Xe		(71)

COPD

Figure 4 shows hyperpolarized ^{3}He MRI L_m maps and CT for patients with emphysema related to COPD and alpha-1 antitrypsin deficiency. The MRI-derived L_m map generated for the AATD subject shows two well-defined regions: 1) apical lung with normal L_m values and, 2) basal lung with abnormally large L_m values, suggesting severe emphysema ($L_m > 500$ µm). Thoracic CT density masks show good quantitative and spatial agreement with MRI regions with augmented L_m values. MRI morphometry has also clearly revealed emphysematous changes in current and ex-smokers,[64-66] congenital lobar emphysema,[98] normal lung aging,[96] as well as for evaluating emphysema in AATD patients[52, 99] and monitoring AATD patient response to augmentation therapy.[100] ^{129}Xe MRI morphometry has been piloted and compared in a small group of COPD patients and healthy volunteers[65] with mean MRI-derived L_m values in the range of 220-253 μm and 410 ± 90 μm, respectively.[101] Finally, hyperpolarized gas diffusion-weighted MRI has been clinically approved for use in the United Kingdom[56, 102-104] and this will dramatically increase the number of cases that can be used as exemplars of the utility of the method.

Bronchopulmonary Dysplasia (BPD)

Extreme prematurity at birth (<28 weeks gestation) commonly results in neonatal intensive care and mechanical ventilation due to respiratory distress syndrome because of limited or no lung surfactant and incomplete lung development. Ventilator-associated lung injury is also possible and extreme prematurity of the lung themselves cause abnormal and irregular lung growth (BPD). In neonates with a clinical diagnosis of BPD, monitoring of lung development throughout the course of the patient's life may guide the type and timing oftreatment, as well as provide insight into lung development in BPD. Hyperpolarized noble gas MRI morphometry has been used to observe the abnormal development of the acinar ducts as with BPD patients,[105] and was shown to be a promising method for longitudinal monitoring. Figure 4 provides an MRI-derived L_m map and CT with lung attenuation values <-950 HU shown in yellow for a patient with BPD. The heterogeneous MRI-derived L_m distribution is consistent with the heterogeneous distribution of the CT low-density areas. Importantly, this approach was previously validated using histology in clinical and small animal studies, as summarized in Table 2, providing credence and evidence of feasibility for the use of MRI morphometry in young patients with BPD in whom repeated CT imaging is not practical for radiation burden reasons.

Radiation-induced lung injury

Radiation-induced lung injury (RILI) remains a major dose-limiting factor for radiotherapy treatment of the lung cancer. Radiation pneumonitis or inflammation is commonly observed in patients at ~3 to 12 weeks post-irradiation due to cytokine induction and inflammation related to the radiation therapy. Late stage post-radiation pulmonary effects include parenchymal fibrosis and this typically develops 6 to 24 months post-radiation therapy and manifests as an irreversible decrease in lung compliance and decreased lung volume which are characteristic of a restrictive or fibrotic pulmonary phenotype. Both early and late post-radiation pulmonary effects have been well-investigated[106-108] but there remains an urgent need for new regional lung measurements of early post-radiation changes, in order to improve patient outcomes. A number of longitudinal clinical studies evaluated lung microstructure following radiotherapy treatment.[109-114] These studies have reported differences in ADC values in patients with RILI compared to controls, along with ^{3}He static lung ventilation defects. RILI-induced fibrosis in rats showed[102] that ADC values in regions of fibrosis were lower compared to healthy regions. The earliest stages of radiation-pneumonitis and RILI was also investigated using ^{129}Xe MRI morphometry in rats. This work revealed quantitative morphological changes at the alveolar level as early as two weeks post-radiation[71] while MRI-based L_m, estimates were consistent with L_m changes measured using histology in rats sacrificed at the end of the study.

Adult Lung Regrowth

One potential clinical application of MRI morphometry is the evaluation and characterization of lung growth in newborns and children as well as in adults, post-surgery. The observation and assessment of lung regrowth in adults[68] and in small animal models[67] demonstrated this clinical potential for cases where MRI is a good alternative for non-invasive assessment of lung structure and function. In the new field of cell-based replacement therapies and whole organ regeneration,[115, 116] non-invasive MRI morphometry provides a non-invasive way to serially measure lung growth as well as the biomechanical and functional properties. For example, ^{3}He MRI morphometry was recently used to track lung growth over 30 days using MRI L_m estimates and changes in the alveolar density.[67]

Lung Transplant

Bronchiolitis obliterans syndrome (BOS), or obstructive chronic lung allograft dysfunction (CLAD), is loss of lung function due to airway remodeling and fibrosis following lung transplantation.[117] Clinically, BOS is characterized using measurements of gas-trapping, bronchiectasis and hyperinflation and thoracic CT follow-up is commonly employed post-transplantation to monitor lung structural changes. More than 10 years ago, hyperpolarized

^{3}He MRI was piloted in post-transplant patients to detect and measure ventilation defects due to BOS.[118, 119] While MRI morphometry has not yet been piloted in these patients, it will certainly provide a sensitive, non-invasive means of measuring changes in the lung parenchyma and perhaps early warnings of BOS in post-transplant patients.

CHALLENGES AND LIMITATIONS

A summary of the challenges, limitations and strengths associated with ^{3}He and ^{129}Xe lung morphometry MRI are briefly outlined in Table 4. Some of the limitations of hyperpolarized noble gas MRI relate mainly to infrastructure availability and the complexity of the analysis that has limited its use at major clinical centers. While ^{3}He availability and cost is also a limitation,[120] as an alternative, ^{129}Xe gas provides both availability and cost effectiveness[121, 122] while enabling imaging measurements that are similar to and perhaps more sensitive to airway obstruction than ^{3}He.[55, 63, 123, 124] As well, ^{129}Xe is modestly soluble in biological tissues and blood, which permits simultaneous ventilation-perfusion and blood-gas tissue barrier imaging.[125, 126] However, ^{129}Xe MRI whole lung three-dimensional morphometry is still very challenging[88, 127] and this has led to the development of rapid image acquisition and reconstruction techniques as well as advanced transmit-receive MRI hardware.[127, 128] Recently, the feasibility of single breath-hold, whole lung morphometry with hyperpolarized ^{3}He using parallel imaging was demonstrated[127] in four asthma patients with a reduction in total acquisition time of up to 10 seconds; morphometric estimates with and without parallel imaging demonstrated good agreement. Another single breath-hold ^{3}He/^{129}X whole lung morphometry approach using compressed sensing with an acceleration factor similar to parallel imaging was demonstrated in healthy volunteers and COPD patients.[88, 97] Recently, a compressed sensing approach[90] was developed that combined undersampling in both spatial and diffusion-sensitizing directions; this work underscores the role of continuous optimization of compressed sensing and parallel imaging to reduce acquisition times which may help increase clinical uptake.

Table 4: Challenges, Limitations and Opportunities

	^{3}He MRI	**^{129}Xe MRI**
Challenges	High cost, limited supply No pathway for clinical translation No pathway for commercial translation	Low gamma = lower SNR than ^{3}He MRI Slower lung filling and gas diffusion Advanced MRI hardware such as high gradient strength and receive phase arrays needed
Limitations	Cannot be mixed with oxygen or used for free breathing measurements in patients Inert, not soluble in lung tissue and blood	Cannot be mixed with oxygen or used for dynamic free-breathing patient measurements Pulse sequences result in mechanical vibrations leading to acoustic effects
Opportunities	High image SNR Fast lung filling	Natural abundance of ^{129}Xe isotope Large volume, high polarization, rapid production ^{129}Xe polarizers Solubility in tissue and blood allows for pulmonary gas, barrier, blood imaging and brain measurements. Approved for clinical use UK

ROLE IN FUTURE

Patients with chronic lung disease typically require treatment and monitoring over decades as disease progression, lung maturation and aging ensues. Frequent, or at least annual clinical evaluations are required to assess progressive disease, response to therapy and the need for changes in therapy and other clinical management strategies. Until now however, and in a few specific cases, thoracic imaging is not routinely used in the clinical work-up or follow-up of patients with chronic lung disease. The application of MRI morphometry methods and measurements in patients with COPD,[51, 64, 65, 85, 96, 97, 103, 104, 129] cystic fibrosis,[101] BPD[105] and AATD [52, 99] has well-demonstrated its clinical potential and opens the door for more personalized and perhaps augmented therapy for these patients. For example, in AATD patients, including those undergoing augmentation therapy or cell-based therapy, there is a potential clinical benefit because response to therapy can be measured using MRI-derived L_m. Moreover, preclinical studies have demonstrated the promising impact of stem cell-based therapies in small animal models mimicking BPD.[130, 131] The evidence of alveolar growth and repair observed in the small animal models is now driving early phase clinical trials for which MRI lung morphometry is an ideal efficacy and safety measurement tool. Furthermore, the direct phenotyping of AATD, BPD and CF patients with MRI-derived lung morphometry measurements holds promise for clinical decision making in regard to lung transplant. Certainly, MRI-derived morphometry measurements are highly complementary to current clinical consensus guideline measurement thresh-holds used to stratify patients to the transplant list.

Further development of MRI hardware including multiple receive array coils[132] and increasing clinical scanner gradient strength, as well as parallel imaging[127] and compressed sensing,[88] will improve image quality and signal-to-noise ratios as well as decrease the data acquisition time. This will provide a way to combine isotropic ventilation and diffusion-weighting in a single breath-hold whole lung measurement. Another important step that will enhance clinical utilization of ^{129}Xe MRI morphometry measurements is the facilitation of new clinical research sites at pediatric hospitals including Cincinnati Children's Hospital (Cincinnati USA) and the Hospital for Sick Children (Toronto CANADA).

In summary, following the pivotal *ex vivo* studies of Leopold and Gough[7] and Weibel and co-workers [8], hyperpolarized noble gas MRI provides new, non-invasive *in vivo* measurements of the lung parenchyma that have been validated using histology. In future, new ^{129}Xe MRI methods will be developed to generate regional maps and biomarkers of alveolar wall microstructure because ^{129}Xe has modest solubility in the tissue barrier for gas diffusion and in the blood.[125, 133, 134] This technological advance will certainly accelerate *in vivo* longitudinal monitoring of lung biomarkers[135] that have never before been possible in patients.

REFERENCES

1. Spriggs EA. John Hutchinson, the inventor of the spirometer--hisnorthcountrybackground, life in London, and scientific achievements. Med Hist. 1977;21(4):357-64. Epub 1977/10/01.
2. Hogg JC, Macklem PT, Thurlbeck WM. Site and nature of airway obstruction in chronic obstructive lung disease. N Engl J Med. 1968;278(25):1355-60.
3. McDonough JE, Yuan R, Suzuki M, et al. Small-airway obstruction and emphysema in chronic obstructive pulmonary disease. N Engl J Med. 2011;365(17):1567-75.
4. Drummond MB, Schwartz PF, Duggan WT, et al. Intersession variability in single-breath diffusing capacity in diabetics without overt lung disease. Am J Respir Crit Care Med. 2008;178(3):225-32.
5. Schluchter MD, Stoller JK, Barker AF, et al. Feasibility of a clinical trial of augmentation therapy for alpha(1)-antitrypsin deficiency. The Alpha 1-Antitrypsin Deficiency Registry Study Group. Am J Respir Crit Care Med. 2000;161(3 Pt 1):796-801.
6. Lynch DA, Austin JH, Hogg JC, et al. CT-Definable Subtypes of Chronic Obstructive Pulmonary Disease: A Statement of the Fleischner Society. Radiology. 2015;277(1):192-205.
7. Leopold JG, Gough J. The centrilobular form of hypertrophic emphysema and its relation to chronic bronchitis. Thorax. 1957;12(3):219-35.
8. Weibel ER. Principles and methods for the morphometric study of the lung and other organs. Lab Invest. 1963;12:131-55.
9. Ochs M, Nyengaard JR, Jung A, et al. The number of alveoli in the human lung. Am J Respir Crit Care Med. 2004;169(1):120-4.
10. Ochs M. A brief update on lung stereology. J Microsc. 2006;222(3):188-200.
11. Ochs M, Mühlfeld C. Quantitative microscopy of the lung: a problem-based approach. Part 1: basic principles of lung stereology. American Journal of Physiology-Lung Cellular and Molecular Physiology. 2013;305(1):L15-L22.
12. Heemskerk-Gerritsen BA, Dijkman JH, Ten Have-Opbroek AA. Stereological methods: a new approach in the assessment of pulmonary emphysema. Microsc Res Tech. 1996;34(6):556-62.
13. Wiebe BM, Laursen H. Lung morphometry by unbiased methods in emphysema: bronchial and blood vessel volume, alveolar surface area and capillary length. APMIS. 1998;106(6):651-6.
14. Massaro GD, Massaro D. Formation of pulmonary alveoli and gas-exchange surface area: quantitation and regulation. Annu Rev Physiol. 1996;58:73-92.
15. Elliott JC, Dover SD. X-ray microtomography. J Microsc. 1982;126(Pt 2):211-3.
16. Kujoory MA, Hillman BJ, Barrett HH. High-resolution computed tomography of the normal rat nephrogram. Invest Radiol. 1980;15(2):148-54.
17. Sato T, Ikeda O, Yamakoshi Y, Tsubouchi M. X-ray tomography for microstructural objects. Appl Opt. 1981;20(22):3880-3.
18. Holdsworth DW, Drangova M, Fenster A. A high-resolution XRII-based quantitative volume CT scanner. Med Phys. 1993;20(2 Pt 1):449-62. Epub 1993/03/01.

19. Drangova M, Holdsworth DW, Boyd CJ, Dunmore PJ, Roach MR, Fenster A. Elasticity and geometry measurements of vascular specimens using a high-resolution laboratory CT scanner. Physiol Meas. 1993;14(3):277-90. Epub 1993/08/01.
20. Litzlbauer HD, Korbel K, Kline TL, et al. Synchrotron-Based Micro-CT Imaging of the Human Lung Acinus. Anat Rec. 2010;293(9):1607-14.
21. Parameswaran H, Bartolák-Suki E, Hamakawa H, Majumdar A, Allen PG, Suki B. Three-dimensional measurement of alveolar airspace volumes in normal and emphysematous lungs using micro-CT. J Appl Physiol. 2009;107(2):583-92.
22. Akhavan Sharif MR, Lam WW, Ouriadov AV, Holdsworth DW, Santyr GE. Comparison of hyperpolarized (3)He MRI rat lung volume measurement with micro-computed tomography. NMR Biomed. 2010;23(4):359-67.
23. Lam WW, Holdsworth DW, Du LY, Drangova M, McCormack DG, Santyr GE. Micro-CT imaging of rat lung ventilation using continuous image acquisition during xenon gas contrast enhancement. J Appl Physiol. 2007;103(5):1848-56.
24. Ford NL, Martin EL, Lewis JF, Veldhuizen RA, Drangova M, Holdsworth DW. In vivo characterization of lung morphology and function in anesthetized free-breathing mice using micro-computed tomography. J Appl Physiol (1985). 2007;102(5):2046-55. Epub 2007/01/27.
25. Ford NL, Nikolov HN, Norley CJ, et al. Prospective respiratory-gated micro-CT of free breathing rodents. Med Phys. 2005;32(9):2888-98. Epub 2005/11/04.
26. Litzlbauer HD, Neuhaeuser C, Moell A, et al. Three-dimensional imaging and morphometric analysis of alveolar tissue from microfocal X-ray-computed tomography. American Journal of Physiology-Lung Cellular and Molecular Physiology. 2006;291(3):L535-L45.
27. Watz H, Breithecker A, Rau WS, Kriete A. Micro-CT of the Human Lung: Imaging of Alveoli and Virtual Endoscopy of an Alveolar Duct in a Normal Lung and in a Lung with Centrilobular Emphysema—Initial Observations 1. Radiology. 2005;236(3):1053-8.
28. Tanabe N, Vasilescu DM, McDonough JE, et al. MicroCT Comparison of Preterminal Bronchioles in Centrilobular and Panlobular Emphysema. Am J Respir Crit Care Med. 2016(ja).
29. Holdsworth DW, Thornton MM. Micro-CT in small animal and specimen imaging. Trends in Biotechnology. 2002;20(8):S34-S9.
30. Ritman EL. Micro-computed tomography of the lungs and pulmonary-vascular system. Proceedings of the American Thoracic Society. 2005;2(6):477-80.
31. Hsia CC, Hyde DM, Ochs M, Weibel ER. An official research policy statement of the American Thoracic Society/European Respiratory Society: standards for quantitative assessment of lung structure. Am J Respir Crit Care Med. 2010;181(4):394-418.
32. Jost RG, Sagel SS, Stanley RJ, Levitt RG. Computed tomography of the thorax. Radiology. 1978;126(1):125-36.
33. Rosenblum LJ, Mauceri RA, Wellenstein DE, Bassano DA, Cohen WN, Heitzman ER. Computed tomography of the lung. Radiology. 1978;129(2):521-4.
34. Goddard PR, Nicholson EM, Laszlo G, Watt I. Computed tomography in pulmonary emphysema. Clin Radiol. 1982;33(4):379-87.
35. Bergin C, Muller N, Nichols DM, et al. The diagnosis of emphysema. A computed tomographic-pathologic correlation. Am Rev Respir Dis. 1986;133(4):541-6.

36. Foster WL, Jr., Pratt PC, Roggli VL, Godwin JD, Halvorsen RA, Jr., Putman CE. Centrilobular emphysema: CT-pathologic correlation. Radiology. 1986;159(1):27-32.
37. Webb WR, Stein MG, Finkbeiner WE, Im JG, Lynch D, Gamsu G. Normal and diseased isolated lungs: high-resolution CT. Radiology. 1988;166(1 Pt 1):81-7.
38. Lynch DA, Brasch RC, Hardy KA, Webb WR. Pediatric pulmonary disease: assessment with high-resolution ultrafast CT. Radiology. 1990;176(1):243-8.
39. Lynch DA. Imaging of small airways diseases. Clin Chest Med. 1993;14(4):623-34. Epub 1993/12/01.
40. Hirose N, Lynch DA, Cherniack RM, Doherty DE. Correlation between high resolution computed tomography and tissue morphometry of the lung in bleomycin-induced pulmonary fibrosis in the rabbit. Am Rev Respir Dis. 1993;147(3):730-8. Epub 1993/03/01.
41. Heussel CP, Herth FJ, Kappes J, et al. Fully automatic quantitative assessment of emphysema in computed tomography: comparison with pulmonary function testing and normal values. Eur Radiol. 2009;19(10):2391-402.
42. Stolk J, Dirksen A, van der Lugt AA, et al. Repeatability of lung density measurements with low-dose computed tomography in subjects with alpha-1-antitrypsin deficiency-associated emphysema. Invest Radiol. 2001;36(11):648-51.
43. Mishima M, Hirai T, Itoh H, et al. Complexity of terminal airspace geometry assessed by lung computed tomography in normal subjects and patients with chronic obstructive pulmonary disease. Proc Natl Acad Sci U S A. 1999;96(16):8829-34.
44. Coxson HO, Rogers RM, Whittall KP, et al. A quantification of the lung surface area in emphysema using computed tomography. Am J Respir Crit Care Med. 1999;159(3):851-6.
45. Albert MS, Cates GD, Driehuys B, et al. Biological magnetic resonance imaging using laser-polarized 129Xe. Nature. 1994;370(6486):199-201.
46. Chen XJ, Hedlund LW, Moller HE, Chawla MS, Maronpot RR, Johnson GA. Detection of emphysema in rat lungs by using magnetic resonance measurements of 3He diffusion. Proc Natl Acad Sci U S A. 2000;97(21):11478-81.
47. Saam BT, Yablonskiy DA, Kodibagkar VD, et al. MR imaging of diffusion of 3He gas in healthy and diseased lungs. Magn Reson Med. 2000;44(2):174-9.
48. Parraga G, Ouriadov A, Evans A, et al. Hyperpolarized 3He ventilation defects and apparent diffusion coefficients in chronic obstructive pulmonary disease: preliminary results at 3.0 Tesla. Invest Radiol. 2007;42(6):384-91.
49. Kauczor HU, Ebert M, Kreitner KF, et al. Imaging of the lungs using 3He MRI: preliminary clinical experience in 18 patients with and without lung disease. J Magn Reson Imaging. 1997;7(3):538-43.
50. Kaushik SS, Cleveland ZI, Cofer GP, et al. Diffusion-weighted hyperpolarized 129Xe MRI in healthy volunteers and subjects with chronic obstructive pulmonary disease. Magn Reson Med. 2011;65(4):1154-65.
51. Yablonskiy DA, Sukstanskii AL, Leawoods JC, et al. Quantitative in vivo assessment of lung microstructure at the alveolar level with hyperpolarized 3He diffusion MRI. Proc Natl Acad Sci U S A. 2002;99(5):3111-6.
52. Ouriadov A, Lessard E, Sheikh K, Parraga G, for the Canadian Respiratory Research N. Pulmonary MRI morphometry modeling of airspace enlargement in chronic

obstructive pulmonary disease and alpha-1 antitrypsin deficiency. Magn Reson Med. 2017.
53. Morbach AE, Gast KK, Schmiedeskamp J, et al. Diffusion-weighted MRI of the lung with hyperpolarized helium-3: a study of reproducibility. J Magn Reson Imaging. 2005;21(6):765-74.
54. Diaz S, Casselbrant I, Piitulainen E, et al. Validity of apparent diffusion coefficient hyperpolarized 3He-MRI using MSCT and pulmonary function tests as references. Eur J Radiol. 2009;71(2):257-63.
55. Kirby M, Ouriadov A, Svenningsen S, et al. Hyperpolarized 3He and 129Xe magnetic resonance imaging apparent diffusion coefficients: physiological relevance in older never- and ex-smokers. Physiol Rep. 2014;2(7).
56. Chen XJ, Möller HE, Chawla MS, et al. Spatially resolved measurements of hyperpolarized gas properties in the lung in vivo. Part I: Diffusion coefficient. Magn Reson Med. 1999;42(4):721-8.
57. Salerno M, Lange EEd, Altes TA, Truwit JD, Brookeman JR, John P. Mugler I. Emphysema: Hyperpolarized Helium 3 Diffusion MR Imaging of the Lungs Compared with Spirometric Indexes—Initial Experience. Radiology. 2002;222(1):252-60.
58. Tanoli TS, Woods JC, Conradi MS, et al. In vivo lung morphometry with hyperpolarized 3He diffusion MRI in canines with induced emphysema: disease progression and comparison with computed tomography. J Appl Physiol (1985). 2007;102(1):477-84.
59. Swift AJ, Wild JM, Fichele S, et al. Emphysematous changes and normal variation in smokers and COPD patients using diffusion 3He MRI. Eur J Radiol. 2005;54(3):352-8.
60. Fain SB, Panth SR, Evans MD, et al. Early Emphysematous Changes in Asymptomatic Smokers: Detection with 3He MR Imaging. Radiology. 2006;239(3):875-83.
61. Woods JC, Yablonskiy DA, Choong CK, et al. Long-range diffusion of hyperpolarized 3He in explanted normal and emphysematous human lungs via magnetization tagging. J Appl Physiol (1985). 2005;99(5):1992-7.
62. Diaz S, Casselbrant I, Piitulainen E, et al. Hyperpolarized 3He apparent diffusion coefficient MRI of the lung: reproducibility and volume dependency in healthy volunteers and patients with emphysema. J Magn Reson Imaging. 2008;27(4):763-70.
63. Kirby M, Svenningsen S, Owrangi A, et al. Hyperpolarized 3He and 129Xe MR Imaging in Healthy Volunteers and Patients with Chronic Obstructive Pulmonary Disease. Radiology. 2012;265(2):600-10.
64. Quirk JD, Chang YV, Yablonskiy DA. In vivo lung morphometry with hyperpolarized (3) He diffusion MRI: reproducibility and the role of diffusion-sensitizing gradient direction. Magn Reson Med. 2015;73(3):1252-7.
65. Ouriadov A, Farag A, Kirby M, McCormack DG, Parraga G, Santyr GE. Lung morphometry using hyperpolarized (129) Xe apparent diffusion coefficient anisotropy in chronic obstructive pulmonary disease. Magn Reson Med. 2013;70(6):1699-706.
66. Ouriadov A, Farag A, Kirby M, McCormack DG, Parraga G, Santyr GE. Pulmonary hyperpolarized Xe morphometry for mapping xenon gas concentrations and alveolar oxygen partial pressure: Proof-of-concept demonstration in healthy and COPD subjects. Magn Reson Med. 2014.

67. Wang W, Nguyen NM, Guo J, Woods JC. Longitudinal, noninvasive monitoring of compensatory lung growth in mice after pneumonectomy via (3)He and (1)H magnetic resonance imaging. Am J Respir Cell Mol Biol. 2013;49(5):697-703.
68. Butler JP, Loring SH, Patz S, Tsuda A, Yablonskiy DA, Mentzer SJ. Evidence for adult lung growth in humans. N Engl J Med. 2012;367(3):244-7.
69. Kirby M, McCormack DG, Parraga G. Evidence of adult lung growth in humans. N Engl J Med. 2012;367(16):1566-7.
70. Yablonskiy DA, Sukstanskii AL, Conradi MS. Commentary on "The influence of lung airways branching structure and diffusion time on measurements and models of short-range 3He gas MR diffusion". J Magn Reson. 2014;239:139-42.
71. Ouriadov A, Fox M, Hegarty E, Parraga G, Wong E, Santyr GE. Early stage radiation-induced lung injury detected using hyperpolarized (129) Xe Morphometry: Proof-of-concept demonstration in a rat model. Magn Reson Med. 2015;75(6):2421-31.
72. Fain S, Schiebler ML, McCormack DG, Parraga G. Imaging of lung function using hyperpolarized helium-3 magnetic resonance imaging: Review of current and emerging translational methods and applications. J Magn Reson Imaging. 2010;32(6):1398-408.
73. Fain SB, Korosec FR, Holmes JH, O'Halloran R, Sorkness RL, Grist TM. Functional lung imaging using hyperpolarized gas MRI. J Magn Reson Imaging. 2007;25(5):910-23.
74. Mugler JP, 3rd, Altes TA. Hyperpolarized 129Xe MRI of the human lung. J Magn Reson Imaging. 2013;37(2):313-31.
75. Callaghan PT. Pulsed-Gradient Spin-Echo Nmr for Planar, Cylindrical, and Spherical Pores under Conditions of Wall Relaxation. Journal of Magnetic Resonance Series A. 1995;113(1):53-9.
76. Weibel E. Geometry and Dimensions of Airways of Conductive and Transitory Zones. Morphometry of the Human Lung: Springer Berlin Heidelberg; 1963. p. 110-35.
77. Gallegos DP, Smith DM, Brinker CJ. An NMR technique for the analysis of pore structure: Application to mesopores and micropores. Journal of Colloid and Interface Science. 1988;124(1):186-98.
78. Coy A, Callaghan PT. Pulsed Gradient Spin-Echo NMR "Diffusive Diffraction" Experiments on Water Surrounding Close-Packed Polymer Spheres. Journal of Colloid and Interface Science. 1994;168(2):373-9.
79. Blair SC, Berge PA, Berryman JG. Using two-point correlation functions to characterize microgeometry and estimate permeabilities of sandstones and porous glass. Journal of Geophysical Research: Solid Earth. 1996;101(B9):20359-75.
80. Kukla V, Kornatowski J, Demuth D, et al. NMR Studies of Single-File Diffusion in Unidimensional Channel Zeolites. Science. 1996;272(5262):702-4.
81. Mitra PP, Sen PN, Schwartz LM, Le Doussal P. Diffusion propagator as a probe of the structure of porous media. Phys Rev Lett. 1992;68(24):3555-8.
82. Mitra PP, Sen PN, Schwartz LM. Short-Time Behavior of the Diffusion-Coefficient as a Geometrical Probe of Porous-Media. Phys Rev B. 1993;47(14):8565-74.
83. Woods JC, Yablonskiy DA, Chino K, Tanoli TS, Cooper JD, Conradi MS. Magnetization tagging decay to measure long-range (3)He diffusion in healthy and emphysematous canine lungs. Magn ResonMed. 2004;51(5):1002-8.

84. Quirk JD, Lutey BA, Gierada DS, et al. In vivo detection of acinar microstructural changes in early emphysema with 3He lung morphometry. Radiology. 2011;260(3):866-74.
85. Yablonskiy DA, Sukstanskii AL, Woods JC, et al. Quantification of lung microstructure with hyperpolarized 3He diffusion MRI. J Appl Physiol. 2009;107(4):1258-65.
86. Sukstanskii AL, Yablonskiy DA. In vivo lung morphometry with hyperpolarized 3He diffusion MRI: theoretical background. J Magn Reson. 2008;190(2):200-10.
87. Berberan-Santos MN, Bodunov EN, Valeur B. Mathematical functions for the analysis of luminescence decays with underlying distributions 1. Kohlrausch decay function (stretched exponential). Chem Phys. 2005;315(1-2):171-82.
88. Chan HF, Stewart NJ, Parra-Robles J, Collier GJ, Wild JM. Whole lung morphometry with 3D multiple b-value hyperpolarized gas MRI and compressed sensing. Magn Reson Med. 2016.
89. Chan H-F, Stewart N, Parra-Robles J, Collier G, Wild JM. 3D Mapping of Whole Lung Morphometry with 129Xe Diffusion-Weighted MRI and Compressed Sensing: Comparison with 3He. ISMRM 25th Annual Meeting, Honolulu, Hawaii, USA. 2017([abstract]):2138.
90. Abascal JFPJ, Desco M, Parra-Robles J. Incorporation of prior knowledge of the signal behavior into the reconstruction to accelerate the acquisition of MR diffusion data. ArXiv e-prints [Internet]. 2017; 1702. Available from: http://adsabs.harvard.edu/abs/2017arXiv170202743A.
91. Wang W, Nguyen NM, Yablonskiy DA, et al. Imaging lung microstructure in mice with hyperpolarized 3He diffusion MRI. Magn Reson Med. 2011;65(3):620-6.
92. Osmanagic E, Sukstanskii AL, Quirk JD, et al. Quantitative assessment of lung microstructure in healthy mice using an MR-based 3He lung morphometry technique. J Appl Physiol (1985). 2010;109(6):1592-9.
93. Ruan W, Zhong J, Wang K, et al. Detection of the mild emphysema by quantification of lung respiratory airways with hyperpolarized xenon diffusion MRI. J Magn Reson Imaging. 2016.
94. Sukstanskii AL, Yablonskiy DA. Lung morphometry with hyperpolarized 129Xe: theoretical background. Magn Reson Med. 2012;67(3):856-66.
95. Yablonskiy DA, Sukstanskii AL. Chapter 12 - Lung Morphometry With HP Gas Diffusion MRI: From Theoretical Models to Experimental Measurements. In: Hane FT, editor. Hyperpolarized and Inert Gas MRI. Boston: Academic Press; 2017. p. 183-209.
96. Paulin GA, Ouriadov A, Lessard E, Sheikh K, McCormack DG, Parraga G. Noninvasive quantification of alveolar morphometry in elderly never- and ex-smokers. Physiol Rep. 2015;3(10).
97. Chan HF, Stewart NJ, Norquay G, Collier GJ, Wild JM. 3D diffusion-weighted 129 Xe MRI for whole lung morphometry. Magn Reson Med. 2017:n/a-n/a.
98. Pike D, Mohan S, Ma W, Lewis JF, Parraga G. Pulmonary imaging abnormalities in an adult case of congenital lobar emphysema. J Radiol Case Rep. 2015;9(2):9-15.
99. Lessard E, Young HM, Bhalla A, et al. Pulmonary 3He Magnetic Resonance Imaging Biomarkers of Regional Airspace Enlargement in Alpha-1 Antitrypsin Deficiency. Acad Radiol. 2017.

100. Lessard E, Ouriadov A, Pike D, McCormack DG, Parraga G. Longitudinal Three-Year Decline in Alpha-1 Antitrypsin Deficiency: Regional Worsening in Emphysema and Ventilation. American Thoracic Society Annual Scientific Meeting. 2016:A3141.
101. Ruppert K, Quirk JD, Mugler JPI, et al. Lung Morphometry using Hyperpolarized Xenon-129: Preliminary Experience [abstract]. ISMRM 20th Annual Meeting, Melbourne, Australia. 2012:1352.
102. Ward ER, Hedlund LW, Kurylo WC, et al. Proton and hyperpolarized helium magnetic resonance imaging of radiation-induced lung injury in rats. Int J Radiat Oncol Biol Phys. 2004;58(5):1562-9.
103. Woods JC, Choong CK, Yablonskiy DA, et al. Hyperpolarized 3He diffusion MRI and histology in pulmonary emphysema. Magn Reson Med. 2006;56(6):1293-300.
104. Thomen RP, Quirk JD, Roach D, et al. Direct comparison of 129 Xe diffusion measurements with quantitative histology in human lungs. Magn Reson Med. 2016.
105. Sheikh K, Bhalla A, Ouriadov A, et al. Pulmonary magnetic resonance imaging biomarkers of lung structure and function in adult survivors of bronchopulmonary dysplasia with COPD. Cogent Medicine. 2017;4(1):1282033.
106. Gross NJ. The pathogenesis of radiation-induced lung damage. Lung. 1981;159(3):115-25.
107. Hill RP. Radiation effects on the respiratory system. The British Journal of Radiology. 2005;Supplement_27(1):75-81.
108. Bentzen SM. Preventing or reducing late side effects of radiation therapy: radiobiology meets molecular pathology. Nat Rev Cancer. 2006;6(9):702-13.
109. Mathew L, Gaede S, Wheatley A, Etemad-Rezai R, Rodrigues GB, Parraga G. Detection of longitudinal lung structural and functional changes after diagnosis of radiation-induced lung injury using hyperpolarized 3He magnetic resonance imaging. Med Phys. 2010;37(1):22-31.
110. Ireland RH, Din OS, Swinscoe JA, et al. Detection of radiation-induced lung injury in non-small cell lung cancer patients using hyperpolarized helium-3 magnetic resonance imaging. Radiother Oncol. 2010;97(2):244-8.
111. Hodge CW, Tome WA, Fain SB, Bentzen SM, Mehta MP. On the use of hyperpolarized helium MRI for conformal avoidance lung radiotherapy. Med Dosim. 2010;35(4):297-303.
112. Mathew L, Wheatley A, Castillo R, et al. Hyperpolarized (3)He magnetic resonance imaging: comparison with four-dimensional x-ray computed tomography imaging in lung cancer. Acad Radiol. 2012;19(12):1546-53.
113. Ireland RH, Bragg CM, McJury M, et al. Feasibility of image registration and intensity-modulated radiotherapy planning with hyperpolarized helium-3 magnetic resonance imaging for non-small-cell lung cancer. Int J Radiat Oncol Biol Phys. 2007;68(1):273-81.
114. Mathew L, Vandyk J, Etemad-Rezai R, Rodrigues G, Parraga G. Hyperpolarized (3)He pulmonary functional magnetic resonance imaging prior to radiation therapy. Med Phys. 2012;39(7):4284-90.
115. Kotton DN, Morrisey EE. Lung regeneration: mechanisms, applications and emerging stem cell populations. Nat Med. 2014;20(8):822-32.
116. Nichols JE, La Francesca S, Niles JA, et al. Production and transplantation of bioengineered lung into a large-animal model. Sci Transl Med. 2018;10(452).

117. Meyer KC, Raghu G, Verleden GM, et al. An international ISHLT/ATS/ERS clinical practice guideline: diagnosis and management of bronchiolitis obliterans syndrome. Eur Respir J. 2014;44(6):1479-503.
118. Gast KK, Zaporozhan J, Ley S, et al. 3He-MRI in follow-up of lung transplant recipients. Eur Radiol. 2004;14(1):78-85.
119. Gast KK, Viallon M, Eberle B, et al. MRI in lung transplant recipients using hyperpolarized 3He: comparison with CT. J Magn Reson. 2002;15(3):268-74.
120. Shea DA, Morgan D. The Helium-3 Shortage: Supply, Demand, and Options for Congress. Technical Report R41419. 2010.
121. Stewart NJ, Norquay G, Marshall H, Wild JM. Feasibility of high quality lung MRI with naturally-abundant hyperpolarised 129Xe. Eur Respir J. 2014;44(Suppl 58).
122. Stewart NJ, Norquay G, Griffiths PD, Wild JM. Feasibility of human lung ventilation imaging using highly polarized naturally abundant xenon and optimized three-dimensional steady-state free precession. Magn Reson Med. 2015;74(2):346-52.
123. Stewart N, Chan H-F, Hughes P, et al. Comparison of 3He and 129Xe MRI for evaluation of lung microstructure and ventilation at 1.5 T. Eur Respir J. 2016;48(suppl 60).
124. Svenningsen S, Kirby M, Starr D, et al. Hyperpolarized (3) He and (129) Xe MRI: differences in asthma before bronchodilation. J Magn Reson Imaging. 2013;38(6):1521-30.
125. Driehuys B, Möller HE, Cleveland ZI, Pollaro J, Hedlund LW. Pulmonary Perfusion and Xenon Gas Exchange in Rats: MR Imaging with Intravenous Injection of Hyperpolarized (129)Xe. Radiology. 2009;252(2):386-93.
126. Zhong J, Zhang H, Ruan W, et al. Simultaneous assessment of both lung morphometry and gas exchange function within a single breath-hold by hyperpolarized (129) Xe MRI. NMR Biomed. 2017;30(8).
127. Chang YV, Quirk JD, Yablonskiy DA. In vivo lung morphometry with accelerated hyperpolarized (3) He diffusion MRI: a preliminary study. Magn Reson Med. 2015;73(4):1609-14.
128. Deppe MH, Parra-Robles J, Marshall H, Lanz T, Wild JM. A flexible 32-channel receive array combined with a homogeneous transmit coil for human lung imaging with hyperpolarized 3He at 1.5 T. Magn Reson Med. 2011;66(6):1788-97.
129. Zhang H, Xie J, Xiao S, et al. Lung morphometry using hyperpolarized (129) Xe multi-b diffusion MRI with compressed sensing in healthy subjects and patients with COPD. Med Phys. 2018;45(7):3097-108.
130. Alphonse RS, Vadivel A, Fung M, et al. Existence, Functional Impairment, and Lung Repair Potential of Endothelial Colony-Forming Cells in Oxygen-Induced Arrested Alveolar Growth. Circulation. 2014;129(21):2144-57.
131. Balasubramaniam V, Ryan SL, Seedorf GJ, et al. Bone marrow-derived angiogenic cells restore lung alveolar and vascular structure after neonatal hyperoxia in infant mice. American Journal of Physiology - Lung Cellular and Molecular Physiology. 2010;298(3):L315-L23.
132. Charles C, Jones2 RW, Halaweish AF, Ainslie MD. Parallel Imaging for Short Breath Hold Times in Perfluorinated Gas Imaging of the Lung [abstract]. ISMRM 23rd Annual Meeting. 2015:3984.

133. Mugler JP, 3rd, Driehuys B, Brookeman JR, et al. MR imaging and spectroscopy using hyperpolarized 129Xe gas: preliminary human results. Magn Reson Med. 1997;37(6):809-15.

134. Cleveland ZI, Cofer GP, Metz G, et al. Hyperpolarized Xe MR imaging of alveolar gas uptake in humans. PLoS One. 2010;5(8):e12192.

135. Kaushik SS, Robertson SH, Freeman MS, et al. Single-breath clinical imaging of hyperpolarized (129)Xe in the airspaces, barrier, and red blood cells using an interleaved 3D radial 1-point Dixon acquisition. Magn Reson Med. 2016;75(4):1434-43.

Appendix D – Health Science Research Ethics Board Approval Notices

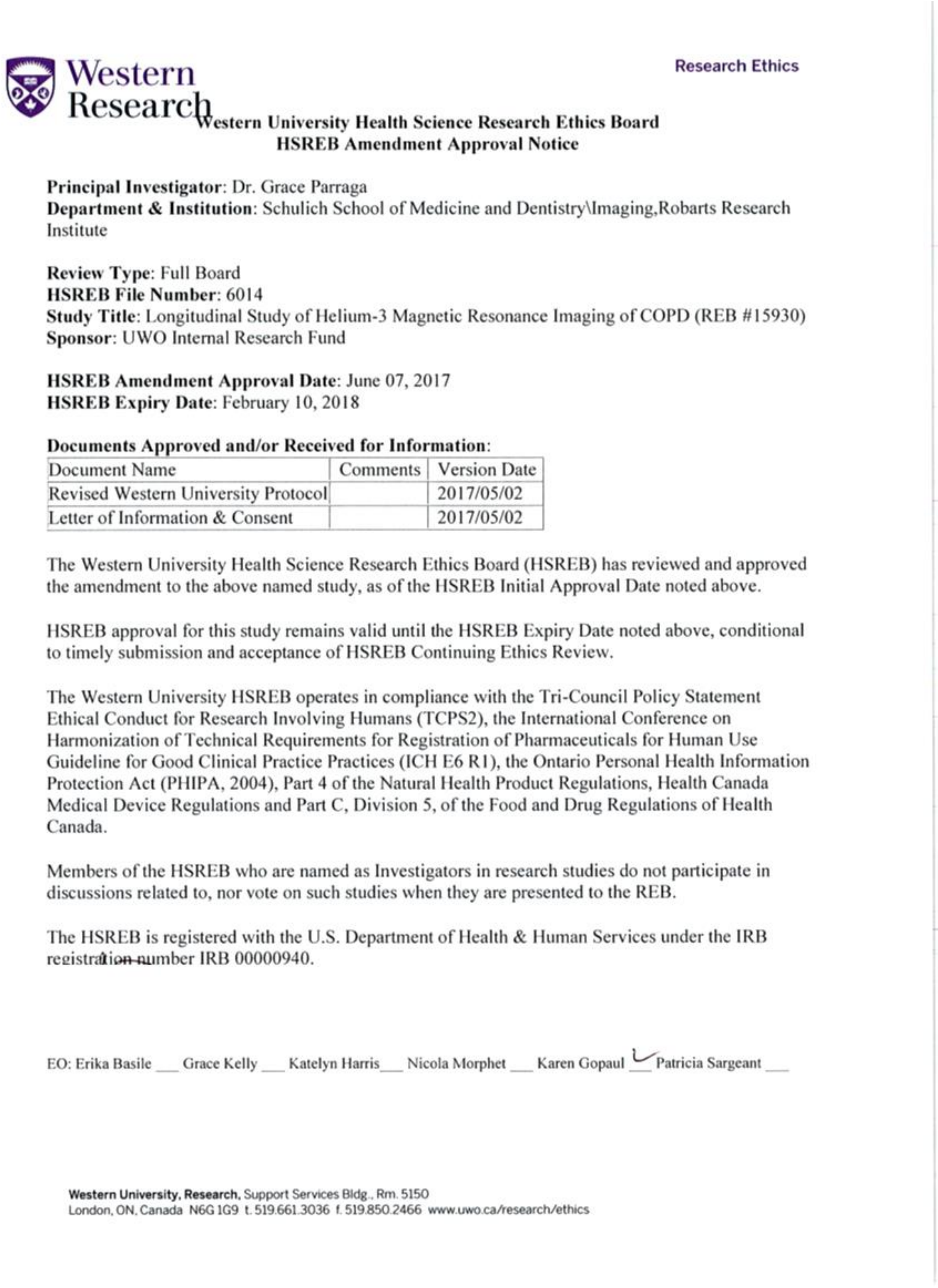

Western Research

Research Ethics

Western University Health Science Research Ethics Board
HSREB Amendment Approval Notice

Principal Investigator: Dr. Grace Parraga
Department & Institution: Schulich School of Medicine and Dentistry\Imaging,Robarts Research Institute

Review Type: Full Board
HSREB File Number: 6014
Study Title: Longitudinal Study of Helium-3 Magnetic Resonance Imaging of COPD (REB #15930)
Sponsor: UWO Internal Research Fund

HSREB Amendment Approval Date: June 07, 2017
HSREB Expiry Date: February 10, 2018

Documents Approved and/or Received for Information:

Document Name	Comments	Version Date
Revised Western University Protocol		2017/05/02
Letter of Information & Consent		2017/05/02

The Western University Health Science Research Ethics Board (HSREB) has reviewed and approved the amendment to the above named study, as of the HSREB Initial Approval Date noted above.

HSREB approval for this study remains valid until the HSREB Expiry Date noted above, conditional to timely submission and acceptance of HSREB Continuing Ethics Review.

The Western University HSREB operates in compliance with the Tri-Council Policy Statement Ethical Conduct for Research Involving Humans (TCPS2), the International Conference on Harmonization of Technical Requirements for Registration of Pharmaceuticals for Human Use Guideline for Good Clinical Practice Practices (ICH E6 R1), the Ontario Personal Health Information Protection Act (PHIPA, 2004), Part 4 of the Natural Health Product Regulations, Health Canada Medical Device Regulations and Part C, Division 5, of the Food and Drug Regulations of Health Canada.

Members of the HSREB who are named as Investigators in research studies do not participate in discussions related to, nor vote on such studies when they are presented to the REB.

The HSREB is registered with the U.S. Department of Health & Human Services under the IRB registration number IRB 00000940.

EO: Erika Basile ___ Grace Kelly ___ Katelyn Harris___ Nicola Morphet ___ Karen Gopaul ✓ Patricia Sargeant ___

Western University, Research, Support Services Bldg., Rm. 5150
London, ON, Canada N6G 1G9 t. 519.661.3036 f. 519.850.2466 www.uwo.ca/research/ethics

Appendix E – Permissions for Reproduction of Scientific Articles

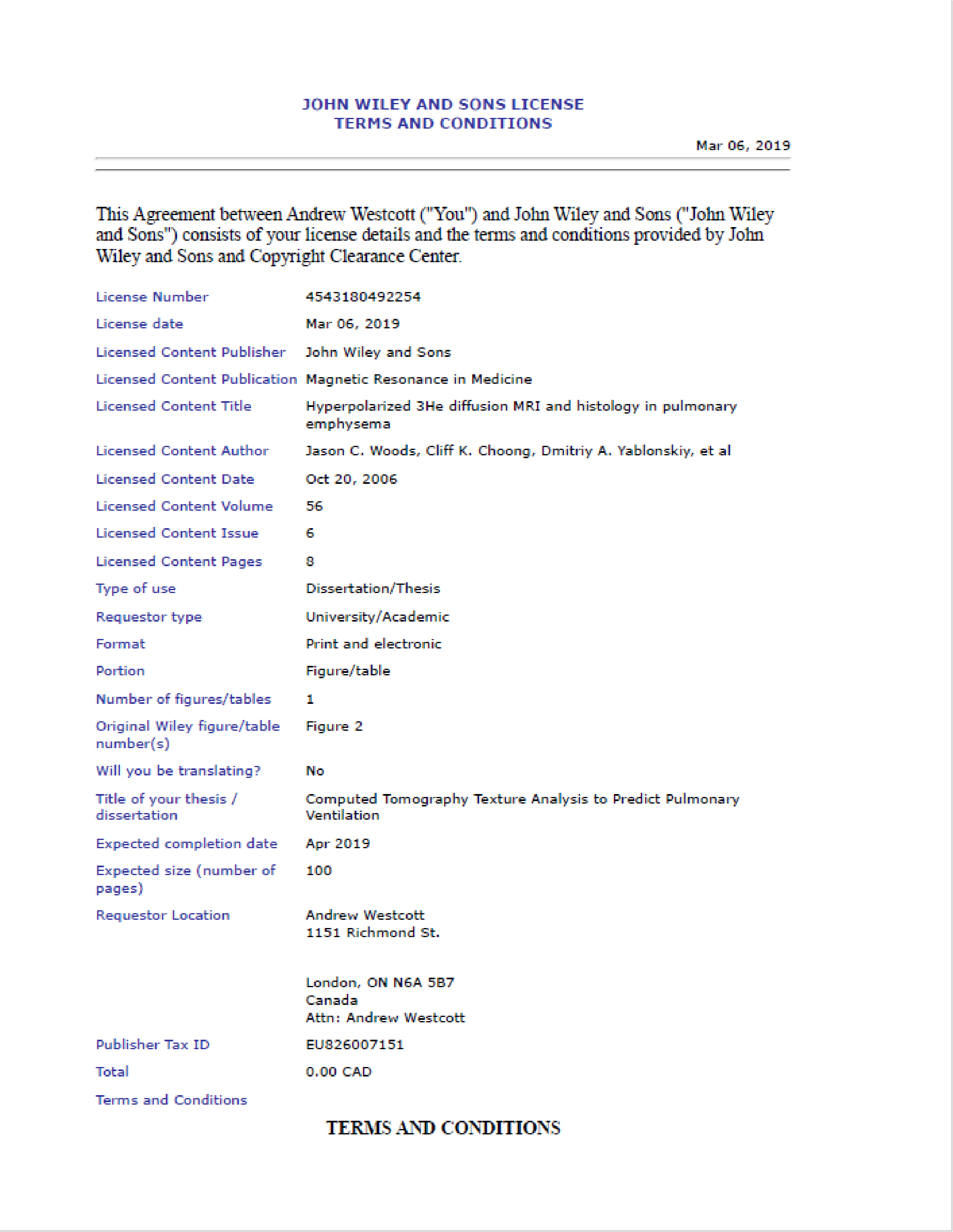

JOHN WILEY AND SONS LICENSE
TERMS AND CONDITIONS

Mar 06, 2019

This Agreement between Andrew Westcott ("You") and John Wiley and Sons ("John Wiley and Sons") consists of your license details and the terms and conditions provided by John Wiley and Sons and Copyright Clearance Center.

License Number	4543180492254
License date	Mar 06, 2019
Licensed Content Publisher	John Wiley and Sons
Licensed Content Publication	Magnetic Resonance in Medicine
Licensed Content Title	Hyperpolarized 3He diffusion MRI and histology in pulmonary emphysema
Licensed Content Author	Jason C. Woods, Cliff K. Choong, Dmitriy A. Yablonskiy, et al
Licensed Content Date	Oct 20, 2006
Licensed Content Volume	56
Licensed Content Issue	6
Licensed Content Pages	8
Type of use	Dissertation/Thesis
Requestor type	University/Academic
Format	Print and electronic
Portion	Figure/table
Number of figures/tables	1
Original Wiley figure/table number(s)	Figure 2
Will you be translating?	No
Title of your thesis / dissertation	Computed Tomography Texture Analysis to Predict Pulmonary Ventilation
Expected completion date	Apr 2019
Expected size (number of pages)	100
Requestor Location	Andrew Westcott 1151 Richmond St. London, ON N6A 5B7 Canada Attn: Andrew Westcott
Publisher Tax ID	EU826007151
Total	0.00 CAD
Terms and Conditions	

TERMS AND CONDITIONS

ELSEVIER LICENSE
TERMS AND CONDITIONS

Mar 06, 2019

This Agreement between Andrew Westcott ("You") and Elsevier ("Elsevier") consists of your license details and the terms and conditions provided by Elsevier and Copyright Clearance Center.

License Number	4543180234163
License date	Mar 06, 2019
Licensed Content Publisher	Elsevier
Licensed Content Publication	The Lancet
Licensed Content Title	Pathophysiology of airflow limitation in chronic obstructive pulmonary disease
Licensed Content Author	James C Hogg
Licensed Content Date	21–27 August 2004
Licensed Content Volume	364
Licensed Content Issue	9435
Licensed Content Pages	13
Start Page	709
End Page	721
Type of Use	reuse in a thesis/dissertation
Portion	figures/tables/illustrations
Number of figures/tables/illustrations	1
Format	both print and electronic
Are you the author of this Elsevier article?	No
Will you be translating?	No
Original figure numbers	Figure 4
Title of your thesis/dissertation	Computed Tomography Texture Analysis to Predict Pulmonary Ventilation
Expected completion date	Apr 2019
Estimated size (number of pages)	100
Requestor Location	Andrew Westcott 1151 Richmond St. London, ON N6A 5B7 Canada Attn: Andrew Westcott
Publisher Tax ID	GB 494 6272 12

JOHN WILEY AND SONS LICENSE
TERMS AND CONDITIONS

Mar 11, 2019

This Agreement between Andrew Westcott ("You") and John Wiley and Sons ("John Wiley and Sons") consists of your license details and the terms and conditions provided by John Wiley and Sons and Copyright Clearance Center.

License Number	4545951488457
License date	Mar 11, 2019
Licensed Content Publisher	John Wiley and Sons
Licensed Content Publication	Journal of Magnetic Resonance Imaging
Licensed Content Title	Hyperpolarized 3He MRI ventilatory apparent diffusion coefficient of alpha-1 antitrypsin deficiency
Licensed Content Author	Grace Parraga, David G. McCormack, Alexei Ouriadov, et al
Licensed Content Date	Aug 13, 2018
Licensed Content Volume	49
Licensed Content Issue	1
Licensed Content Pages	3
Type of use	Dissertation/Thesis
Requestor type	Author of this Wiley article
Format	Print and electronic
Portion	Full article
Will you be translating?	No
Title of your thesis / dissertation	Computed Tomography Texture Analysis to Predict Pulmonary Ventilation
Expected completion date	Apr 2019
Expected size (number of pages)	
Requestor Location	Andrew Westcott 1151 Richmond St. London, ON N6A 5B7 Canada Attn: Andrew Westcott
Publisher Tax ID	EU826007151

JOHN WILEY AND SONS LICENSE
TERMS AND CONDITIONS

Mar 11, 2019

This Agreement between Andrew Westcott ("You") and John Wiley and Sons ("John Wiley and Sons") consists of your license details and the terms and conditions provided by John Wiley and Sons and Copyright Clearance Center.

License Number	4545951401670
License date	Mar 11, 2019
Licensed Content Publisher	John Wiley and Sons
Licensed Content Publication	Journal of Magnetic Resonance Imaging
Licensed Content Title	Rapid single-breath hyperpolarized noble gas MRI-based biomarkers of airspace enlargement
Licensed Content Author	Alexei Ouriadov, Grace Parraga, Fumin Guo, et al
Licensed Content Date	Dec 21, 2018
Licensed Content Volume	0
Licensed Content Issue	0
Licensed Content Pages	10
Type of use	Dissertation/Thesis
Requestor type	Author of this Wiley article
Format	Print and electronic
Portion	Full article
Will you be translating?	No
Title of your thesis / dissertation	Computed Tomography Texture Analysis to Predict Pulmonary Ventilation
Expected completion date	Apr 2019
Expected size (number of pages)	
Requestor Location	Andrew Westcott 1151 Richmond St. London, ON N6A 5B7 Canada Attn: Andrew Westcott
Publisher Tax ID	EU826007151

JOHN WILEY AND SONS LICENSE
TERMS AND CONDITIONS

Mar 11, 2019

This Agreement between Andrew Westcott ("You") and John Wiley and Sons ("John Wiley and Sons") consists of your license details and the terms and conditions provided by John Wiley and Sons and Copyright Clearance Center.

License Number	4545951141118
License date	Mar 11, 2019
Licensed Content Publisher	John Wiley and Sons
Licensed Content Publication	Journal of Magnetic Resonance Imaging
Licensed Content Title	Advanced pulmonary MRI to quantify alveolar and acinar duct abnormalities: Current status and future clinical applications
Licensed Content Author	Alexei Ouriadov, Grace Parraga, David G. McCormack, et al
Licensed Content Date	Jan 13, 2019
Licensed Content Volume	0
Licensed Content Issue	0
Licensed Content Pages	13
Type of use	Dissertation/Thesis
Requestor type	Author of this Wiley article
Format	Print and electronic
Portion	Full article
Will you be translating?	No
Title of your thesis / dissertation	Computed Tomography Texture Analysis to Predict Pulmonary Ventilation
Expected completion date	Apr 2019
Expected size (number of pages)	
Requestor Location	Andrew Westcott 1151 Richmond St. London, ON N6A 5B7 Canada Attn: Andrew Westcott
Publisher Tax ID	EU826007151

Appendix F – Curriculum Vitae

Andrew Westcott

April 2019

EDUCATION

2017-2019

MSc (Medical Biophysics)
Department of Medical Biophysics
Western University, London Canada
Supervisor: Dr. Grace Parraga
Project: 'Texture Analysis and Machine Learning to Predict Pulmonary Ventilation from Thoracic Computed Tomography'

2013-2017

BASc (Engineering Physics – Materials Option)
Department of Physics, Engineering Physics & Astronomy
Queen's University, Kingston Canada

POSITIONS

2018-

Robarts Research Institute
Research Assistant
Robarts Research Institute, Western University
Supervisor: Dr. Grace Parraga
Project: 'Maintenance and operation of gas polarizers for hyperpolarized gas MRI. Maintenance of lab website and computer infrastructure'

2016

Sunnybrook Research Institute
Summer Student
Medical Physics – X-ray Imaging Research Group
Supervisor: Dr. John Rowlands
Project: 'Designing a Model to Investigate Charge in Amorphous Selenium Flat Panel X-Ray Detectors'

2015

Queen's University
Undergraduate Research Assistant
Department of Mechanical and Materials Engineering
Supervisor: Dr. David Rival
Project: 'Creating a Novel Refractive Index Matched Hydrogel Model for 3D Fluid Flow Analysis'

HONOURS AND AWARDS

2019	**ISMRM Educational Stipend Award** ISMRM Annual Meeting 2019 *Awarded to support the attendance of students, postdoctoral and clinical trainees to present abstracts at the scientific meeting* **$535 USD**
2019	**Canadian Thoracic Society Poster Competition** American Thoracic Society Annual Meeting *Selected as one of the Top 30 abstracts submitted to the American Thoracic Society conference.*
2018-	**Western Graduate Research Scholarship** Department of Medical Biophysics, Western University *Awarded to a full time graduate student for stipend support who has maintained an average of 80% or more* **$1,667 per term**
2017- 2018	**Western Graduate Research Scholarship** Department of Medical Biophysics, Western University *Awarded to a full time graduate student for stipend support who has maintained an average of 80% or more* **$1,500 per term**
2018	**ISMRM Educational Stipend Award** Joint Annual Meeting ISMRM-ESMRMB 2018 *Awarded to support the attendance of students, postdoctoral and clinical trainees to present abstracts at the scientific meeting* **$525 USD**
2015-2017	**Dean’s Scholar** Queen’s University *Granted to Undergraduate Engineering students who obtain a GPA of 3.5 or higher*
2013	**Queen’s University Excellence Scholarship** Queen’s University *Entrance scholarship based on high school grades of 90.0-94.9%* **$2,000**

PRESENTATIONS AND PRESENTATIONS

A Peer Reviewed Journal Manuscripts

In Preparation (n=1)

1. DPI Capaldi, C Ong-Ly, **A Westcott**, RL Eddy, F Guo, DG McCormack and G Parraga. *Hyperpolarized 3He MRI Biomarkers of Ventilation Defect Clusters: Comparison in Chronic Obstructive Pulmonary Disease and Bronchiectasis*. In preparation for Academic Radiology.

Submitted (n=1)

1. **A Westcott**, DPI Capaldi, DG McCormack, A Ward, A Fenster and G Parraga. *Chronic Obstructive Pulmonary Disease: Thoracic CT Texture Analysis and Machine Learning to Predict Pulmonary Ventilation.* Submitted to Radiology February 26, 2019.

Accepted (n=4)

1. **A Westcott,** DPI Capaldi, A Ouriadov, DG McCormack and G Parraga. *Hyperpolarized 3He MRI ventilator apparent diffusion coefficient of alpha-1 antitrypsin deficiency.* JMRI 2018. DOI: 10.1002/jmri.26202.
2. **A Westcott,** F Guo, G Parraga and A Ouriadov. *Rapid single-breath hyperpolarized noble gas MRI-based biomarkers of airspace enlargement.* JMRI 2018. DOI: 10.1002/jmri.26574
3. RL Eddy, **A Westcott**, GN Maksym, G Parraga and RJ Dandurand. *Oscillometry and Pulmonary Magnetic Resonance Imaging in Asthma and COPD.* Physiological Reports. DOI: 10.14814/phy2.13955.
4. **A Westcott,** DG McCormack, G Parraga and A Ouriadov. *Advanced Pulmonary MRI to Quantify Alveolar and Acinar Duct Abnormalities: Current Status and Future Clinical Applications.* JMRI 2018. DOI: 10.1002/jmri.26623.

B Peer Reviewed Published Conference Proceedings

Accepted (n=2)

1. **A Westcott**, DPI Capaldi, DG McCormack, A Fenster and G Parraga. *Texture Analysis of Thoracic CT to Predict Hyperpolarized Gas MRI Lung Function.* SPIE Proceedings (oral presentation).
2. JL MacNeil, DPI Capaldi, RL Eddy, **A Westcott**, AM Matheson, AL Barker, C OngLy, DG McCormack and G Parraga. *Development and Evaluation of Pulmonary Imaging Multi-Parametric Response Maps for Deep Phenotyping of Chronic Obstructive Pulmonary Disease.* SPIE Proceedings (oral presentation).

B Peer Reviewed Conference Abstracts

Submitted (n=1)

1. RL Eddy, **A Westcott,** M Kirby, DG McCormack, G Parraga. CT Pulmonary Vessel Volume in Ex-smokers with Normal FEV_1. *European Respiratory Society International Congress 2019 Madrid, Spain September 28-October 2, 2019.*

Accepted (n=21)

1. **A Westcott**, DPI Capaldi, D McCormack, A Fenster and G Parraga. Machine Learning for Lung Function Synthesis: Predicting MRI Ventilation from Thoracic CT. *Imaging Network of Ontario Symposium 2019.*
2. RL Eddy, **A Westcott**, GN Maksym, DG McCormack and G Parraga. Can Oscillometry Explain Differences Between 3He and 129Xe Ventilation Heterogeneity? *Imaging Network of Ontario Symposium 2019.*
3. AL Barker, RL Eddy, AM Matheson, **A Westcott**, GR Washko and G Parraga. Is Vascular Pruning Related to MRI Ventilation Defects in Bronchiectasis and COPD Patients? *Imaging Network of Ontario Symposium 2019.*
4. JL MacNeil, DPI Capaldi, **A Westcott**, DG McCormack and G Parraga. Novel COPD Multi-parametric Response Map Phenotypes. *Imaging Network of Ontario Symposium 2019.*
5. A Ouriadov, **A Westcott**, DG McCormack and G Parraga. Longitudinal Emphysema Measurements in Patients using 3He and 129Xe MRI. *Imaging Network of Ontario Symposium 2019.*
6. **A Westcott**, M Kirby, DG McCormack and G Parraga. Normal Thoracic CT in Ex-smokers without COPD: Can Machine Learning Reveal Subclinical Disease? American Thoracic Society Annual Scientific Meeting 2019 Dallas, TX, United States May 17-22, 2019.
7. AL Barker, RL Eddy, AM Matheson, **A Westcott**, GR Washko and G Parraga. Bronchiectasis, Vascular Pruning and Ventilation Defects in COPD and Bronchiectatic Patients: Are They Related? American Thoracic Society Annual Scientific Meeting 2019 Dallas, TX, United States May 17-22, 2019.
8. JL MacNeil, DPI Capaldi, **A Westcott**, DG McCormack and G Parraga. Novel Multi-parametric Response Map COPD Phenotypes. American Thoracic Society Annual Scientific Meeting 2019 Dallas, TX, United States May 17-22, 2019.
9. C Ong Ly, **A Westcott**, I Dhaliwal, A Fenster, M Kirby and G Parraga. Can Machine Learning and MRI Identify COPD Patients at Risk of Accelerated Progression? American Thoracic Society Annual Scientific Meeting 2019 Dallas, TX, United States May 17-22, 2019.
10. A Ouriadov, **A Westcott** and G Parraga. Feasibility of Longitudinal Emphysema Measurements in COPD and Alpha-1 Antitrypsin Deficiency Using 3He and 129Xe MRI. American Thoracic Society Annual Scientific Meeting 2019 Dallas, TX, United States May 17-22, 2019.
11. **A Westcott**, A Ouriadov, RL Eddy, DG McCormack, M Kirby, G Parraga. Compressed Sensing Hyperpolarized Noble Gas Ventilation MRI: Towards a Maximum Clinically Acceptable Acceleration Factor. International Society for Magnetic Resonance in Medicine Annual Scientific Meeting 2019 Montreal, Canada May 11-16, 2019.

12. C Ong-Ly, **A Westcott**, I Dhaliwal, A Fenster, M Kirby and G Parraga. Hyperpolarized Ventilation MRI and Ensemble Machine Learning Predict Airflow Limitation Worsening in Ex-smokers. International Society for Magnetic Resonance in Medicine Annual Scientific Meeting 2019 Montreal, Canada May 11-16, 2019.
13. S Svenningsen, A Ouriadov, NB Konyer, RL Eddy, **A Westcott**, DG McCormack, M Kjarsgaard, MD Noseworthy, P Nair and G Parraga. Two-site Reproducibility of Hyperpolarized ^{129}Xe MRI Ventilation in Severe Asthma: Implications for Multicenter Clinical Studies. International Society for Magnetic Resonance in Medicine Meeting, Montreal, QC, Canada
14. A Ouriadov, **A Westcott**, DG McCormack, G Parraga. Feasibility of ^{129}Xe MRI Morphometry Measurements with Acceleration Factors of 7 and 10. International Society for Magnetic Resonance in Medicine Annual Scientific Meeting 2019 Montreal, Canada May 11-16, 2019.
15. RL Eddy, **A Westcott**, GN Maksym, DG McCormack, G Parraga. Differences between ^{3}He and ^{129}Xe Ventilation Heterogeneity Explained Using Oscillometry. International Society for Magnetic Resonance in Medicine Annual Scientific Meeting 2019 Montreal, Canada May 11-16, 2019.
16. AL Barker, **A Westcott**, RL Eddy, DG McCormack, G Parraga and A Ouriadov. Feasibility of Single Breath-hold Isotropic Voxel ^{129}Xe MRI in Patients. International Society for Magnetic Resonance in Medicine Annual Scientific Meeting 2019 Montreal, Canada May 11-16, 2019.
17. **A Westcott**, DG McCormack and G Parraga. Texture Analysis of Thoracic CT to Predict Hyperpolarized Gas MRI Lung Function. *SPIE Medical Imaging Proceedings (oral presentation).*
18. JL MacNeil, DPI Capaldi, RL Eddy, **A Westcott**, AM Matheson, AL Barker, C OngLy, DG McCormack and G Parraga. Development and Evaluation of Pulmonary Imaging Multi-Parametric Response Maps for Deep Phenotyping of Chronic Obstructive Pulmonary Disease. *SPIE Medical Imaging Proceedings (oral presentation).*
19. **A Westcott**, R Eddy, DPI Capaldi, H Young, DG McCormack and G Parraga, Quantification of Hyperpolarized ^{3}He MRI Ventilation Heterogeneity in asthmatics: Surface area of ventilation clusters. *International Society for Magnetic Resonance in Medicine Meeting Proceedings 2018*.
20. **A Westcott**, DPI Capaldi, A Ouriadov, DG McCormack and G Parraga, Longitudinal Imaging Biomarkers of Severe Emphysema in AATD and COPD. *London Health Research Day 2018.*
21. **A Westcott**, R Eddy DPI Capaldi, H Young, DG McCormack and G Parraga. Quantification of Hyperpolarized ^{3}He MRI Ventilation Heterogeneity in Asthmatics: Surface Area of Ventilation Clusters. *Robarts Research Retreat 2018.*

C Poster Presentations (n=4)

1. **A Westcott**, R Eddy, DPI Capaldi, H Young, DG McCormack and G Parraga, Quantification of Hyperpolarized ^{3}He MRI Ventilation Heterogeneity in asthmatics:

Surface area of ventilation clusters. *International Society for Magnetic Resonance in Medicine Meeting Proceedings 2018*. (electronic poster)

2. **A Westcott**, DPI Capaldi, A Ouriadov, DG McCormack and G Parraga. Imaging Biomarkers of Airspace Enlargement: Alpha-1 Antitrypsin Deficiency. *London Imaging Discovery Day 2018*. (electronic poster)
3. **A Westcott**, DPI Capaldi, A Ouriadov, DG McCormack and G Parraga, A Novel Magnetic Resonance Imaging Biomarker of Airspace Enlargement in Alpha-1 Antitrypsin Deficiency. *London Health Research Day 2018*. (traditional poster)
4. **A Westcott**. Designing a Model to Investigate Charge in Amorphous Selenium Flat Panel X-Ray Detectors. *Queen's University Department of Physics Thesis Poster Presentation*, Kingston, Ontario, April 12, 2017. (traditional poster)

D Academic Reports (n=1)

1. **A Westcott**. Designing a Model to Investigate Charge in Amorphous Selenium Flat Panel X-Ray Detectors. *Queen's University Undergraduate Thesis*, Kingston, Ontario, 2017.

PROFESSIONAL SOCIETIES

2017-	International Society for Magnetic Resonance in Medicine *Student Member*
2018-	American Thoracic Society *Student Member*
2018-	International Society for Optics and Photonics (SPIE) *Student Member*

COMMUNITY ACTIVITIES

2017-	**BIRC Deep Learning Club Co-coordinator** *Co-coordinators:* Rachel Eddy, Wenyao Xia, Patricia Johnson *Goal:* Organize monthly seminars for introduction and exploration of deep learning applications in medical research. *Responsibilities:* Give presentations and organize a community for deep learning.
2016-2017	**Let's Talk Science** *Workshop Volunteer* Queen's University
2014-2017	**Mini Baja Design Team** *Team Member* Queen's University